



## 저작자표시-비영리-동일조건변경허락 2.0 대한민국

이용자는 아래의 조건을 따르는 경우에 한하여 자유롭게

- 이 저작물을 복제, 배포, 전송, 전시, 공연 및 방송할 수 있습니다.
- 이차적 저작물을 작성할 수 있습니다.

다음과 같은 조건을 따라야 합니다:



저작자표시. 귀하는 원저작자를 표시하여야 합니다.



비영리. 귀하는 이 저작물을 영리 목적으로 이용할 수 없습니다.



동일조건변경허락. 귀하가 이 저작물을 개작, 변형 또는 가공했을 경우에는, 이 저작물과 동일한 이용허락조건하에서만 배포할 수 있습니다.

- 귀하는, 이 저작물의 재이용이나 배포의 경우, 이 저작물에 적용된 이용허락조건을 명확하게 나타내어야 합니다.
- 저작권자로부터 별도의 허가를 받으면 이러한 조건들은 적용되지 않습니다.

저작권법에 따른 이용자의 권리는 위의 내용에 의하여 영향을 받지 않습니다.

이것은 [이용허락규약\(Legal Code\)](#)을 이해하기 쉽게 요약한 것입니다.

[Disclaimer](#)

공학박사학위논문

**Platinum Group Electrocatalysts and Multiscale  
Electrode Structure for Oxygen Reduction in  
Polymer Electrolyte Membrane Fuel Cell**

**고분자 전해질 연료전지의 산소환원반응을 위한  
백금족 전기촉매 및 멀티스케일 전극 구조**

2015 년 8 월

서울대학교 대학원

화학생명공학부

강 윤 식

## **Abstract**

# **Platinum Group Electrocatalysts and Multiscale Electrode Structure for Oxygen Reduction in Polymer Electrolyte Membrane Fuel Cell**

Yun Sik Kang

School of Chemical and Biological Engineering

The Graduate School

Seoul National University

As one of the most noticeable new energy sources, polymer electrolyte membrane fuel cell (PEMFC) is a state of the art energy conversion device producing electricity from hydrogen and oxygen for automotive and stationary applications, due to its high efficiency and no or less emission of pollutants. However, the commercialization of PEMFC is significantly obstructed by the high price of Pt and sluggish kinetic reaction of electrocatalyst with oxygen. A considerable amount of study has been done to decrease the amount of Pt used while maintaining high oxygen reduction reaction (ORR) activity and low manufacturing cost; forming Pt based bimetallic alloy with other transition metals and core-shell structured nanoparticles (NPs), non-Pt alloy or their oxides, carbon-supported

transition metal/nitrogen (M-N-C) materials and conductive polymers, which are primarily intended for lowering the cost of the PEMFC while possessing high ORR activity. In the aspect of electrode structure and system, in addition, many studies related to the modifications of electrode catalyst layer and polymer electrolyte membrane structures such as the usage of pore-forming agent, patterned Nafion membrane and ordered structure of Pt catalyst layer for better PEMFC single cell performance. In other words, these researches are related to the improvement of catalytic activity and utilization of Pt group metal electrocatalyst.

In this study, the novel methodologies for the enhancement of PEMFC performance and utilization of Pt group (Pt, Pd) electrocatalyst via atomic scale and macroscale approaches were suggested. First, in case of atomic scale approaches focusing on electrocatalyst itself, the novel synthetic methods of Pt bimetallic alloy nanoparticles (NPs) via Al pitting corrosion method was proposed. Al metal as a reducing agent has many advantages such as a good reducing capability, easy transportation and storage because of its solid form and spontaneous oxide film formation under ambient condition. By utilizing this novel synthesizing method, carbon supported Pt and Pt-M (Au, Pd) NPs were synthesized very easily without any complex conditions and samples were analyzed via physical, chemical and electrochemical analyses. Additionally, post heat treatments with various conditions were conducted to elucidate the relationship between ORR activity and surface atomic structure of electrocatalyst.

Second, highly active PdFe alloy NPs were synthesized via modified two-step chemical synthesis method, which combines polyol reduction method and conventional sodium borohydride method. PdM (M=Fe, Co, Ni, Ti and Cu) bimetallic alloy materials have attracted recent attention because of their many advantages, such as much cheaper material price, higher estimated reserves and similar or better catalytic properties compared to Pt. PdFe alloy NPs were prepared via two ways before mentioned and the physical and electrochemical properties were examined. In addition, the effect of post heat treatment on ORR activity was analyzed by using physical and electrochemical measurements. By the heat treatment, PdFe NPs exhibited intermetallic structures with Pd rich surface shell and ordered PdFe core. Due to this structural modifications, heat treated PdFe NPs exhibited the downshift of d-band center of Pd and, as a result, higher ORR activity compared to as prepared PdFe NPs and conventional carbon supported Pt electrocatalyst.

Third, as a macroscale approach for the structural modifications of catalyst layer and polymer electrolyte structures, multiscale approach were applied and optimized for enhancing the performance of PEMFC. With an aid of multiplex lithography that integrates rational advantages in both microscale and nanoscale, complex and multiscale architectures were embedded into polymer electrolyte Nafion membrane of PEMFC via thermal imprinting process. From the measurements, the prepared multiscale patterned Nafion membrane exhibited enhanced physical and

electrochemical properties compared to commercial Nafion 211 and 212 due to its multiscale structure. The membrane electrode assembly (MEA) with multiscale patterned Nafion membrane exhibited higher PEMFC performance due to increased electrochemically active surface area (ECSA) and decrease of membrane resistance in the thinned polymer electrolyte membrane. In addition, for realistic applications of PEMFC, we conducted accelerated durability test (ADT) to mimic actual operating condition of PEMFC by potential cycling according to DOE protocols. After ADT, MEA with multiscale Nafion membrane still exhibited much higher single cell performance than conventional one without breakdown or short-circuit.

From these structural and compositional modifications of Pt group electrocatalysts via atomic scale (Pt and Pd bimetallic alloy NPs) and macroscale approaches (Structural change in cathode catalyst layer via multiscale approach), in conclusion, the catalytic activity of Pt group electrocatalysts and PEMFC single cell performance were highly enhanced. Furthermore, these methods can be helpful for designing new materials and electrode systems for another energy conversion devices such as batteries and solar cells.

**Key Words :** Polymer electrolyte membrane fuel cell, Oxygen reduction reaction, Pt group bimetallic alloy, Pt catalyst layer, Crystalline structure, Multiscale structure.

**Student Number:** 2011-30274

# Contents

<b>Abstract .....</b>	<b>i</b>
<b>List of Figures.....</b>	<b>viii</b>
<b>List of Tables .....</b>	<b>xiv</b>
 <b>Chapter 1. Introduction.....</b>	 <b>1</b>
1.1. Theoretical basis of Fuel Cells .....	1
1.2. Polymer electrolyte membrane fuel cells.....	7
1.3. Recent development of electrocatalyst and electrode structure.....	12
1.4. Objectives of this study .....	16
<b>Chapter 2. Experimental .....</b>	<b>20</b>
2.1. Platinum Bimetallic Alloy Electrocatalyst synthesized by Al Pitting Corrosion method .....	20
2.1.1. Synthesis of carbon supported Pt and Pt-M (Au, Pd) NPs .....	20
2.1.2. Post heat treatment of Pt and Pt-M (Au, Pd) NPs.....	21
2.1.3. Membrane electrode assembly (MEA) preparation.....	22
2.1.4. Physical characterization of carbon supported Pt and Pt-M (Au, Pd) NPs ...	22
2.1.5. Electrochemical measurements of carbon supported Pt and Pt-M (Au, Pd) NPs .....	23
2.2. Palladium-Iron Alloy Electrocatalyst via Modified Chemical Synthesis.....	27
2.2.1. Synthesis of carbon supported Pd <sub>x</sub> Fe <sub>y</sub> NPs.....	27
2.2.2. Post heat treatment of carbon supported Pd <sub>x</sub> Fe <sub>y</sub> NPs.....	28
2.2.3. Membrane electrode assembly (MEA) preparation.....	28
2.2.4. Physical characterization of carbon supported Pd <sub>x</sub> Fe <sub>y</sub> NPs .....	29
2.2.5. Electrochemical measurements of carbon supported Pd <sub>x</sub> Fe <sub>y</sub> NPs .....	31
2.3. Polymer Electrolyte Membrane Fuel Cell with Multiscale Nafion membrane.....	34
2.3.1. Preparation of hierarchical structure.....	34
2.3.2. Preparation of multiscale Nafion membrane via thermal imprinting process .....	35
2.3.3. Membrane electrode assembly (MEA) preparation.....	36



2.3.4. Physical analysis of hierarchical multiscale structure .....	36
2.3.5. Electrochemical measurements of polymer electrolyte membrane fuel cell with multiscale Nafion membrane .....	37
<b>Chapter 3. Results and Discussion.....</b>	<b>39</b>
3.1. Platinum Bimetallic Alloy Electrocatalyst synthesized by Al Pitting Corrosion method .....	39
3.1.1. Physical characterization carbon supported Pt and Pt-M (Au, Pd) NPs .....	39
3.1.2. Electrochemical characterizations of carbon supported Pt and Pt-M (Au, Pd) NPs .....	42
3.2. Palladium-Iron Alloy Electrocatalyst via Modified Chemical Synthesis.....	69
3.2.1. Physical characterization carbon supported Pd <sub>x</sub> Fe <sub>y</sub> NPs .....	69
3.2.2. Electrochemical characterizations of carbon supported Pd <sub>x</sub> Fe <sub>y</sub> NPs. ....	76
3.3. Polymer Electrolyte Membrane Fuel Cell with Multiscale Nafion membrane.....	103
3.3.1. Achieving complex and multiscale structures via multiplex lithography .....	103
3.3.2. Physical and electrochemical characterization .....	111
<b>Chapter 4. Conclusions.....</b>	<b>130</b>
<b>References.....</b>	<b>133</b>
<b>국문초록 .....</b>	<b>142</b>

## List of Figures

**Figure 1-1.** Schematic illustration of fuel cell.

**Figure 1-2.** Sketch of William Grove's 1839 fuel cell system.

**Figure 1-3.** Classification of fuel cell systems according to their applications.

**Figure 1-4.** Cell reaction of PEMFC.

**Figure 1-5.** Polarization curve of PEMFC and three major losses during the cell operation.

**Figure 1-6.** Classification of the researches related to electrocatalyst for PEMFC.

**Figure 1-7.** Classification of the researches related to structural modifications of electrode of PEMFC.

**Figure 1-8.** Objectives of this study according to the approaches of different scale.

**Figure 2-1.** Schematic illustration of (a) the synthesis via Al pitting corrosion method and (b) the heat treatment process.

**Figure 2-2.** Schematic illustration of (a) the two-step synthesis and (b) the heat treatment process.

**Figure 3-1.** XRD spectra of carbon supported Pt and Pt-M (Au, Pd) NPs prepared by Al pitting corrosion method.

**Figure 3-2.** XRD spectra of carbon supported Pt and Pt-M (Au, Pd) NPs prepared by sodium borohydride method.

**Figure 3-3.** TEM images of carbon supported Pt and Pt-M (Au, Pd) NPs prepared by Al pitting corrosion method with various conditions and their particle size distributions.

**Figure 3-4.** EDS mapping analysis of carbon supported Pt and Pt-M (Au, Pd) NPs.

**Figure 3-5.** TEM images of carbon supported Pt and Pt-M (Au, Pd) NPs prepared by sodium borohydride method with various conditions and their particle size distributions.

**Figure 3-6.** Comparison of bulk and surface composition of Pt bimetallic alloy NPs

prepared by Al pitting corrosion method.

**Figure 3-7.** Comparison bulk and surface composition of Pt bimetallic alloy NPs prepared by sodium borohydride method.

**Figure 3-8.** Cyclic voltammogram ((a), (c), (e)) and ORR polarization curve ((b), (d), (f)) of carbon supported Pt and Pt-M (Au, Pd) NPs prepared by Al pitting corrosion method with various conditions.

**Figure 3-9.** Relationship between ECSA and mass and specific activity at 0.9 V vs. RHE of carbon supported Pt and Pt-M (Au, Pd) NPs synthesized via Al pitting corrosion with various conditions.

**Figure 3-10.** Cyclic voltammogram ((a), (c), (e)) and ORR polarization curve ((b), (d), (f)) of carbon supported Pt and Pt-M (Au, Pd) NPs prepared by sodium borohydride method with various conditions.

**Figure 3-11.** Relationship between ECSA and mass and specific activity at 0.9 V vs. RHE of carbon supported Pt and Pt-M (Au, Pd) NPs synthesized via sodium borohydride method with various conditions.

**Figure 3-12.** CO stripping voltammogram ((a), (c), (e)) and N<sub>2</sub>O reduction curve ((b), (d), (f)) of carbon supported Pt and Pt-M (Au, Pd) NPs prepared by Al pitting corrosion method with various conditions.

**Figure 3-13.** Comparison area normalized ORR activity at 0.9 V vs. RHE and binding energies of 4f Pt<sup>0</sup> of Pt bimetallic alloy NPs prepared by Al pitting corrosion method.

**Figure 3-14.** MOR data of carbon supported Pt and Pt-M (Au, Pd) NPs prepared by Al pitting corrosion method with various conditions.

**Figure 3-15.** CO stripping voltammogram of carbon supported Pt and Pt-M (Au, Pd) NPs prepared by sodium borohydride method with various conditions.

**Figure 3-16.** Single cell test of Pt bimetallic alloy NPs prepared by Al pitting corrosion method and their Pt mass normalized maximum power density.

**Figure 3-17.** TEM images of ASP and HT Pd<sub>x</sub>Fe<sub>y</sub> samples prepared by two-step synthesis with particle size distribution and mean particle diameter. (a) and (d) for ASP and HT Pd<sub>3</sub>Fe<sub>1</sub>, (b) and (e) for ASP and HT Pd<sub>1</sub>Fe<sub>1</sub>, (c) and (f) for ASP and HT Pd<sub>1</sub>Fe<sub>3</sub>.

**Figure 3-18.** HRPD patterns of ASP and HT samples prepared by two-step synthesis and their whole pattern matching data.

**Figure 3-19.** TEM images of ASP and HT Pd<sub>x</sub>Fe<sub>y</sub> samples prepared by one-step synthesis with particle size distribution and mean particle diameter. (a) and (d) for ASP and HT Pd<sub>3</sub>Fe<sub>1</sub>, (b) and (e) for ASP and HT Pd<sub>1</sub>Fe<sub>1</sub>, (c) and (f) for ASP and HT Pd<sub>1</sub>Fe<sub>3</sub>.

**Figure 3-20.** XRD patterns of ASP and HT samples prepared by one-step synthesis.

**Figure 3-21.** XAS characterization of ASP and HT Pd<sub>x</sub>Fe<sub>y</sub> samples prepared by two-step synthesis for (a) Pd K-edge and (c) Fe K-edge and their Fourier transformed spectra for (a) Pd K-edge and (c) Fe K-edge.

**Figure 3-22.** XPS spectra of ASP and HT Pd<sub>x</sub>Fe<sub>y</sub> samples prepared by two-step synthesis (a) Pd 3d and (b) Fe 2p.

**Figure 3-23.** XPS spectra of ASP and HT Pd<sub>x</sub>Fe<sub>y</sub> samples prepared by one-step synthesis (a) Pd 3d and (b) Fe 2p.

**Figure 3-24.** Comparison of binding energies of 3d Pd<sup>0</sup> of Pd<sub>x</sub>Fe<sub>y</sub> alloy NPs prepared by two-step synthesis.

**Figure 3-25.** Comparison of bulk and surface atomic composition of ASP and HT Pd<sub>x</sub>Fe<sub>y</sub> samples prepared by two-step synthesis.

**Figure 3-26.** Comparison of bulk and surface atomic composition of ASP and HT Pd<sub>x</sub>Fe<sub>y</sub> samples prepared by one-step synthesis.

**Figure 3-27.** Cyclic voltammogram ((a), (c)) and ORR polarization curve ((b), (d)) of ASP and HT Pd<sub>x</sub>Fe<sub>y</sub> samples prepared by two-step synthesis.

**Figure 3-28.** (a) Mass and (b) area normalized ORR activity at 0.9 V vs. RHE.

**Figure 3-29.** Cyclic voltammogram ((a), (c)) and ORR polarization curve ((b), (d)) of ASP

and HT Pd<sub>x</sub>Fe<sub>y</sub> samples prepared by one-step synthesis.

**Figure 3-30.** CO stripping voltammogram ((a), (c)) and N<sub>2</sub>O reduction curve ((b), (d)) of ASP and HT Pd<sub>x</sub>Fe<sub>y</sub> samples prepared by two-step synthesis.

**Figure 3-31.** CO stripping voltammogram of ASP and HT Pd<sub>x</sub>Fe<sub>y</sub> samples prepared by one-step synthesis.

**Figure 3-32.** Cyclic voltammogram ((a), (c)) and ORR polarization curve ((b), (d)) of ASP and HT Pd<sub>x</sub>Fe<sub>y</sub> samples prepared by two-step synthesis after ADT.

**Figure 3-33.** Pd mass normalized ORR activity as 0.9 V vs. RHE of HT Pd<sub>x</sub>Fe<sub>y</sub> NPs prepared by two-step synthesis before and after ADT.

**Figure 3-34.** Single cell test of HT Pd<sub>x</sub>Fe<sub>y</sub> NPs prepared by two-step synthesis and their Pd mass normalized maximum power density.

**Figure 3-35.** (a) Single-scale structures from soft lithography. (b) Multiscale perspective of a complex, hierarchical architecture from multiplex lithography. The architecture has independent nanopatterns (dots and lines) on each flat surface. (c) Illustration of a ‘gray zone’ with infiltrated oxygen from a permeable PDMS blanket. (d) Calculated curing contrast after short time-dependent UV exposure. (e) Hypothesis for multiple curing with UV to form complex hierarchical architectures from simple molding processes.

**Figure 3-36.** Micro ebb tides in partially cured resin for the generation of a multiple contrast brick (MCB). (a) Schematic illustration for the overlapping of OIL and the resulting micro ebb tide after the first UV exposure. The micro ebb tides gradually reduce the curing contrast on the top surface of the brick from  $\alpha$  to  $\alpha'$ . (b) Microscopic images of the real-time monitoring of micro ebb tides. The low affinity of viscoelastic PUA resin to PDMS pillars yields the spontaneous coating of partially cured resin on the top surface of the brick. (c) Digital image of the MCB produced as a unit part for LEGO®-like stacking.

**Figure 3-37.** (a) Schematic illustration for the vertical stacking of MCBs and the connected interfaces under a surface selection between relatively high ( $\alpha$ ) and low ( $\alpha'$ ) curing contrasts of the MCB. (b) SEM images of the integrated MCB (20- $\mu\text{m}$  holes) on the underlying substrate (800-nm in diameter). (c), (d) Analysis for the deformability in accordance with the curing contrast under a surface selection. A focused ion beam (FIB) study reveals the differences in the deformability at a fixed ratio with a diameter of 25, where the bottom surface with relatively high curing contrast ( $\alpha \sim 55\%$ ) remained the unfilled nanoholes (c), while a large fluidity of the viscoelastic coating ( $\alpha \sim 45\%$ ) showed a sufficient deformation to fill even microholes (d). (e), (f), (g) SEM images of the replicated two-level hierarchical structures from the stacked bricks.

**Figure 3-38.** (a) Schematic illustration for the fabrication of a four-level polymeric architecture via the multi-stacking process with MCBs. (b) Multiscale perspective for the obtained four-level architecture with various pillars of increasing sizes (150 nm/8  $\mu\text{m}$ /165  $\mu\text{m}$ /500  $\mu\text{m}$ ).

**Figure 3-39.** (a) Schematic illustration of the multiplex lithography. Both imprinting and bonding is achieved with the top and bottom surfaces of the brick ( $\alpha'$  and  $\alpha$ , respectively) to form complex hierarchical architectures. (b), (c), (d), (e), (f), (g) SEM images of the bricks (b, c), monolithic assemblies (d, e) and final architectures after replication (f, g).

**Figure 3-40.** (a) Tensile strength test of membranes and (b) COMSOL simulation data related to force distribution.

**Figure 3-41.** (a) Schematic illustration of the device operation with multiscale Nafion membrane. (b) SEM images of imprinted multiscale Nafion membrane. (c) Measured proton conductivities of each patterned Nafion membrane. (d) The difference between the maximum power densities of conventional

membrane electrode assembly (MEA) and the MEA with a multiscale Nafion membrane under the conditions of  $\text{H}_2/\text{Air}$  and  $\text{H}_2/\text{O}_2$  with or without outlet pressure. (e) Measured polarization curves.

**Figure 3-42.** (a) Cyclic voltammogram (CV), (b) electrochemical impedance spectroscopy (EIS) of MEAs and (c) its equivalent circuit.

**Figure 3-43.** Polarization curves conventional MEA and the MEA with a multiscale Nafion membrane before and after ADT under the conditions of (a), (b)  $\text{H}_2/\text{Air}$  and (c), (d)  $\text{H}_2/\text{O}_2$  with or without outlet pressure of 150 kPa.

**Figure 3-44.** (a) Cyclic voltammogram (CV) and difference in ECSAs of MEAs after ADT.

**Figure 3-45.** Comparison of ECSAs of conventional MEA and the MEA with a multiscale Nafion membrane before and after ADT.

**Figure 3-46.** (a) Measurement of permeated hydrogen oxidation current via linear sweep voltammetry in the range from 0 to 0.7 V. vs. RHE and (b) the moles of permeated hydrogen gas at 0.5 V. vs. RHE calculated by Nernst equation.

## List of Tables

**Table 1-1.** Classification of fuel cell systems.

**Table 3-1.** XPS deconvolution data of carbon supported Pt and Pt-M (Au, Pd) NPs prepared by Al pitting corrosion method.

**Table 3-2.** XPS deconvolution data of carbon supported Pt and Pt-M (Au, Pd) NPs prepared by sodium borohydride method.

**Table 3-3.** EXAFS fitting data of ASP and HT Pd<sub>x</sub>Fe<sub>y</sub> samples by two-step synthesis.

**Table 3-4.** XPS Pd 3d deconvolution data of ASP and HT Pd<sub>x</sub>Fe<sub>y</sub> samples by two-step synthesis.

**Table 3-5.** EIS fitted data of MEAs.

**Table 3-6.** Physical and electrochemical properties of MEAs.



# Chapter 1. Introduction

---

## 1.1. Theoretical basis of Fuel Cells

Fuel cells are electrochemical energy conversion devices that can convert the chemical energy of fuels such as hydrogen or oxygen gas into electrical energy directly without any mechanical conversion processes. (Figure 1-1.) (1, 2) The first idea of fuel cell was demonstrated by Sir William Grove in February 1839. (3) Grove introduced the concept of hydrogen fuel cell by immersing two Pt electrodes on one end in a solution of sulfuric acid and the other two ends separately sealed in containers of oxygen and hydrogen, he found a constant current between the electrodes. In this experiment, hydrogen was oxidized and oxygen was reduced, respectively. Then, as the products, water and electricity were generated. This reaction is reversed water electrolysis. (Figure 1-2.) After this, Francis T. Bacon made a practical fuel cell system in 1937 and developed a 6 kW fuel cell in 1950. The first practical fuel cell application was conducted in the U.S. Space Program. General Electric invented the polymer electrolyte membrane fuel cell (PEMFC) and the fuel cell was used in NASA's Gemini program and Apollo Space Program. (4) Now, many researchers make great efforts to commercialize the fuel cell system.

As one of battery systems theoretically, fuel cell system is composed of both

electrodes (anode and cathode), where electrochemical reactions occur and DC electricity is generated directly. However, the fuel cell system is very different from the battery system such as lithium ion secondary battery in some aspects. Basically, the fuel cell system is open structure, which fuels and oxidants are supplied into the system constantly. In contrary to this, in traditional battery system, there is only limited reactant to produce electrical energy. In addition, because fuel cell system is energy conversion device, it cannot store electric energy produced by cell reaction, in contrast with traditional battery system.

Fuel cells have a lot of advantages such as no or less emission of pollutants like CO<sub>2</sub>, NO<sub>x</sub> and SO<sub>x</sub>, higher energy conversion efficiency up to 80 % compared to internal combustion engines. According to the fuels used for electrochemical reactions and power densities produced by, fuel cell system can be classified into various types. The types of fuel cell system are expressed in Table 1-1 and Figure 1-3. These can be categorized into five types according to their electrolytes and operating temperatures; alkaline fuel cells (AFC), phosphoric acid fuel cells (PAFC), solid oxide fuel cells (SOFC), molten carbonate fuel cells (MCFC), and polymer electrolyte membrane fuel cells (PEMFC).

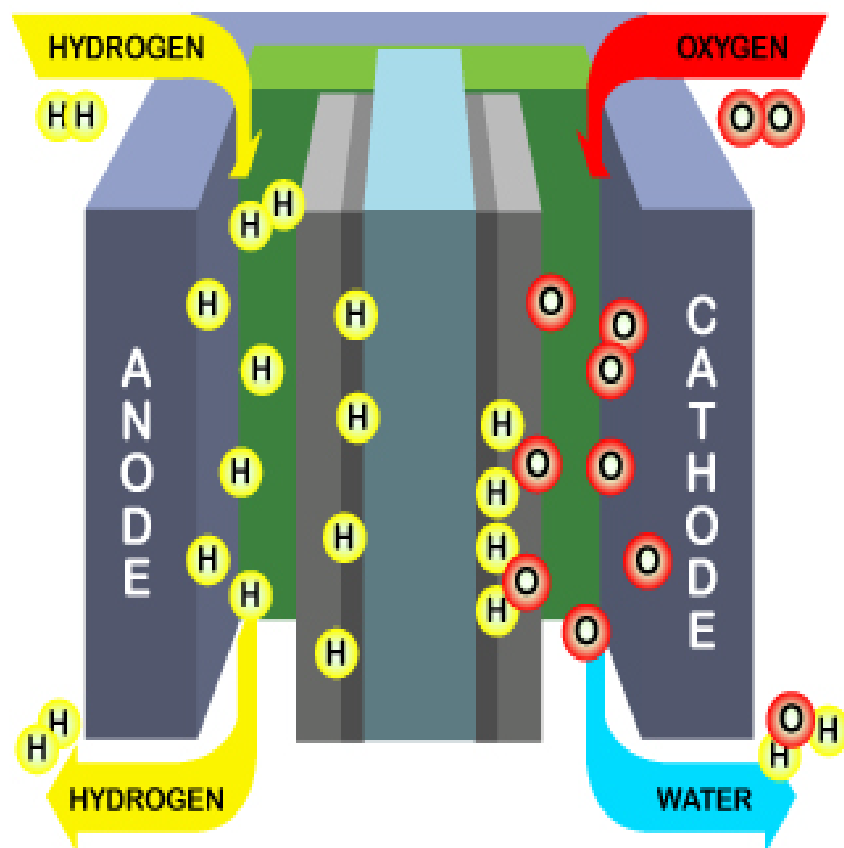


**Figure 1-1.** Schematic illustration of fuel cell.

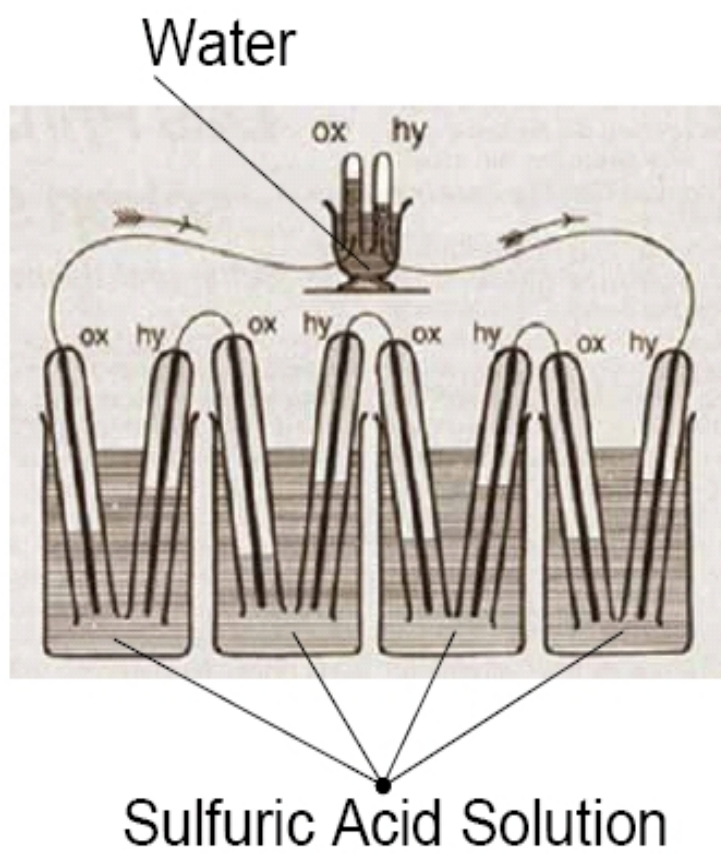


**Figure 1-2.** Sketch of William Grove's 1839 fuel cell system.

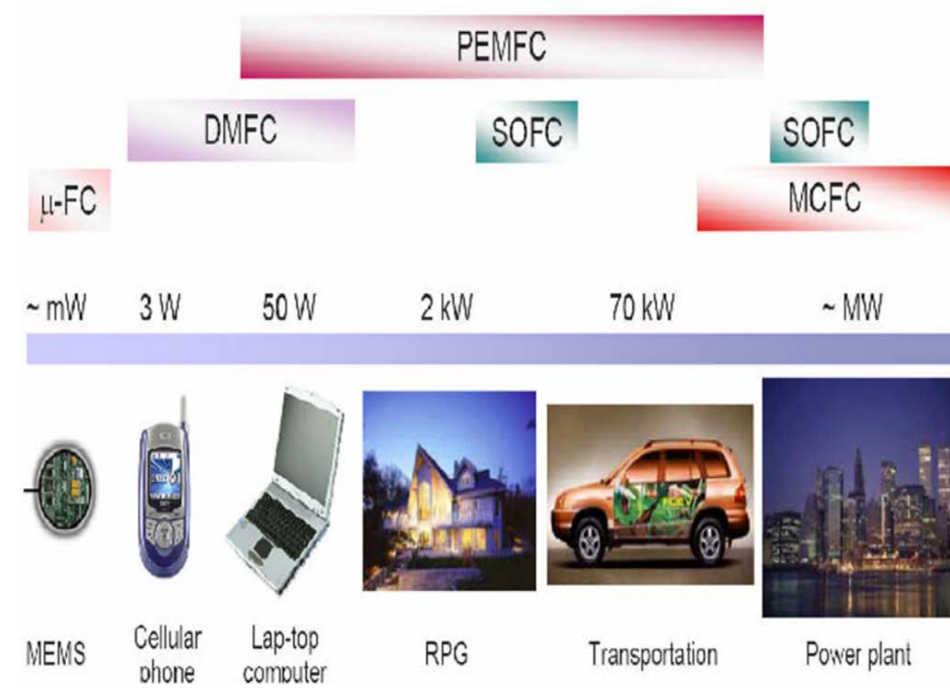


**Figure 1-3.** Classification of fuel cell systems according to their applications.

	PEMFC	PAFC	AFC	MCFC	SOFC
Electrolyte	Polymer Membrane	Liquid $\text{H}_3\text{PO}_4$ (Immobilized)	Liquid KOH (Immobilized)	Molten Carbonate	Ceramic
Charge Carrier	$\text{H}^+$	$\text{H}^+$	$\text{OH}^-$	$\text{CO}_3^{2-}$	$\text{O}^{2-}$
Operating Temperature	80 °C	200 °C	60-220 °C	650 °C	600-1000 °C
Catalyst	Platinum	Platinum	Platinum	Nickel	Perovskites (Ceramic)
Cell Components	Carbon-based	Carbon-based	Carbon-based	Stainless-based	Ceramic-based
Fuel Compatibility	$\text{H}_2$ , Methanol	$\text{H}_2$	$\text{H}_2$	$\text{H}_2$ , $\text{CH}_4$	$\text{H}_2$ , $\text{CH}_4$ , CO

**Table 1-1.** Classification of fuel cell systems.

## **1.2. Polymer electrolyte membrane fuel cells**

Among these fuel cell systems mentioned above, polymer electrolyte membrane fuel cell (PEMFC) has attracted many researchers' attentions for previous decades because of its many advantages compared to other fuel cell systems, conventional battery system and internal combustion engines. From the electrochemical reaction of hydrogen and oxygen gas feeds to anode and cathode, respectively, it generates electricity and water without any pollutants, exhibits high power density and operates relatively low temperature under  $\sim 100^\circ\text{C}$ . Due to these desirable properties, PEMFC can be applied to electric vehicle, portable devices and residential power systems, such as power supplies for laptop computers, cell phone, digital cameras and emergency electric power due to high coverage of various working voltages and various electric powers density generated. Basically, the PEMFC cell reaction of PEMFC is expressed in Figure 1-4. The cell reaction proceeds as follows. At anode, from hydrogen oxidation reaction (HOR), 2 moles of protons and 2 moles electrons are generated and produced proton move to cathode through Nafion membrane and electrons travel through external electric wire. At cathode, the electrochemical reduction reaction involves oxygen molecules, protons and electrons from anode reaction which produces water. This reaction called oxygen reduction reaction (ORR) is highly irreversible reaction in acidic condition, unlike HOR at anode, with low exchange current density (range of  $10^{-10}$ -

$10^{-11} \text{ A cm}_{\text{Pt}}^{-2}$ ) and because of this, electrochemical reaction at cathode is regarded as rate determining step (RDS) in PEMFC reactions. (5-7)

The overall reaction of PEMFC is affected by the overpotentials in every component such as anode, cathode and electrolyte. The follows equation represents these aspects. (1, 2, 4)

$$E = E_0 - \eta_{act,a} - \eta_{act,c} - \eta_{ohm} - \eta_{mt,a} - \eta_{mt,c}$$

where  $E_0$  is the thermodynamic reversible potential,  $\eta_{act,a}$  and  $\eta_{act,c}$  are the activation overpotentials related to the charge transfer at the anode and cathode, respectively resulted from electrochemical reactions. The terms  $\eta_{ohm}$  is the ohmic overpotential in electrolyte and interfaces between each cell component,  $\eta_{mt,a}$  and  $\eta_{mt,c}$  are the mass transfer overpotentials at the anode and cathode, respectively caused by mass transport properties. Among above overpotentials it has been known that  $\eta_{act,c}$ , the slow ORR, is the main reasons for potential losses during the PEMFC operation. The polarization curve of PEMFC is shown in Figure 1-5. This curve can be divided into three regions according to the overpotentials related.

i) Activation overpotential region : The reasons of this are hydrogen oxidation kinetics and oxygen reduction kinetics at the anode and cathode, respectively. In other words, the overpotentials related to these kinetics slow the reactions at each electrode and can be determined by the activity of electrocatalyst at each electrode.



In addition, these overpotentials are expressed as a sudden drop of single cell potential at low current density region.

ii) Ohmic loss region : The reasons of this are resistance in proton and electron pathway via electrodes and polymer electrolyte or interfacial resistance between cell components. Due to this, the cell voltage decreases linearly at middle region of polarization curve. This can be mitigated by the structural and material modification of polymer electrolyte membranes and electrodes.

iii) Concentration loss region : At this region, the cell reactions are fast to use up hydrogen and oxygen of each electrode, resulting in mass transport limiting current density. In addition, due to generated water at the cathode, flooding occurs and it makes oxygen supply harder than before. This is expressed as a fast drop of cell potential at high current density region and can be mitigated by the structural modification of electrodes or operating conditions.

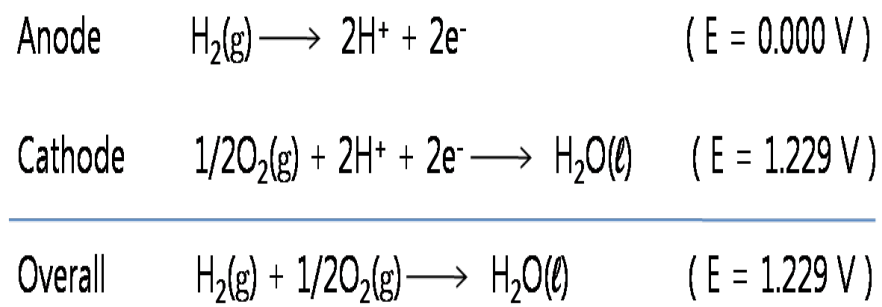


**Figure 1-4.** Cell reaction of PEMFC.

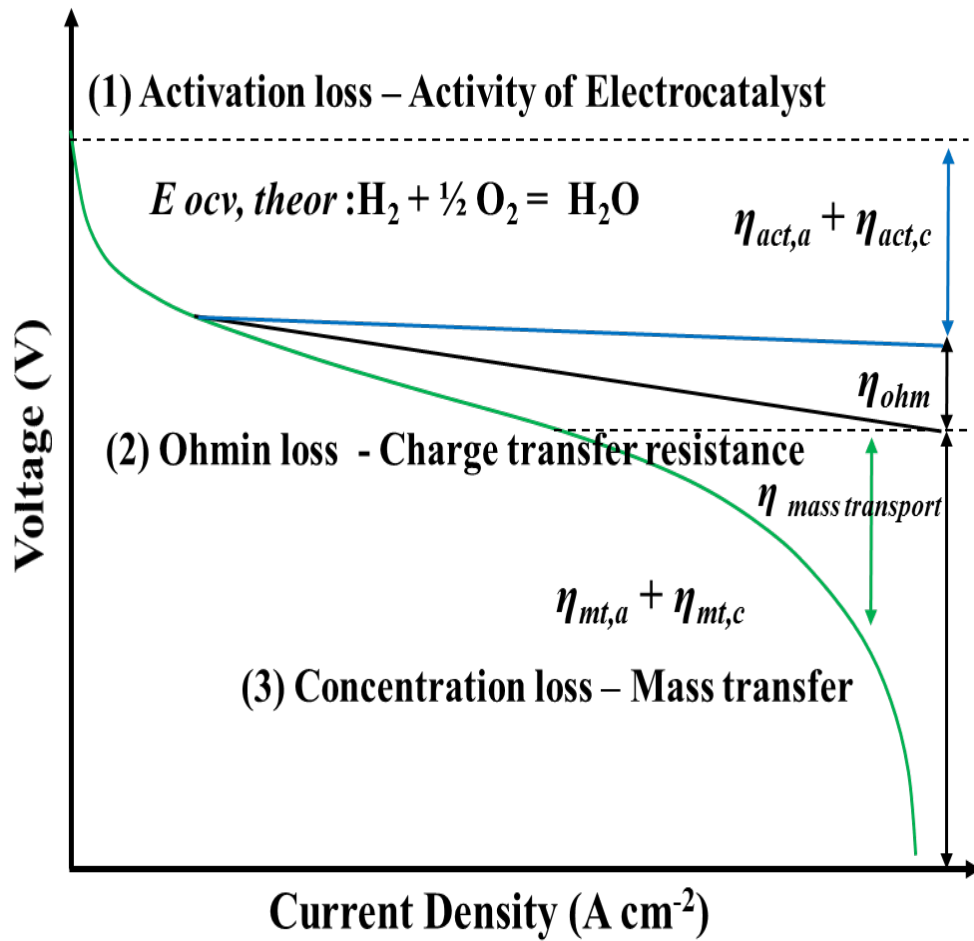


**Figure 1-5.** Polarization curve of PEMFC and three major losses during the cell operation.

### 1.3. Recent development of electrocatalyst and electrode structure

For the operation of PEMFC, the electrocatalyst and the electrode structure are key components because they engage the electrochemical reactions such as HOR or ORR. One of the electrocatalysts for these reactions, platinum group metals such as Pt and Pd are believed as best electrode materials for PEMFC, especially for ORR. Especially, among these reactions at each electrode, ORR is much more important than HOR for the enhancement of PEMFC performance due to its slow reaction kinetics. During the ORR, four electrons involve and the reaction mechanism is much complex because of the strong O-O bond breaking, the formation of Pt (or Pd) oxide species, the generation of hydrogen peroxide as a side product and so on. (8-11) The overall ORR in acid electrolyte is as follows.



During the past two decades, many researchers have studied about the activity improvement of Pt electrocatalyst and PEMFC single cell via alloying Pt with other transition metals (Ni, Co, Fe etc), Pt shell - transition metal core structure, modifications of surface and electronic structures of NPs via additional post treatment such as acid treatment or heat treatment (so called Pt skeleton and Pt skin structure). (12-26) In addition, to use less or no amount of Pt metal, the researches

for substitution Pt of less expensive electrocatalyst such as non-noble transition metal alloy or their oxides, carbon-supported transition metal/nitrogen (M-N-C) materials and conductive polymers which are primarily intended for lowering the cost of the PEMFC while possessing high ORR activity. (27-40) (Figure 1-6) These many electrocatalyst modification approaches are related to the improvement of activation loss of PEMFC polarization curve mentioned above.

In the aspect of electrode structures and systems, in addition, many studies related to the modifications of electrode catalyst layer and polymer electrolyte structures such as the usage of pore-forming agent, patterned Nafion membrane and ordered structure of Pt catalyst without the modifications of electrocatalyst itself. (41-49) (Figure 1-7) These researches are related to the decrease of ohmic loss and concentration loss of PEMFC polarization curve and can improve accessibility of electrocatalyst for electrochemical reaction and utilization of Pt group metal electrocatalysts.

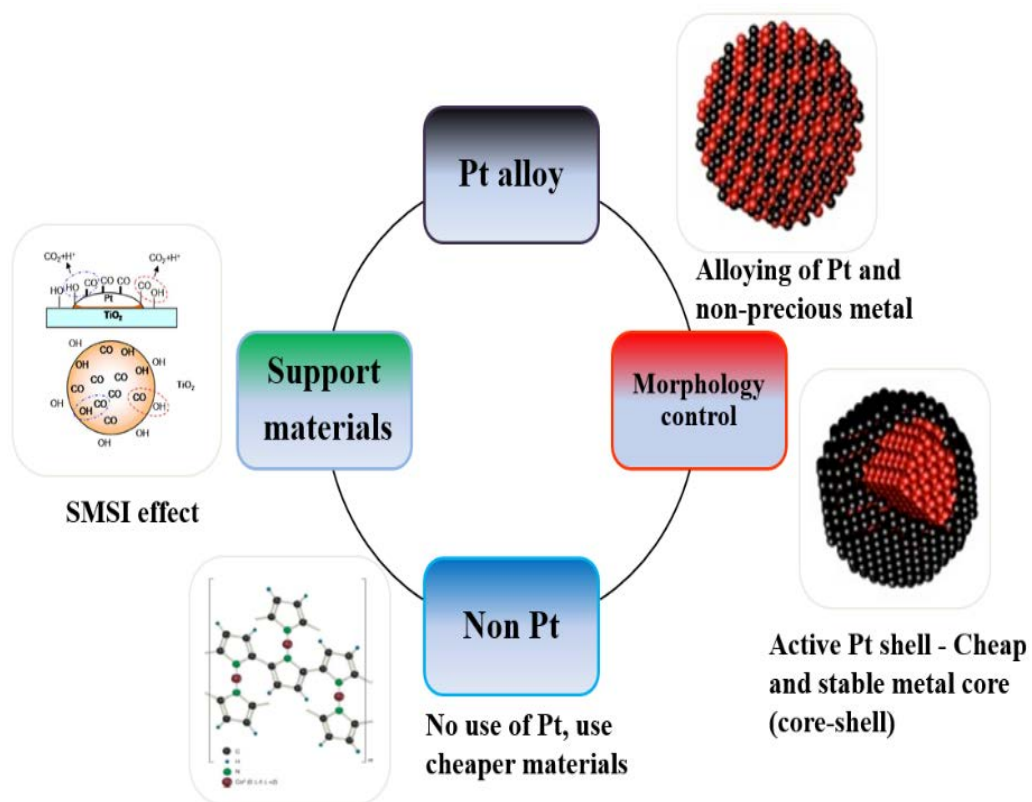


**Figure 1-6.** Classification of the researches related to electrocatalyst for PEMFC.

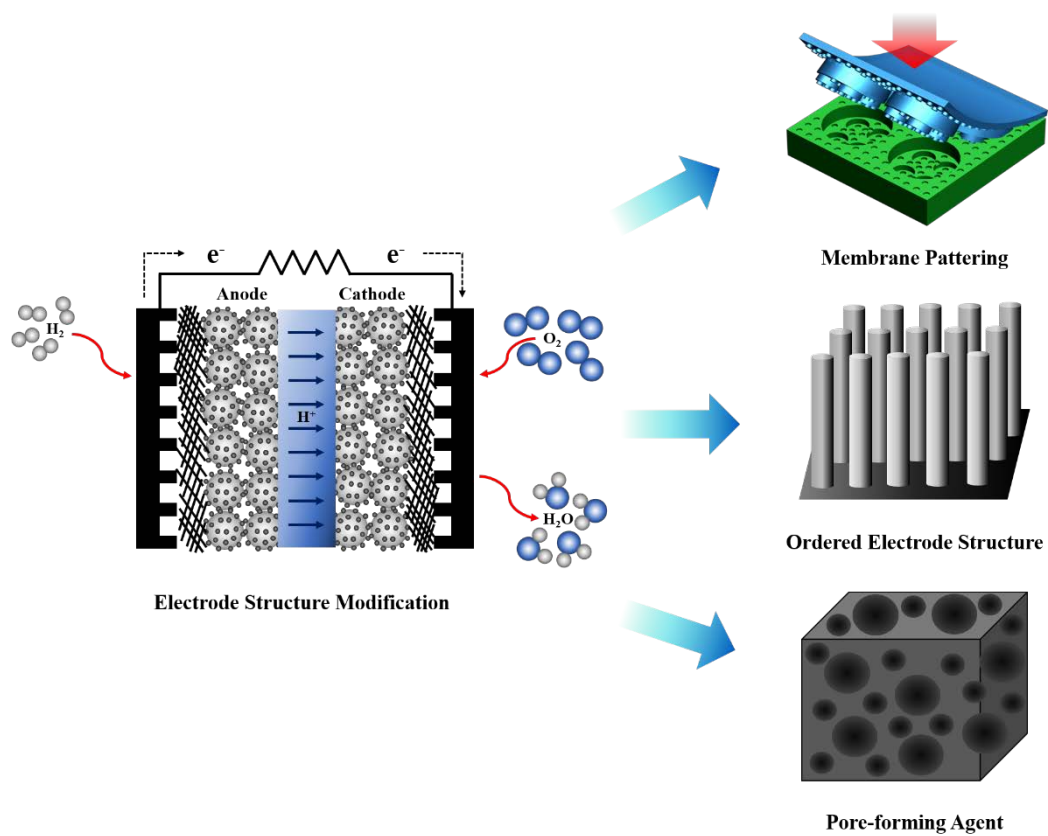


**Figure 1-7.** Classification of the researches related to structural modifications of electrode of PEMFC.

## **1.4. Objectives of this study**

In this study, the novel methodologies for the enhancement of PEMFC performance via atomic scale and macroscale approaches are suggested. First, in case of atomic scale approaches focusing on electrocatalyst itself for the improvement of activation loss of PEMFC, the novel synthetic methods of Pt bimetallic alloy nanoparticles (NPs) via Al pitting corrosion method and fabrication of highly active palladium-iron (PdFe) alloy NPs via modified two-step chemical synthesis were proposed. It is reported that highly dispersed palladium (Pd) nanoparticles on carbon black can be synthesized by using metallic aluminum (Al) as a reducing agent resulted from pitting corrosion phenomenon. (50) Al metal as a reducing agent has many advantages such as a good reducing capability, easy transportation and storage because of its solid form and spontaneous oxide film formation under ambient condition. By utilizing this novel synthesizing method, carbon supported Pt and Pt-M (Au,Pd) NPs were fabricated very easily without any complex conditions and samples were analyzed via physical, chemical and electrochemical analysis. Besides, to clearly find out advantages and disadvantages of Al pitting corrosion method for synthesizing Pt bimetallic alloy NPs, physical and electrochemical properties of Pt bimetallic alloy NPs prepared via conventional sodium borohydride method were compared to those of samples of Al pitting corrosion method. Additionally, post heat treatments with various conditions were



conducted to elucidate the relationship between ORR activity and atomic structure of electrocatalyst. Next, highly active and cheap PdFe alloy NPs were synthesized via modified two-step chemical synthesis method, which combines polyol reduction method and conventional sodium borohydride method. PdM (M=Fe, Co, Ni, Ti and Cu) bimetallic alloy materials have attracted recent attention because of their many advantages, such as much cheaper material price, higher estimated reserves and similar or better catalytic properties compared to Pt. (51-58) In addition, the effect of post heat treatment on ORR activity was analyzed by using physical and electrochemical measurements. By the heat treatment, PdFe NPs exhibited intermetallic structures with Pd rich surface shell and ordered PdFe core. Due to this structural modifications, heat treated PdFe NPs exhibited the downshift of d-band center of Pd and, as a result, higher ORR activity compared to as prepared PdFe NPs and conventional carbon supported Pt catalyst.

Next, as a macroscale approach for modification of catalyst layer and polymer electrolyte structures for the improvement of ohmic loss and concentration loss of PEMFC, multiscale approach for enhancing performance of PEMFC were applied and optimized. Multiscale surface is the distinct structure in nature, giving unique properties including superhydrophobicity, directional adhesion, antifogging, directional wettability and structural color. (59-63) These special functions from multiscale structure have been focused on and many researches on this have been conducted for decades. In addition, the studies related to the structural

modifications of catalyst layer and polymer electrolyte structures were reported for many years, such as the usage of pore-forming agent, patterned Nafion membrane and ordered structure of Pt catalyst without the modifications of electrocatalyst itself, as mentioned above. In this study, with an aid of multiplex lithography that integrates rational advantages in both microscale and nanoscale, complex and multiscale architectures was embedded into polymer electrolyte membrane of PEMFC via thermal imprinting process. From the mechanical measurements, the prepared multiscale Nafion membrane exhibited enhanced physical properties due to its multiscale structure. The membrane electrode assembly (MEA) with multiscale patterned Nafion membrane exhibited high utilization of Pt due to increased electrochemically active surface area (ECSA) and decrease of proton pathway in thinned polymer electrolyte membrane. The effects on enhanced PEMFC performance were proved by using physical and electrochemical measurements such as scanning electron microscopy (SEM), cyclic voltammogram (CV), electrochemical impedance spectroscopy (EIS) and etc. In addition, for realistic applications of PEMFC such as automotive, we conducted accelerated durability test (ADT) to mimic actual operating condition of PEMFC by potential cycling according to DOE protocols. (64) After ADT, MEA with multiscale membrane still exhibited higher performance than conventional one, which means multiscale approach for PEMFC can be one of the best ways to increase PEMFC performance and utilization of Pt.

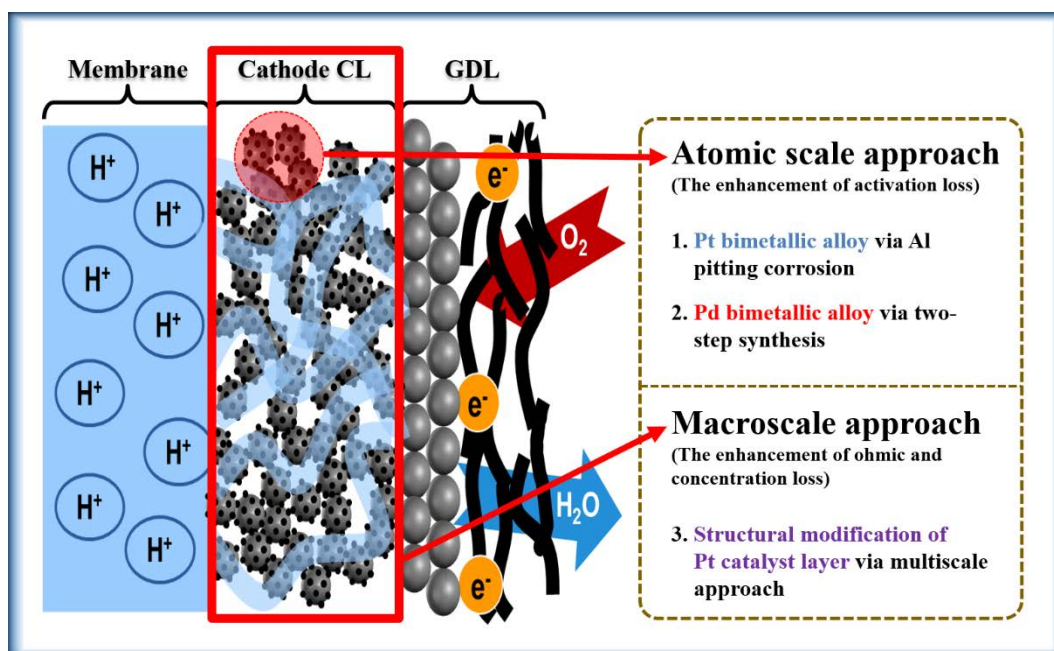


**Figure 1-8.** Objectives of this study according to the approaches of different scale.

## Chapter 2. Experimental

---

### 2.1. Platinum Bimetallic Alloy Electrocatalyst synthesized by Al Pitting Corrosion method

#### 2.1.1. Synthesis of carbon supported Pt and Pt-M (Au, Pd) NPs

Carbon supported Pt and Pt-M (Au, Pd) (40 wt.%) NPs were prepared via Al pitting corrosion method proposed by Manthiram et al. Materials for the synthesis are as follows; carbon black (Vulcan XC-72R, Carbot), DI water (18.2 MΩ cm, Millipore), sodium citrate as support, solvent and capping agent. These were dispersed by using a magnetic stirrer and an ultrasonic bath for 1 h. After this step, sample of chloroplatinic acid hexahydrate ( $\text{H}_2\text{PtCl}_6 \cdot 6\text{H}_2\text{O}$ ), gold (III) chloride trihydrate ( $\text{HAuCl}_4 \cdot 3\text{H}_2\text{O}$ ) and sodium tetrachloropalladate (II) ( $\text{Na}_2\text{PdCl}_4$ ) were added to the solution and stirred for 1 h. In the final step, Al foil as a reducing agent was added and stirred for 24 h to end up the reduction reaction completely. After finishing every step, the solution was filtered, washed with DI water and dried in a vacuum desiccator. To eliminate Al foil residue produced during the synthesis, additional acid treatment was conducted in 0.5 M  $\text{HClO}_4$  solution for 24 h and secondary filtering with DI water was conducted. The as prepared samples were also dried in a vacuum desiccator for more than 6 h. The atomic ratio of Pt to M

(Au, Pd) was fixed as 3:1. All chemicals were purchased from Sigma-Aldrich and used as received. The schematic illustration of the synthesis is shown in Figure 2-1 (a). In addition, for comparison, Pt and Pt-M (Au, Pd) NPs were synthesized via conventional sodium borohydride method and physical and electrochemical measurements on the prepared samples were conducted.

### **2.1.2. Post heat treatment of Pt and Pt-M (Au, Pd) NPs**

Structural modifications of carbon supported Pt and Pt-M (Au, Pd) NPs were induced via post heat treatment under various conditions to elucidate the effect of atomic ordering for ORR activity. At first, every sample was heat treated at 150 °C for 2 h under H<sub>2</sub>/Ar (the mixture of 5 % H<sub>2</sub> and 95 % Ar) atmosphere to fully reduce their surface, which were largely oxidized due to additional acid treatment. In sequence, there were 2 additional heat treatment conditions; i) to induce fully ordered structure, NPs were received heat treatment at 500 °C for 1 h under H<sub>2</sub>/Ar atmosphere, ii) to segregate Pt atoms to their surface and for additional increase in ORR activity, the heat treatment was conducted at 150 °C for 1 h under CO (99.9 % ) atmosphere. NPs in this study were denoted as Pt/C or Pt<sub>3</sub>M (Au, Pd)/C ASP, Pt/C or Pt<sub>3</sub>M (Au, Pd)/C H<sub>2</sub>, Pt/C or Pt<sub>3</sub>M (Au, Pd)/C 500 and Pt/C or Pt<sub>3</sub>M (Au, Pd)/C CO according to conditions of the heat treatments. The schematic illustration of the heat treatment process is shown in Figure 2-1 (b).

### **2.1.3. Membrane electrode assembly (MEA) preparation**

A catalyst slurries for the anode and cathode catalyst layer were fabricated by mixing 40 wt.% Pt/C (Johnson Matthey) and synthesized Pt and Pt-M (Au, Pd) NPs NPs, Nafion ionomer solution and 2-propanol (Sigma Aldrich). Nafion 212 membrane (Dupont) was used after the pretreatment. They were boiled in 3 % hydrogen peroxide solution, and rinsed in D.I. water. After that, they were soaked in 0.5 M H<sub>2</sub>SO<sub>4</sub>, and washed again in D.I. water. Each procedure in the solutions was performed at 80 °C for 1 h, respectively. The prepared catalyst slurries were sprayed onto the anode and cathode parts of the Nafion membrane. The catalyst loadings were equally 0.12 mg cm<sup>-2</sup> in the anodes and cathodes of the MEAs, respectively. The catalyst-coated membranes (CCMs) were dried at room temperature for 12 h, and sandwiched between the anode and cathode gas diffusion layers (GDLs, SGL 35 BC) without hot press process. The active geometric areas of the MEAs were 5.0 cm<sup>2</sup>.

### **2.1.4. Physical characterization of carbon supported Pt and Pt-M (Au, Pd) NPs**

Crystalline structure of carbon supported Pt and Pt-M (Au, Pd) NPs were examined by X-ray diffraction (XRD) using Rigaku D/MAX 2500 operated with a Cu K $\alpha$  radiation (40 kV, 200 mA). The size and morphology of carbon supported Pt and Pt-M (Au, Pd) NPs were confirmed by transmission electron microscopy

(TEM) using JEM 2100F (JEOL) and their chemical compositions were further analyzed by energy-dispersive X-ray spectroscopy (EDX) with Tecnai F20 (FEI). Samples were prepared by placing a drop of catalyst solution onto a carbon-coated holey copper grid that was subsequently dried in an oven for more than 12 h. X-ray photoelectron spectroscopy (XPS, Thermo Sigma Probe) measurements were conducted with Al Ka as the X-ray beam source. All spectra were calibrated by C 1s at 285 eV as a reference. The peaks for each sample were deconvoluted by using XPSPEAK 4.1 software. Inductively coupled plasma-atomic emission spectral (ICP-AES, Shimadzu JP/ICPS-7500) analysis was conducted for quantitative analysis of chemicals.

#### **2.1.5. Electrochemical measurements of carbon supported Pt and Pt-M (Au, Pd) NPs**

The NPs ink was prepared by mixing 0.01 g of carbon supported Pt and Pt-M (Au, Pd) NPs with DI water (18.2 MΩ cm; Millipore), 5 wt.% Nafion ionomer solution as a binder, and isopropyl alcohol (IPA) (Sigma–Aldrich). 3 μL of slurry was pipetted and dropped onto a glassy carbon rotating disc electrode (geometric surface area 0.196 cm<sup>2</sup>). (65) Electrochemical measurements were carried out using an Autolab potentiostat (PGSTAT101) with a conventional three-electrode electrochemical cell comprised of a glassy carbon working electrode, a Pt wire

counter electrode, and a saturated calomel reference electrode (SCE). All electrochemical measurements are quoted with respect to reversible hydrogen electrode (RHE) and were conducted at 293 K. After the electrochemical cell was purged with Ar for 30 min, cyclic voltammogram was obtained at a potential range of 0.05 to 1.05 V vs. RHE with a scan rate of 20 mV/s in 0.1 M HClO<sub>4</sub> under Ar purging. ORR polarization curves were obtained using a rotation disk electrode (RDE, Pine Research Instrumentation) at 1600 rpm, in the range from 0.05 to 1.05 V vs RHE with a scan rate of 5 mV/s in 0.1 M HClO<sub>4</sub> under an O<sub>2</sub> flow. ORR polarization curves and the corresponding activities are reported after the iR-compensation. CO oxidation and N<sub>2</sub>O reduction analysis was conducted using CV at potentials of 0.05 to 1.05 V and 0.05 to 0.7V vs. RHE at a scan rate of 20 and 50 mV/s. CO gas was purged for 15 min to adsorb CO molecules on Pt and Pt-M (Au, Pd) NPs and subsequent Ar gas was purged for 30 min to eliminate extra CO molecules in electrolyte. N<sub>2</sub>O gas was bubbled into the electrolyte for 15 min to saturate the electrolyte before the measurement and the N<sub>2</sub>O flow was maintained during the experiment. Methanol oxidation reaction (MOR) test was conducted in the range from 0.05 to 1.05 V vs RHE with a scan rate of 20 mV/s in 0.1 M HClO<sub>4</sub> with 1.0 M CH<sub>3</sub>OH and 5<sup>th</sup> curves of measured data were used for comparison.

For the single cell performance test, fully humidified H<sub>2</sub> and O<sub>2</sub> (air) gas were supplied into the anode and cathode, respectively. The stoichiometric coefficient of



H<sub>2</sub>/O<sub>2</sub> was 2.0/9.5, with total outlet pressure of ambient. Single cell temperature was maintained at 80 °C according to DOE condition.

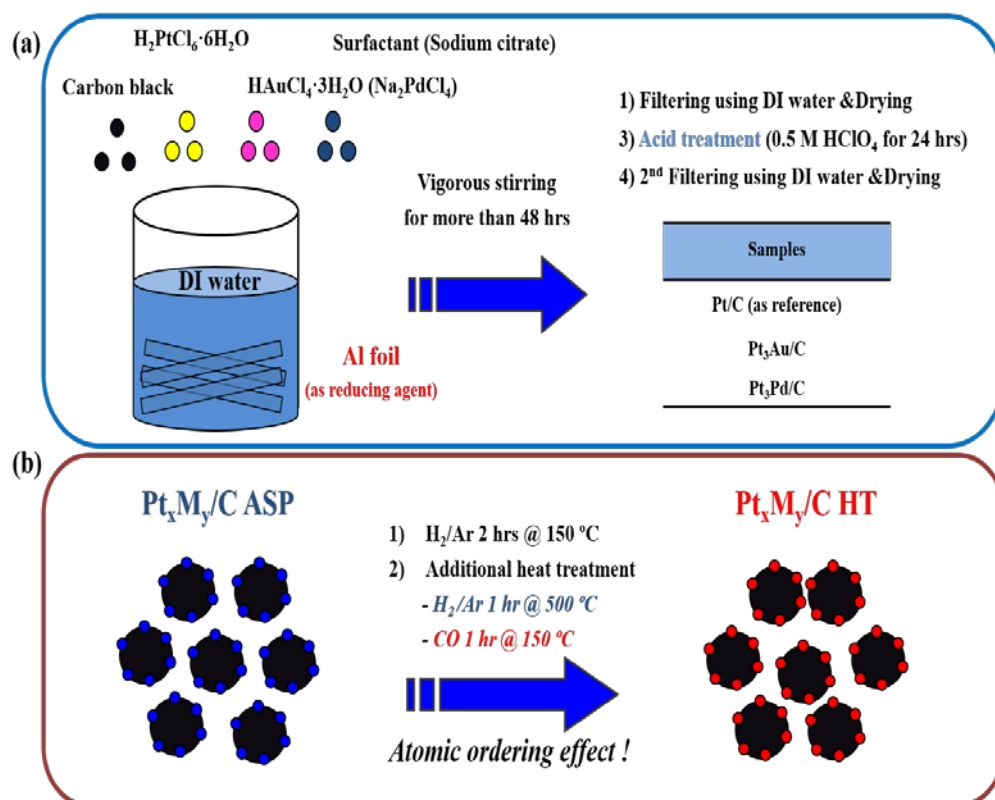


**Figure 2-1.** Schematic illustration of (a) the synthesis via Al pitting corrosion method and (b) the heat treatment process.

## **2.2. Palladium-Iron Alloy Electrocatalyst via Modified Chemical Synthesis**

### **2.2.1. Synthesis of carbon supported Pd<sub>x</sub>Fe<sub>y</sub> NPs**

Carbon supported PdFe (40 wt.%) NPs were prepared via a two-step reduction process. Carbon supported PdFe NPs were synthesized by polyol reduction method using 1,2-propanediol as solvent and reducing agent. Carbon black (Vulcan XC-72R) and oleylamine as a stabilizer, were dispersed in 1,2-propanediol using a magnetic stirrer and an ultrasonic bath. (66, 67) In sequence, certain amounts of Pd (II) acetylacetonate and Fe (II) acetylacetonate were added to the mixture solution and the solution was kept in stirring condition for 6 h. After ultrasonic treatment, the solution was heated up to 110 °C in a three neck flask under an Ar atmosphere and it was maintained at the temperature for 1 h to purge remaining water out of the solution. Then, additional NaBH<sub>4</sub> was added to the heated solution under vigorous stirring circumstances. After that, the solution was held for 1 h to complete the nucleation. The mixture was then heated up to 165 °C and remained at the temperature for 2 h for complete reduction of the precursors. After cooling down to room temperature naturally, the solution was filtered, washed with ethanol, and dried in a vacuum desiccator. The amounts of Pd and Fe precursors were calculated to produce Pd:Fe atomic ratios of 3:1, 1:1, and 1:3. Hereafter, the as prepared PdFe NPs are designated as ASP Pd<sub>x</sub>Fe<sub>y</sub>, where x and y denote the ratio of Pd and Fe. All

chemicals were purchased from Sigma-Aldrich and used without further purification processes. The schematic illustration of the synthesis is shown in Figure 2-2 (a). In addition, to find out the difference between one-step polyol method and two-step modified method,  $\text{Pd}_x\text{Fe}_y$  NPs were synthesized at  $165^\circ\text{C}$  for 1 h without the addition of sodium borohydride and physical and electrochemical measurements were conducted.

### **2.2.2. Post heat treatment of carbon supported $\text{Pd}_x\text{Fe}_y$ NPs**

ASP samples were heated in a tube furnace at  $500^\circ\text{C}$  for 2 h under 5 vol. %  $\text{H}_2$  in Ar- $\text{H}_2$  mixture gas to trigger the surface-segregation of Pd. Subsequently, samples were cooled down to room temperature under Ar atmosphere. The resulting post heat-treated  $\text{Pd}_x\text{Fe}_y$  is denoted as HT  $\text{Pd}_x\text{Fe}_y$ . The schematic illustration of the heat treatment process is shown in Figure 2-2 (b).

### **2.2.3. Membrane electrode assembly (MEA) preparation**

A catalyst slurries for the anode and cathode catalyst layer were fabricated by mixing 40 wt.% Pt/C (Johnson Matthey) and synthesized  $\text{Pd}_x\text{Fe}_y$  NPs, Nafion ionomer solution and 2-propanol (Sigma Aldrich). Nafion 212 membranes (Dupont) were used after the pretreatment. They were boiled in 3 % hydrogen peroxide

solution, and rinsed in D.I. water. After that, they were soaked in 0.5 M H<sub>2</sub>SO<sub>4</sub>, and washed again in D.I. water. Each procedure in the solutions was performed at 80 °C for 1 h, respectively. The prepared catalyst slurries were sprayed onto the anode and cathode parts of the Nafion membrane. The catalyst loadings were equally 0.12 mg cm<sup>-2</sup> in the anodes and cathodes of the MEAs, respectively. The catalyst-coated membranes (CCMs) were dried at room temperature for 12 h, and sandwiched between the anode and cathode gas diffusion layers (GDLs, SGL 35 BC) without hot press process. The active geometric areas of the MEAs were 5.0 cm<sup>2</sup>.

#### **2.2.4. Physical characterization of carbon supported Pd<sub>x</sub>Fe<sub>y</sub> NPs**

The size and morphology of carbon supported Pd<sub>x</sub>Fe<sub>y</sub> NPs were confirmed by transmission electron microscopy (TEM) using JEM 2100F (JEOL). Samples were prepared by placing a drop of sample solution onto a carbon-coated holey copper grid that was subsequently dried in an oven. Crystalline structure of carbon supported Pd<sub>x</sub>Fe<sub>y</sub> NPs were examined using high resolution powder diffraction (HRPD) measured at the 9B HRPD beamline of the Pohang Light Source II (PLS-II, Korea) and X-ray diffraction (XRD) using Rigaku D/MAX 2500 operated with a Cu K $\alpha$  radiation (40 kV, 200 mA). The incident X-rays were vertically collimated using a mirror and were monochromatized to a wavelength of 1.5495 Å using a double-crystal Si (1 1 1) monochromator. Each specimen of approximately 0.2 g of

powder was prepared by flat plate side loading method to avoid the preferred orientation, and the sample was then rotated about the normal to the surface during the measurement to increase sampling statistics. A step scan was performed at room temperature from  $5^\circ$  in  $2\theta$  with  $0.02^\circ$  increments and  $1^\circ$  overlaps to the next detector bank up to  $126^\circ$  in  $2\theta$ . In order to accurately determine the phases contained in the samples and to determine lattice parameters, HRPD patterns were fitted by the whole-pattern profile matching method, in which the system was modeled as multiphases. X-ray absorption spectroscopy (XAS) of Pd K-edge and Fe K-edge was measured at 7D and 8C beamlines of PLS-II. A Si (111) monochromator crystal was used with intensity detuned to 70 – 85 % to eliminate high-order harmonics. The XAS data were collected in transmission modes. All measurements were calibrated with a reference Pd or Fe foil. The spectra were processed using Athena and Artemis software of the IFEFFIT package. (68) EXAFS spectra were fitted with fcc structure model (space group : Fm3m) of  $\text{Pd}_x\text{Fe}_y$  using the FEFF6 code. A lattice constant of 3.89 Å for Pd-Pd was used. The Pd-Fe structure was constructed by replacing all the Pd atoms in the first shell of the Pd fcc structure by Fe atoms. Fitted parameters were the mean square relative displacement (Debye-Waller factor,  $\sigma^2$ ), the effective scattering lengths (R), and the change of reference energy ( $\Delta E$ ). The amplitude reduction factor ( $S_0^2$ ) was fixed to 0.8. The r-range for fitting was 1.6 - 2.9 Å. X-ray photoelectron spectroscopy (XPS) were measured at 8A1 beamline of PLS-II. All spectra were calibrated by C 1s at

284.6 eV. The obtained spectra were deconvoluted by using the XPSPEAK 4.1 software. The elemental analysis was carried out with an inductively coupled plasma atomic emission spectrometer (ICP-AES, Shimadzu JP/ICPS-7500).

#### **2.2.5. Electrochemical measurements of carbon supported Pd<sub>x</sub>Fe<sub>y</sub> NPs**

The catalyst ink was prepared by mixing the catalyst with DI water (18.2 MΩ cm; Millipore), 5 wt.% Nafion ionomer solution as a binding material, and isopropyl alcohol (IPA) (Sigma–Aldrich). 3 μL of slurry was pipetted and dropped onto a glassy carbon electrode (geometric surface area 0.196 cm<sup>2</sup>). Electrochemical measurements were carried out using an Autolab potentiostat (PGSTAT101) with a conventional three-electrode electrochemical cell comprised of a glassy carbon working electrode, a Pt wire counter electrode, and a saturated calomel reference electrode (SCE). All electrochemical measurements are quoted with respect to reversible hydrogen electrode (RHE) and were conducted at 293 K. After the electrochemical cell was purged with Ar for 30 min, cyclic voltammogram (CV) was obtained at a potential range of 0.05 to 1.05 V vs. RHE with a scan rate of 20 mV/s in 0.1 M HClO<sub>4</sub> under Ar purging. ORR polarization curves were obtained using a rotation disk electrode (RDE, Pine Research Instrumentation) at 1600 rpm, in the range from 0.05 to 1.05 V vs RHE with a scan rate of 5 mV/s in 0.1 M HClO<sub>4</sub> under an O<sub>2</sub> flow. ORR polarization curves and the corresponding activities are

reported after the iR-compensation. CO oxidation and N<sub>2</sub>O reduction analysis was carried out using CV at potentials of 0.05 to 1.05 V and 0.05–0.7V vs. RHE at a scan rate of 20 and 50 mV/s. CO gas was purged for 15 min to adsorb CO molecules on Pd<sub>x</sub>Fe<sub>y</sub> NPs and subsequent Ar gas was purged for 30 min to eliminate extra CO molecules in electrolyte. N<sub>2</sub>O gas was bubbled into the electrolyte for 15 min to saturate the electrolyte before the measurement and the N<sub>2</sub>O flow was maintained during the experiment. The electrochemical performances of the prepared samples were compared with those of a commercial Pt/C catalyst (40 wt.%, Johnson Matthey).

For the single cell performance test, fully humidified H<sub>2</sub> and O<sub>2</sub> (air) gas were supplied into the anode and cathode, respectively. The stoichiometric coefficient of H<sub>2</sub>/O<sub>2</sub> was 2.0/9.5, with total outlet pressure of ambient. Single cell temperature was maintained at 80 °C according to DOE condition.



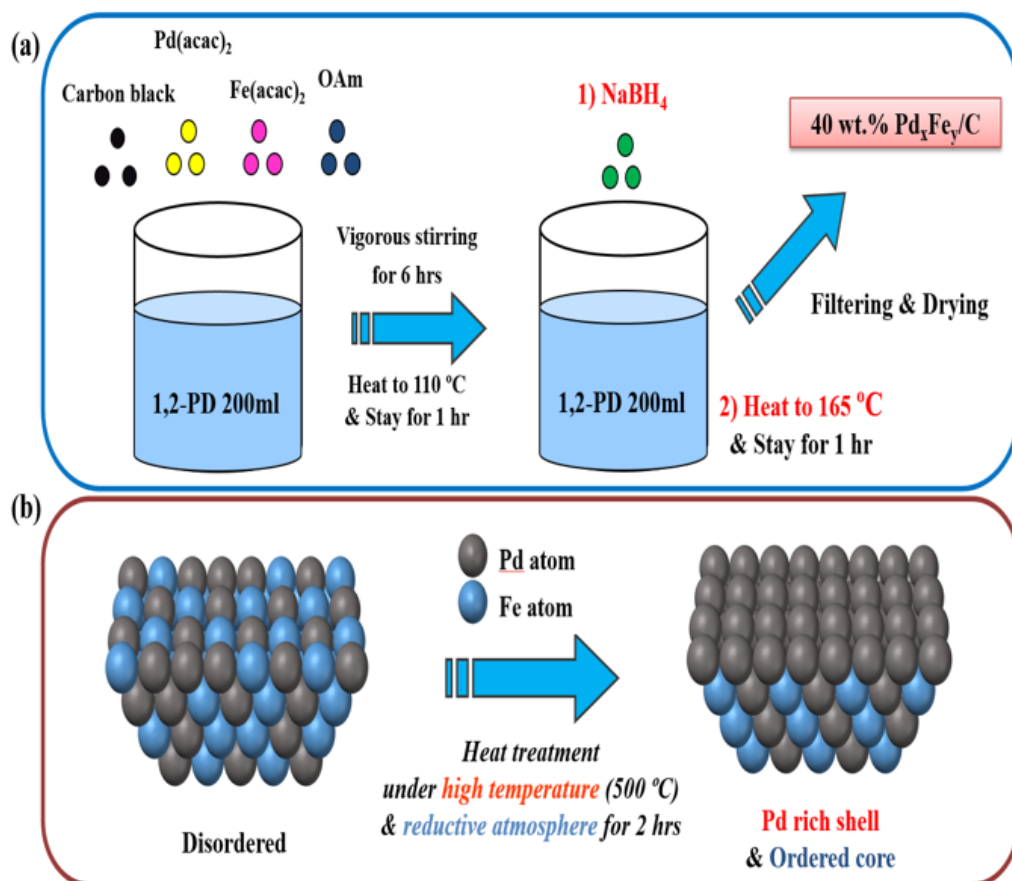


**Figure 2-2.** Schematic illustration of (a) the two-step synthesis and (b) the heat treatment process.

## **2.3. Polymer Electrolyte Membrane Fuel Cell with Multiscale Nafion membrane**

### **2.3.1. Preparation of hierarchical structure**

The hole patterned silicon masters were fabricated by photolithography and reactive ion etching. The masters were treated with a fluorinated-SAM solution ((tridecafluoro-1,1,2,2-tetrahydrooctyl)-trichlorosilane : FOTCS, Gelest Corp.) diluted to 0.03 M in anhydrous heptane in an Ar chamber. After the surface treatment the masters were annealed at 120°C for 20 min. After the preparation of the master, a mixture of base and curing agent (10:1 w/w) of Sylgard 184 PDMS elastomer (Dupont) was poured onto the patterned masters and cured at 70 °C for 2 h. The cured PDMS molds were peeled off from the master and cut prior to use.

A small amount of hydrophilic resin (PUA311, Minuta Tech) was drop-dispensed onto a patterned PDMS mold, and a flat PDMS upper mould was uniformly placed onto patterned PDMS mold. Then, the sandwich assembly was exposed to UV light ( $< 3$  min,  $\lambda = 250\sim 400$  nm, Fusion Cure System, Minuta Tech) under an applied pressure ( $25\text{ g cm}^{-2} \sim 1\text{ kg cm}^{-2}$ ) after forming conformal contact. After removal of the upper and lower PDMS molds, a flexible, free-standing membrane with dual phase polymeric membrane via micro ebb-tide phenomena was obtained.

A prepared dual phase polymeric membrane was uniformly placed onto nanopatterned PUA311 mold contacting with more cured face ( $\alpha$  phase) of the

membrane and nanopatterned PDMS mold was placed onto the less cured face ( $\alpha'$  phase) of the membrane. Then, the sandwich assembly was exposed to UV light ( $> 3$  min,  $\lambda = 250\sim 400$  nm) with hydraulic pressure ( $6\sim 8$  kg cm $^{-2}$ ) in a vacuum chamber ( $5\times 10^{-2}$  Torr) after forming conformal contact. After removal of the PDMS molds, multiscale two-level PUA311 hole pattern array via simultaneous bonding and imprinting process was obtained. The same process was conducted with different micro-sized membrane to obtain tri-level PUA311 hole patterned master. After the preparation of the master, a mixture of base and curing agent (10:1 w/w) of Sylgard 184 PDMS elastomer was poured onto the patterned masters and cured at  $70\text{ }^{\circ}\text{C}$  for 2 h. The cured PDMS molds were peeled off from the master and cut prior to use.

### **2.3.2. Preparation of multiscale Nafion membrane via thermal imprinting process**

Nafion membrane (Nafion 212, Dupont) was uniformly placed onto as-prepared multiscale PDMS mold and glass substrate. Then, the sandwich assembly was imprinted under hydraulic pressure ( $10\sim 20$  kg cm $^{-2}$ ) and temperature ( $\sim 120\text{ }^{\circ}\text{C}$ ) for 30 min. After cooling down to room temperature, patterned Nafion membrane were peeled off from the PDMS mold and keep Nafion membrane into deionized water container for  $\sim 12$  h.

### **2.3.3. Membrane electrode assembly (MEA) preparation**

A catalyst slurries for the anode and cathode catalyst layer were fabricated by mixing 40 wt.% Pt/C (Johnson Matthey), Nafion ionomer solution and 2-propanol (Sigma Aldrich). Multiscale and flat Nafion membranes (Dupont) were used after the pretreatment. They were boiled in 3 % hydrogen peroxide solution, and rinsed in D.I. water. After that, they were soaked in 0.5 M H<sub>2</sub>SO<sub>4</sub>, and washed again in D.I. water. Each procedure in the solutions was performed at 80 °C for 1 h, respectively. The prepared catalyst slurries were sprayed onto the anode and cathode parts of the Nafion membrane. The Pt loadings were equally 0.12 mg cm<sup>-2</sup> in the anodes and cathodes of the MEAs, respectively. The catalyst-coated membranes (CCMs) were dried at room temperature for 12 h, and sandwiched between the anode and cathode gas diffusion layers (GDLs, SGL 35 BC) without hot press process. The active geometric areas of the MEAs were 5.0 cm<sup>2</sup>.

### **2.3.4. Physical analysis of hierarchical multiscale structure**

Magnified optical images were seen using an optical microscope (Olympus IX70, Japan). Field emission-scanning electron microscopy (FE-SEM) was conducted using a SUPRA 55VP (Carl Zeiss) to measure morphology of the various sample used in this study. The Fourier Transform Infrared Spectroscopy (FTIR) spectra were obtained using Vertex 70 with FT-IR spectrometer (BRUCKER). IR radiation

was detected by a liquid-nitrogen-cooled mercury cadmium telluride detector. FT-IR data were obtained to monitor the degree of photopolymerization of PUA as a function of UV exposure time.

### **2.3.5. Electrochemical measurements of polymer electrolyte membrane fuel cell with multiscale Nafion membrane**

For the single cell performance test, fully humidified H<sub>2</sub> and O<sub>2</sub> (air) gas were supplied into the anode and cathode, respectively. The stoichiometric coefficient of H<sub>2</sub>/O<sub>2</sub> (air) was 2.0/9.5 (2.0), with total outlet pressure of ambient or 150 kPa. Single cell temperature was maintained at 80 °C according to DOE condition. Cyclic voltammogram (CV) was obtained in the potential range of 0.05 to 1.20 V vs. RHE at 100 mV/s to measure the electrochemical active surfaces area (ECSA) of the prepared cathode catalyst layers at room temperature (RT). Fully humidified H<sub>2</sub> and N<sub>2</sub> gas were injected to the anode and cathode, respectively. The anode flowing H<sub>2</sub> gas was used as reference and counter electrodes, and the cathode flowing N<sub>2</sub> gas served as a working electrode. Electrochemical impedance spectroscopy (EIS) (IM6, Zahner) of the single cells was measured at 0.6 V with an amplitude of 10 mV. The measurement was conducted in a frequency range from 0.1 Hz to 100 kHz. Other experimental conditions such as temperature and gas humidification were the same as single cell operation at 80 °C with H<sub>2</sub>/Air. The ZView program (Scribner Associates, Inc.) was utilized to fit the EIS data, and a

simple equivalent circuit was applied. The proton conductivity of Nafion membranes was measured using EIS (IM6, Zahner) fitted with a four probe with an amplitude of 10 mV over the frequency range from 0.1 Hz to 3.0 MHz. The impedance was measured at a controlled humidity and temperature (70 °C and 90 % RH). All electrochemical measurements in this study were reported versus a reversible hydrogen electrode (RHE). For the Nyquist plot, the real  $Z'$ -axis intercept was close to the ohmic resistance ( $R$ ) of a membrane. The proton conductivity ( $\sigma$ ) of membrane is calculated using the equation,  $\sigma = d/RS$ , where  $d$  is the distance between the reference and sensing electrodes, and  $S$  is the cross-section area of a membrane. (69) The accelerated durability test was conducted by using CV method. The CV test was repeated in the potential range of 0.05 to 1.20 V vs. RHE and 100 mV/s at RT for 5000 cycles with fully humidified  $H_2/N_2$  gas supplied to anode and cathode, respectively. (64) After ADT test, single cell performance and ECSA of samples were compared. Hydrogen crossover rate of membranes was measured by using linear sweep voltammetry in the range from 0 to 0.7 V. RHE and the moles of permeated hydrogen gas at 0.5 V vs. RHE was calculated by Nernst equation. (70)

## Chapter 3. Results and Discussion

---

### 3.1. Platinum Bimetallic Alloy Electrocatalyst synthesized by Al Pitting Corrosion method

#### 3.1.1. Physical characterization carbon supported Pt and Pt-M (Au, Pd) NPs

XRD results of carbon supported Pt and Pt-M (Au, Pd) NPs are presented in Figure 3-1. The synthesized NPs exhibited three main peaks of face centered cubic (FCC) Pt crystalline phase of (111), (200), and (220) at  $2\theta = 39.8^\circ$ ,  $46.2^\circ$  and  $67.5^\circ$ , respectively. In case of Pt<sub>3</sub>Au/C samples, they showed additional main peaks of FCC Au crystalline phase of (111), (200), and (220) appearing at  $2\theta = 38.2^\circ$ ,  $44.5^\circ$  and  $65.6^\circ$ , respectively, which means the NPs were not fully alloyed. (71, 72) Contrary to this, for Pd<sub>3</sub>Pd/C samples, they exhibited only three main peaks of FCC Pt crystalline phase and the angle of peaks moved to higher value slightly compared to pure Pt, which means the NPs were prepared as an alloyed structure. In addition, there were changes in peak intensities of samples after the heat treatment under various conditions. Specially, for the heat treated sample at 500 °C under H<sub>2</sub>/Ar atmosphere, the peaks became narrower and sharper than other conditions, which means due to the high temperature of the heat treatment, the NPs aggregated and size of them increased largely. (73) For the heat treated samples under H<sub>2</sub>/Ar and

CO atmosphere at 150 °C, however, the noticeable changes in main peaks were not detected. To examine the differences between Al pitting corrosion method and conventional sodium borohydride method, Pt bimetallic alloy NPs were synthesized by using sodium borohydride. Basically, there is a difference in reduction potential between them, (50, 74-76) it is expected that synthesized samples will show different particle size and alloying degrees. From the Figure 3-2, it is believed that due to fast reduction by sodium borohydride, the XRD peaks of samples moved to higher angle compared to samples prepared by Al pitting corrosion, which means higher alloying degree.

TEM images of carbon supported Pt and Pt-M (Au, Pd) NPs with various conditions are given in Figure. 3-3 ((a), (b) and (c) for Pt/C, Pt<sub>3</sub>Au/C and Pt<sub>3</sub>Pd/C ASP, (d), (e) and (f) for Pt/C, Pt<sub>3</sub>Au/C and Pt<sub>3</sub>Pd/C H<sub>2</sub>, (g), (h) and (i) for Pt/C, Pt<sub>3</sub>Au/C and Pt<sub>3</sub>Pd/C 500, (j), (k) and (l) for Pt/C, Pt<sub>3</sub>Au/C and Pt<sub>3</sub>Pd/C CO) The average particle sizes and distribution of samples are expressed as insets of Figure 3-3. Particle size changes of samples were detected after the post heat treatment. Among these, after the heat treatment at 500 °C, particle size changes were significant for every sample. To figure out the distribution of Pt, Au and Pd, EDS mapping analysis of samples was conducted (Figure 3-4. (a) to (e)). From the mapping images, we concluded that the synthesized Pt and Pt-M (Au, Pd) NPs are well distributed on carbon black, which means Al foil is a good candidate as a reducing agent for synthesizing Pt and Pt bimetallic NPs. In addition, TEM images



of samples prepared by sodium borohydride method are given Figure 3-5 ((a), (b) and (c) for Pt/C, Pt<sub>3</sub>Au/C and Pt<sub>3</sub>Pd/C ASP, (d), (e) and (f) for Pt/C, Pt<sub>3</sub>Au/C and Pt<sub>3</sub>Pd/C H<sub>2</sub>, (g), (h) and (i) for Pt/C, Pt<sub>3</sub>Au/C and Pt<sub>3</sub>Pd/C 500, (j), (k) and (l) for Pt/C, Pt<sub>3</sub>Au/C and Pt<sub>3</sub>Pd/C CO). Comparing the average particle size of samples, it is concluded that samples with sodium borohydride method showed much smaller particle size due to the fast reduction reaction. Besides, same as before, particle size changes of samples were detected after the post heat treatment. Among these, after the heat treatment at 500 °C, particle size changes were significant for every sample.

The surface atomic composition of Pt was calculated from the XPS intensity of Pt 4f<sub>7/2</sub>, Au 4f<sub>7/2</sub> and Pd 3d<sub>5/2</sub> with a correction of the photoelectron cross section and was compared to the bulk composition of samples. The surface and bulk composition of samples prepared by Al pitting corrosion calculated from XPS data are presented in Figure 3-6 and 3-7. The bulk Pt fractions of Pt of Pt<sub>3</sub>Au/C and Pt<sub>3</sub>Pd/C samples are 75.7 % and 90.5 %, confirmed by ICP-AES. Compared these values each other, it is concluded that in case of Pt<sub>3</sub>Au/C samples, surface Pt atomic composition of samples was higher than bulk composition except Pt<sub>3</sub>Au/C 500 sample, which is the result of the difference in surface energies of Pt and Au, and in case of Pt<sub>3</sub>Pd/C samples, however, those values and bulk composition were same, which means no changes in surface atomic composition by the heat treatment. Samples prepared by sodium borohydride method have shown different bulk and surface compositions. The bulk Pt fractions of Pt of Pt<sub>3</sub>Au/C and Pt<sub>3</sub>Pd/C samples

are 71.4 % and 79.1 %, confirmed by ICP-AES. Compared these values each other, however, it is shown that the effect of the heat treatment is similar and the trends of surface Pt composition was identical compared to that of samples of Al pitting corrosion before mentioned.

### **3.1.2. Electrochemical characterizations of carbon supported Pt and Pt-M (Au, Pd) NPs**

In Figure 3-8. (a), (c) and (e), the results of the CV was expressed. All CV measurement were repeated to obtain stable CV curves and as a result, there are no any evidences of impurities in CV. Every sample exhibited typical  $H_{upd}$  region in the range from 0.05 to 0.4 V vs. RHE and Pt oxide formation and reduction peak near 0.8 V vs. RHE. Among these, ASP samples did not exhibit  $H_{upd}$  regions because during the preparation step, samples were treated in acid solution for 24 h to get rid of Al metal residue, inducing the surface oxidation of NPs. From  $H_{upd}$  region, we calculated electrochemically active surface area (ECSA) with a charge density of  $210 \mu C/cm^2$  for hydrogen adsorption area on Pt. According to calculated values, the ECSAs were changed after the each heat treatment in various conditions, resulting in the particle size changes and surface fraction of Pt in NPs. In case of Pt/C samples, after the every additional heat treatment, the ECSA decreased gradually due to the enlarged Pt NPs. For  $Pt_3Au/C$  samples, as the surface atomic

fraction of Pt and the size of NPs change, the ECSA changes to smaller or larger value. When it was heat treated at 500 °C under H<sub>2</sub>/Ar atmosphere, the surface fraction of Au increased up to 34 % and the NPs aggregated significantly, resulting in the decrease of ECSA to large degrees. Contrary to this, when it was treated under CO atmosphere, the surface fraction of Pt increased due to the segregation of Pt induced by interaction between CO and Pt and the ECSA increased in turn. For Pt<sub>3</sub>Pd/C samples, the surface fraction of Pt did not changed by the heat treatment largely. Therefore, it can be interpreted that the heat treatment affect the atomic ordering and electronic structure of Pt<sub>3</sub>Pd/C samples, not surface atomic fractions of NPs. This will be analyzed further by electrochemical measurement part. The rotating disk electrode (RDE) technique was used to conduct assessment of the activity for oxygen reduction reaction in 0.1 M HClO<sub>4</sub> solution in Figure 3-8. (b), (d) and (f). The ORR polarization curve measurements were initiated in the positive direction from 0.05 V to 1.05 V vs RHE. It is manifest that half-wave potentials increased in following order: Pt/C H<sub>2</sub> > Pt/C CO > Pt/C 500, Pt<sub>3</sub>Au/C CO > Pt<sub>3</sub>Au/C H<sub>2</sub> > Pt<sub>3</sub>Au/C 500, Pt<sub>3</sub>Pd/C CO ≥ Pt<sub>3</sub>Pd/C H<sub>2</sub> > Pt<sub>3</sub>Pd/C 500 The Pt mass normalized kinetic current density of Pt<sub>3</sub>Au/C CO at 0.9 V vs. RHE was slightly higher than that of commercial Pt catalyst (Figure 3-9). Comparing Pt bimetallic alloy NPs prepared by Al pitting corrosion method to those of sodium borohydride method, it is manifest that the surface structure and chemical state are difference due to the difference between synthesis processes. In case of ASP samples, at first, ASP

samples prepared by pitting corrosion method did not exhibit  $H_{upd}$  area due to surface oxidation by the additional acid treatment. However, ASP samples prepared by sodium borohydride method showed clear  $H_{upd}$  area and because of this, the effect of the heat treatment is different from those of samples prepared by Al pitting corrosion method. For Pt/C and Pt<sub>3</sub>Pd/C prepared by sodium borohydride method, among the additional heat treatments, the heat treatment under hydrogen atmosphere at 150°C is favorable for better ORR activity. However, for Pt<sub>3</sub>Au/C samples, every additional heat treatment did not give positive effects on their ORR activity (Figure 3-10). (Half-wave potentials increased in following order: Pt/C H<sub>2</sub> > Pt/C ASP > Pt/C CO > Pt/C 500, Pt<sub>3</sub>Au/C ASP > Pt<sub>3</sub>Au/C H<sub>2</sub> > Pt<sub>3</sub>Au/C CO > Pt<sub>3</sub>Au/C 500, Pt<sub>3</sub>Pd/C H<sub>2</sub> > Pt<sub>3</sub>Pd/C ASP > Pt<sub>3</sub>Pd/C CO > Pt<sub>3</sub>Pd/C 500) The Pt mass and area normalized kinetic current density at 0.9 V and ECSA were expressed in Figure 3-11. Reasons of these results will be explained in following parts.

The electronic structure and surface composition of carbon supported Pt and Pt-M (Au, Pd) NPs were analyzed by XPS measurement. The core-level Pt 4f spectra of every sample exhibited a doublet signal for Pt 4f<sub>5/2</sub> and 4f<sub>7/2</sub>, respectively and were deconvoluted into Pt<sup>0</sup>, Pt<sup>2+</sup> and Pt<sup>4+</sup>. The XPS deconvolution data and spectra are presented in Table 3-1 and 3-2. When compared with the binding energy 70.9 eV of pure Pt, a shift of Pt<sup>0</sup> to a higher binding energy was detected for every sample, which can be explained by oxophilicity of NPs compared to bulk structure and especially for Pt<sub>3</sub>Pd samples, electron transfer from Pd to Pt resulted from alloying

can be the reason of this. (77, 78) It is also interpreted that the shift of binding energy to higher value of induces downshift of d-band center of Pt, which is the important descriptor to explain ORR activity of electrocatalyst. (79) In addition, after the heat treatment, the ratio of Pt<sup>0</sup> was changed. In case of the heat treatments under H<sub>2</sub> atmosphere, the Pt<sup>0</sup> percentage of every sample increased to some degrees. However, in case of the heat treatment under CO atmosphere, the Pt<sup>0</sup> percentage of every sample decreased. From the deconvolution data for the Au 4f core level region, which can be assigned to the formation of Au metal. Peaks of metallic Au (near 84.5 eV for 4f<sub>7/2</sub> compared to 83.8 eV for pure Au) were easily detected, indicating that Au metal was dominant on their surface. In addition, the XPS spectra of Pd 3d core level region were presented. Due to the overlap of Pt 4d region, it is impossible to deconvolute the Pt peaks. Comparing the binding energies of Pd 3d<sub>5/2</sub> peaks of samples, it is proved that the peaks (near 336.3 eV) moved to higher values than pure Pd (334.9 eV), which means the electron transfer from Pd to Pt induced by alloying. For Pt bimetallic alloy NPs prepared by sodium borohydride method, as mentioned before, a shift of Pt<sup>0</sup> to a higher binding energy was detected for every sample for Pt<sub>3</sub>Pd samples due to the electron transfer from Pd to Pt resulted from alloying. In addition, after the heat treatments under H<sub>2</sub> atmosphere, the Pt<sup>0</sup> percentage of every sample increased to some degrees and after the heat treatment under CO atmosphere, the Pt<sup>0</sup> percentage of every sample decreased.

To analyze the structural changes and elucidate the enhancement of ORR activity after the heat treatment, CO oxidation method was conducted by using CV technique in Figure 3-12 (a), (c) and (e). Before the measurement, CO molecules was adsorbed on Pt and Pt-M (Au, Pd) NPs at potential of 0.05 V vs. RHE for 15 min and electrolyte was purged with Ar gas for 30 min. Then, adsorbed CO molecules were oxidized electrochemically via potentials sweep from 0.05 V to 1.05 V vs. RHE. Typical adsorbed CO oxidation curve has two distinct peaks at near 0.7 V and 0.85 V vs. RHE, which refer to Pt (111) and Pt (100) facets. (80) For every sample, after the heat treatment at 500 °C, particle size changes were significantly increased. Due to this, the adsorbed CO oxidation curve changed and the oxidation peak area was decreased largely. In case of Pt<sub>3</sub>Au/C samples, the second peak was diminished after the heat treatment under CO atmosphere, which means the fraction of Pt (111) on its surface increased, not d-band modification (Figure 3-13) and due to this, the ORR activity was also increased in turn (81). In addition, from XPS quantitative analysis of surface Pt fraction (Figure 3-6), after the heat treatment under CO atmosphere, the surface Pt fraction increased to some degrees. It can be also the reason of enhanced ORR activity. For Pt<sub>3</sub>Pd/C samples, the fraction of Pt facets was not changed considerably. However, the onset potential of adsorbed CO oxidation moved to higher potential after the heat treatment under CO atmosphere, which means the oxophilicity of Pt<sub>3</sub>Pd/C CO was decreased and because of this, the ORR activity was increased. In addition, from XPS

deconvolution data mentioned above, the binding energy of  $\text{Pt}^0$  after the heat treatment under CO atmosphere shifted to higher value compared to other samples, which means downshift of d-band center. (Figure 3-13) It is regarded as the decrease in binding energy for oxygen species such as O, OH and oxophilicity of Pt. Therefore, these results are in good agreement with the ORR activity trends of samples. Additionally,  $\text{N}_2\text{O}$  reduction analysis was conducted to obtain information about electronic structure of samples indirectly (Figure 3-12 (b), (d) and (f)). As the adsorption and reduction of  $\text{N}_2\text{O}$  can occur only at free sites, the reduction rate will be maximized when the amount of adsorbed ions becomes minimum value, indicating the potential of zero total charge (PZTC). It is believed that the value of PZTC has a relationship with work function, surface structure and specific adsorption properties of electrocatalyst, the ORR activity can be analyzed in terms of PZTC. When it comes to the relationship between ORR activity and PZTC, as the PZTC value increases to higher potential, the binding energy with oxygen species decreases and ORR activity also increases. In other words, the increase in PZTC value means that it becomes hard to oxidize the surface of electrocatalyst and it can be interpreted that the binding energy to oxygen species decreases on Pt and it facilitates the kinetics of ORR consequently. For  $\text{Pt}_3\text{Au}/\text{C}$  samples, the potentials at maximum reduction current is almost same, which means the electronic structure of Pt of samples was not changed. For  $\text{Pt}_3\text{Pd}/\text{C}$  samples, however,  $\text{Pt}_3\text{Pd}/\text{C}$  CO has much higher potential value than  $\text{Pt}_3\text{Pd}/\text{C}$   $\text{H}_2$  and  $\text{Pt}_3\text{Pd}/\text{C}$  500, which proves that

because of the heat treatment under CO atmosphere, the electronic structure of Pt<sub>3</sub>Pd/C CO was changed desirably and resulted in higher ORR activity. To further analyze the surface structure of samples, methanol oxidation reaction (MOR) test was carried out via CV method in Figure 3-14. After the heat treatment under CO atmosphere, the onset potential for MOR moved to negative values, which means the surface structure of samples were modified for higher MOR activity. For Pt<sub>3</sub>Au/C samples, after the heat treatment under CO atmosphere, Pt (100) facet decreased and Pt (111) became dominant facet. From the researches about MOR, the onset potential for bulk oxidation increases in the order of Pt (111) < Pt (110) < Pt (100). (82-84) This is in accordance with adsorbed CO oxidation analysis. For Pt<sub>3</sub>Pd/C samples, although Pt<sub>3</sub>Pd/C CO exhibited higher MOR activity, the difference in onset potential was not that great, which means the heat treatment did not changed surface structure of Pt<sub>3</sub>Pd/C samples. Instead, from the heat treatment under CO atmosphere, the downshift of d-band center of Pt<sub>3</sub>Pd/C occurred, due to this, Pt<sub>3</sub>Pd/C CO showed better MOR activity than the other samples.

In case of samples prepared by sodium borohydride method, the surface structures of samples are very different from those of samples prepared by Al pitting corrosion method. (Figure 3-15) Among the samples, Pt<sub>3</sub>Au/C samples displayed very different surface structures, showing only one CO oxidation peak and no peak separation after the heat treatment. It is regarded as the formation of Pt-Au alloy structure with high alloying degree. In addition, from the CO oxidation data on



polycrystalline Pt, it is commonly believed that the peak at 0.85 V vs. RHE refers to the existence Pt (100). Hence, after the heat treatment, Pt (100) facet become dominant and due to this, ORR activity of Pt<sub>3</sub>Au/C samples decreased. In addition, according to the conditions of the heat treatment, surface composition of Pt<sub>3</sub>Au/C samples changed. After the heat treatment under H<sub>2</sub> atmosphere, the ECSAs decreased and onset potential of CO oxidation moved to higher potentials, which means decrease in surface Pt fraction of samples. Contrary to this, after the heat treatment under CO atmosphere, the ECSAs increased and onset potential of CO oxidation moved to smaller potentials, which means increase in surface Pt fraction. For Pt<sub>3</sub>Pd/C samples, however, after the heat treatment under H<sub>2</sub> atmosphere at 150°C exhibited the highest ORR activity due to increased alloying degree. The increased alloying degree triggered d-band modification and because of this, the onset potential of CO oxidation become larger than before. This is the same trend with ORR activity. In addition, it is concluded that Pt<sub>3</sub>Pd/C samples are less sensitive to the heat treatment under H<sub>2</sub> and CO atmosphere compared to Pt<sub>3</sub>Au/C samples due to the difference in surface energy among Pt, Au and Pd.

Lastly, the single cell performance test was conducted with synthesized Pt bimetallic alloy NPs (Pt/C H<sub>2</sub>, Pt<sub>3</sub>Au/C CO and Pt<sub>3</sub>Pd/C CO) prepared by Al pitting corrosion under the condition that fully humidified H<sub>2</sub> and O<sub>2</sub> gas were supplied into the anode and cathode, respectively. It is shown that MEA with the synthesized Pt bimetallic alloy NPs exhibited comparable performance without any

modifications of electrode structure and system. In addition, they showed higher Pt mass normalized maximum power density in case of Pt<sub>3</sub>Au/C CO, which is the same trend with above mentioned ORR data. (Figure 3-16)

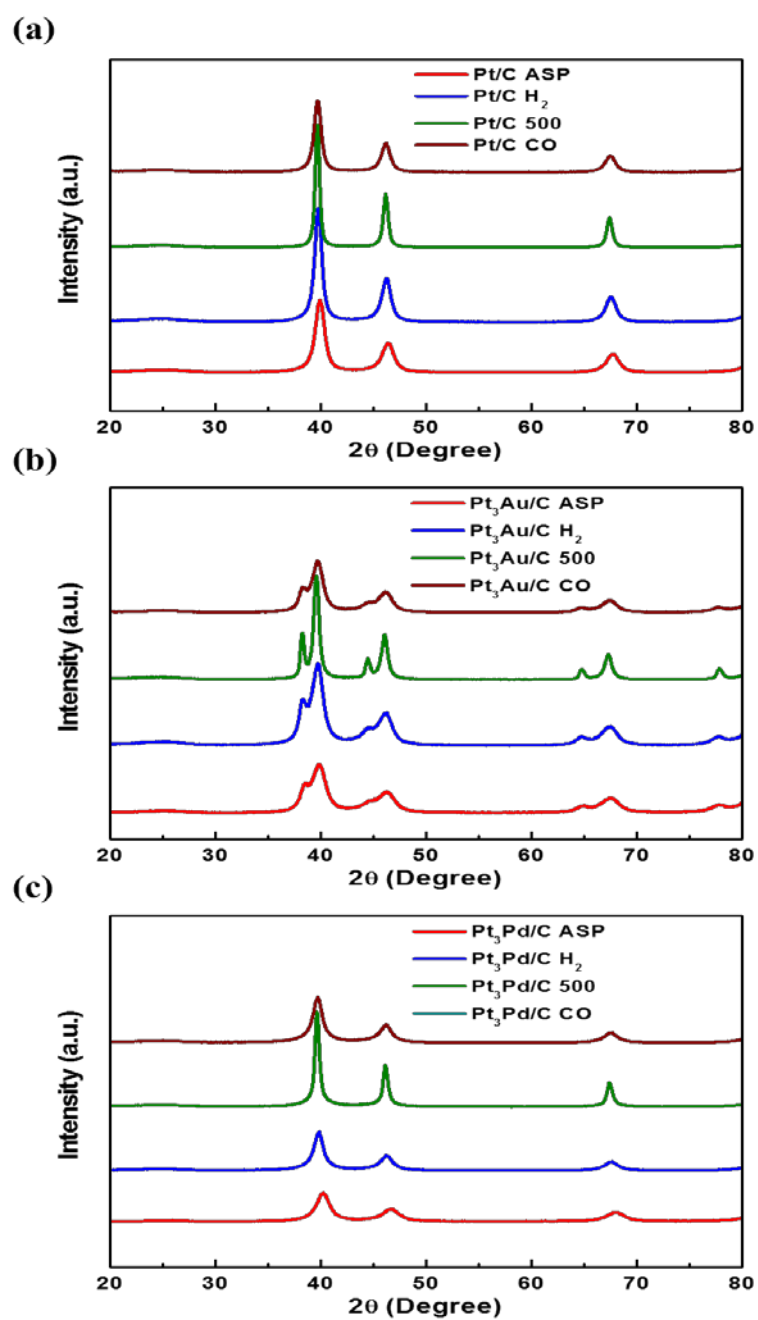


**Figure 3-1.** XRD spectra of carbon supported Pt and Pt-M (Au, Pd) NPs prepared by Al pitting corrosion method.

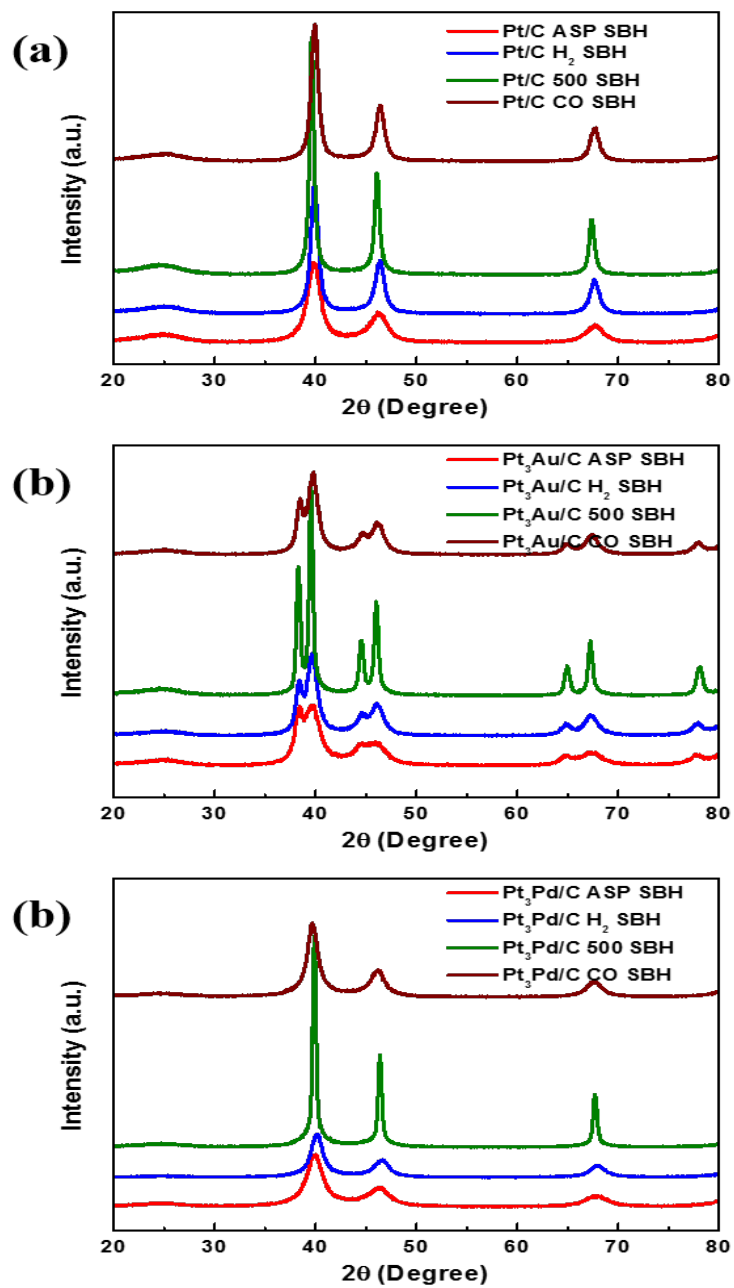


**Figure 3-2.** XRD spectra of carbon supported Pt and Pt-M (Au, Pd) NPs prepared by sodium borohydride method.

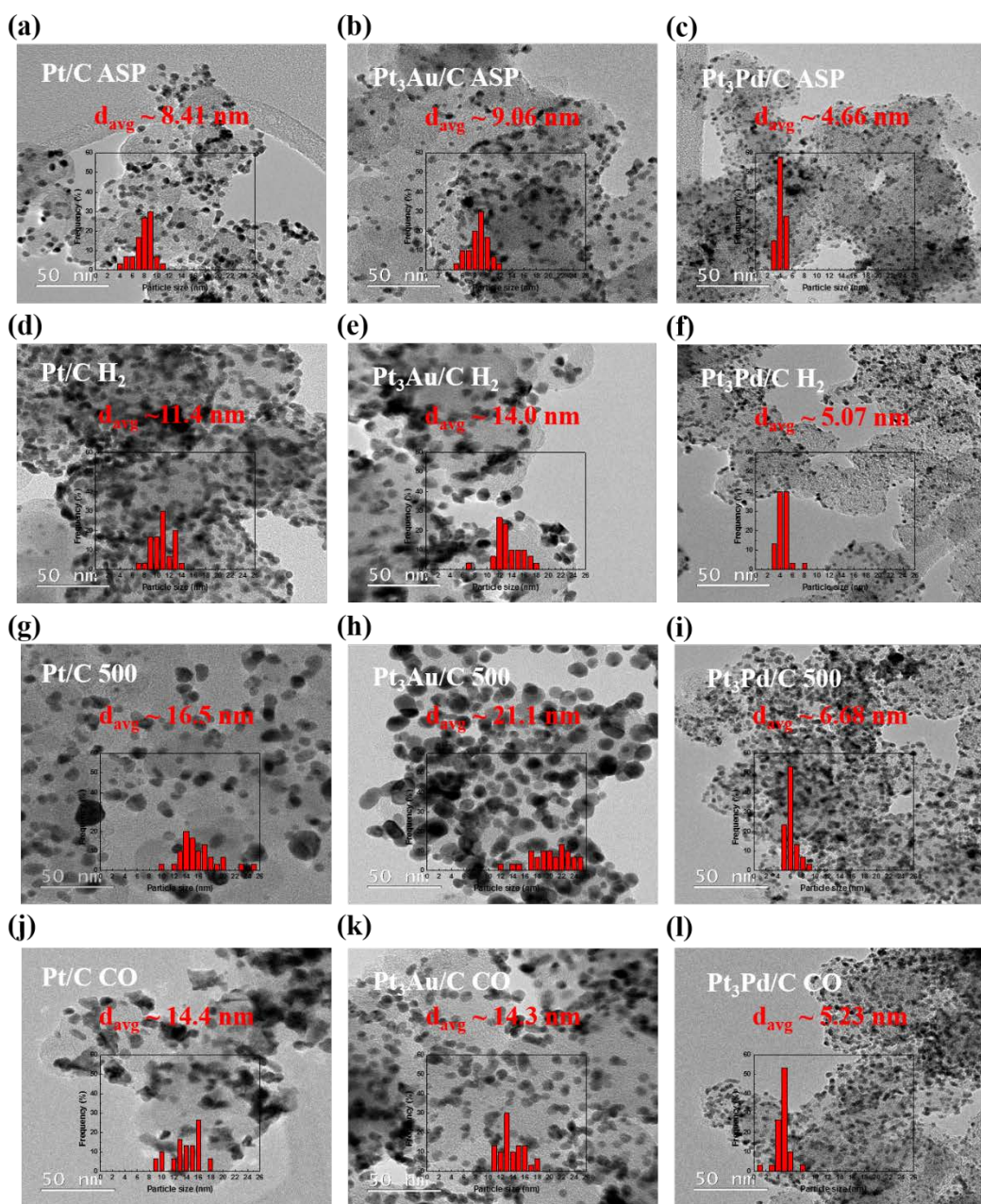


**Figure 3-3.** TEM images of carbon supported Pt and Pt-M (Au, Pd) NPs prepared by Al pitting corrosion method with various conditions and their particle size distributions.

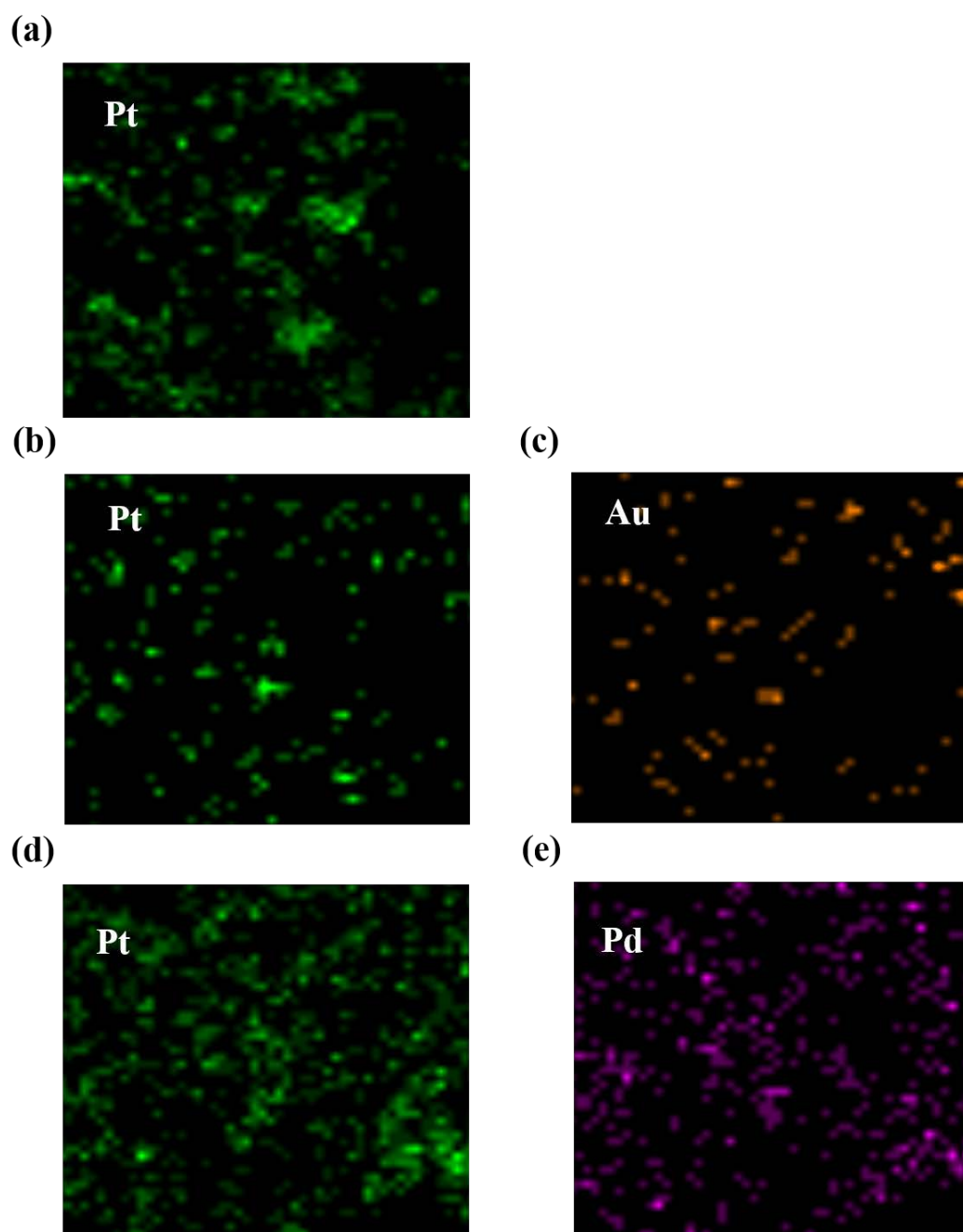


**Figure 3-4.** EDS mapping analysis of carbon supported Pt and Pt-M (Au, Pd) NPs.



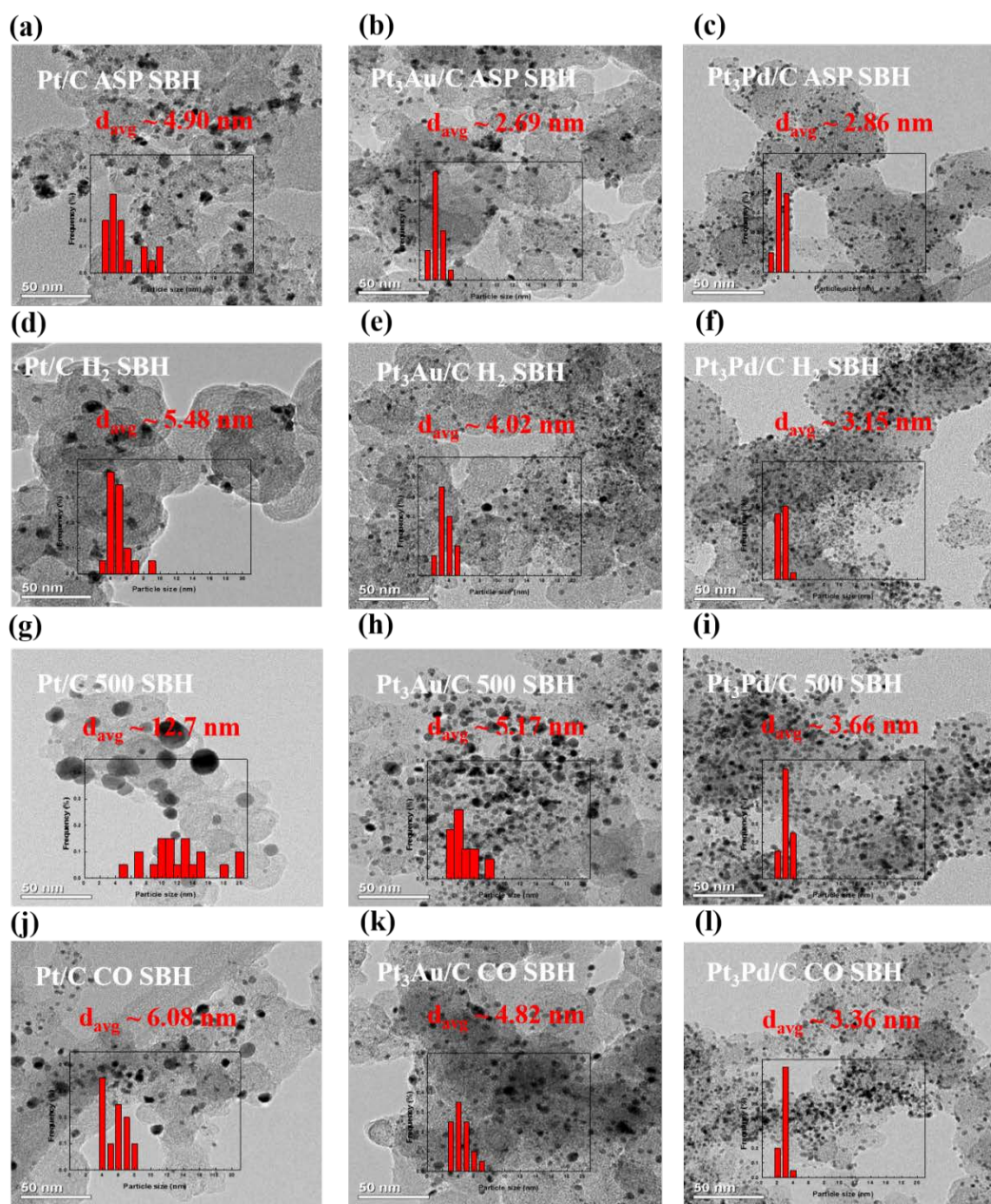


**Figure 3-5.** TEM images of carbon supported Pt and Pt-M (Au, Pd) NPs prepared by sodium borohydride method with various conditions and their particle size distributions.

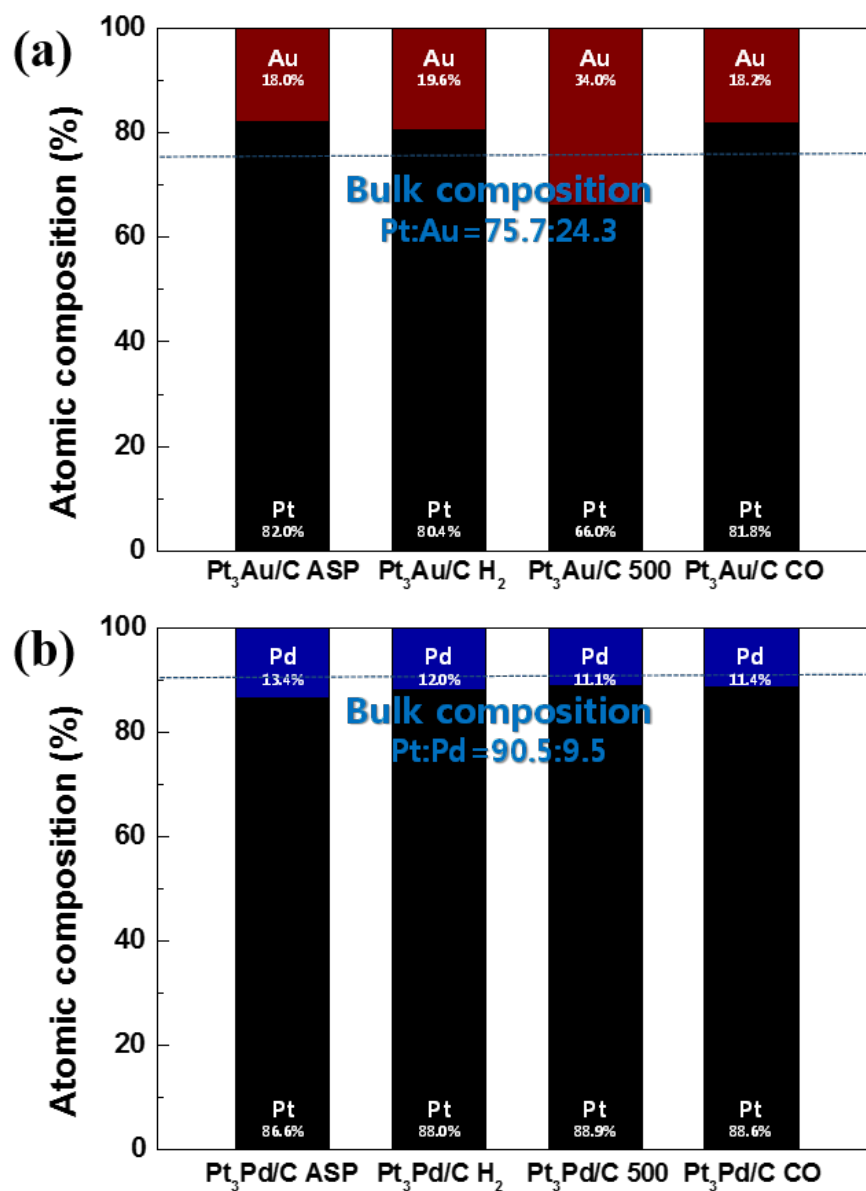


**Figure 3-6.** Comparison of bulk and surface composition of Pt bimetallic alloy NPs prepared by Al pitting corrosion method.



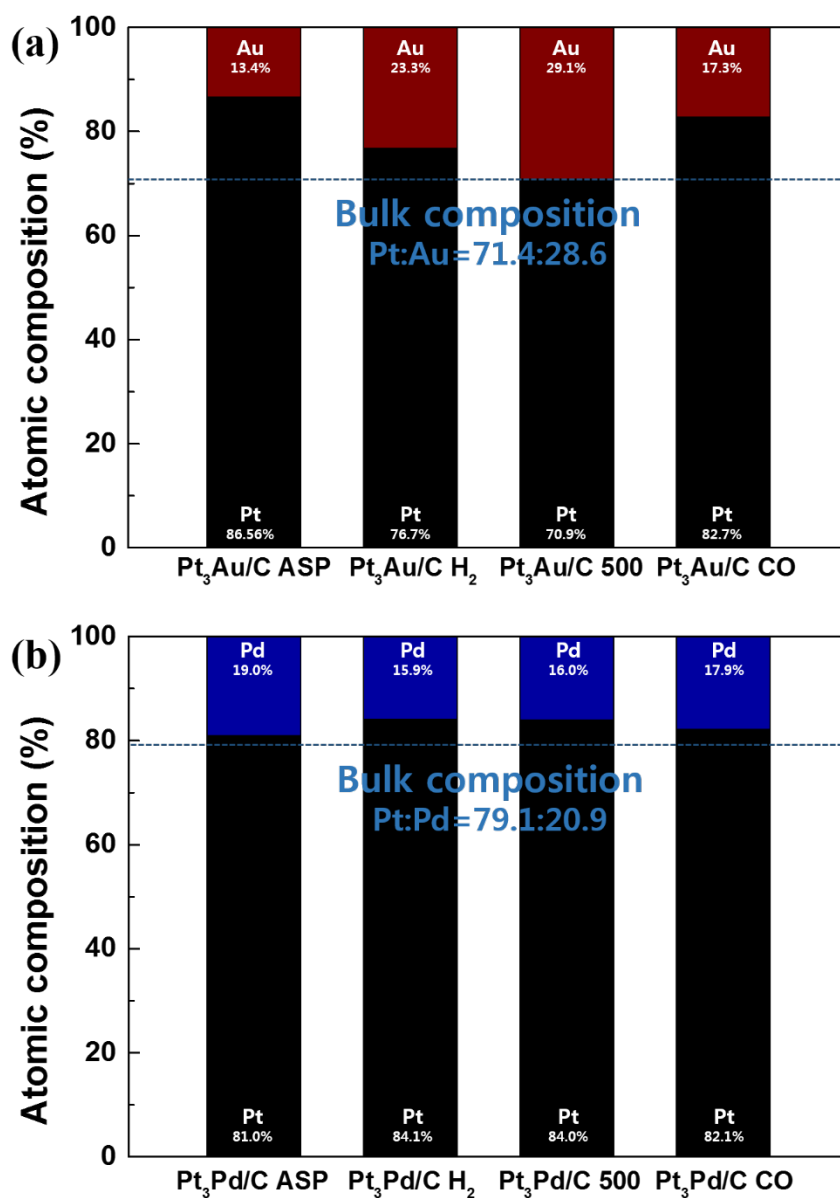


**Figure 3-7.** Comparison bulk and surface composition of Pt bimetallic alloy NPs prepared by sodium borohydride method.

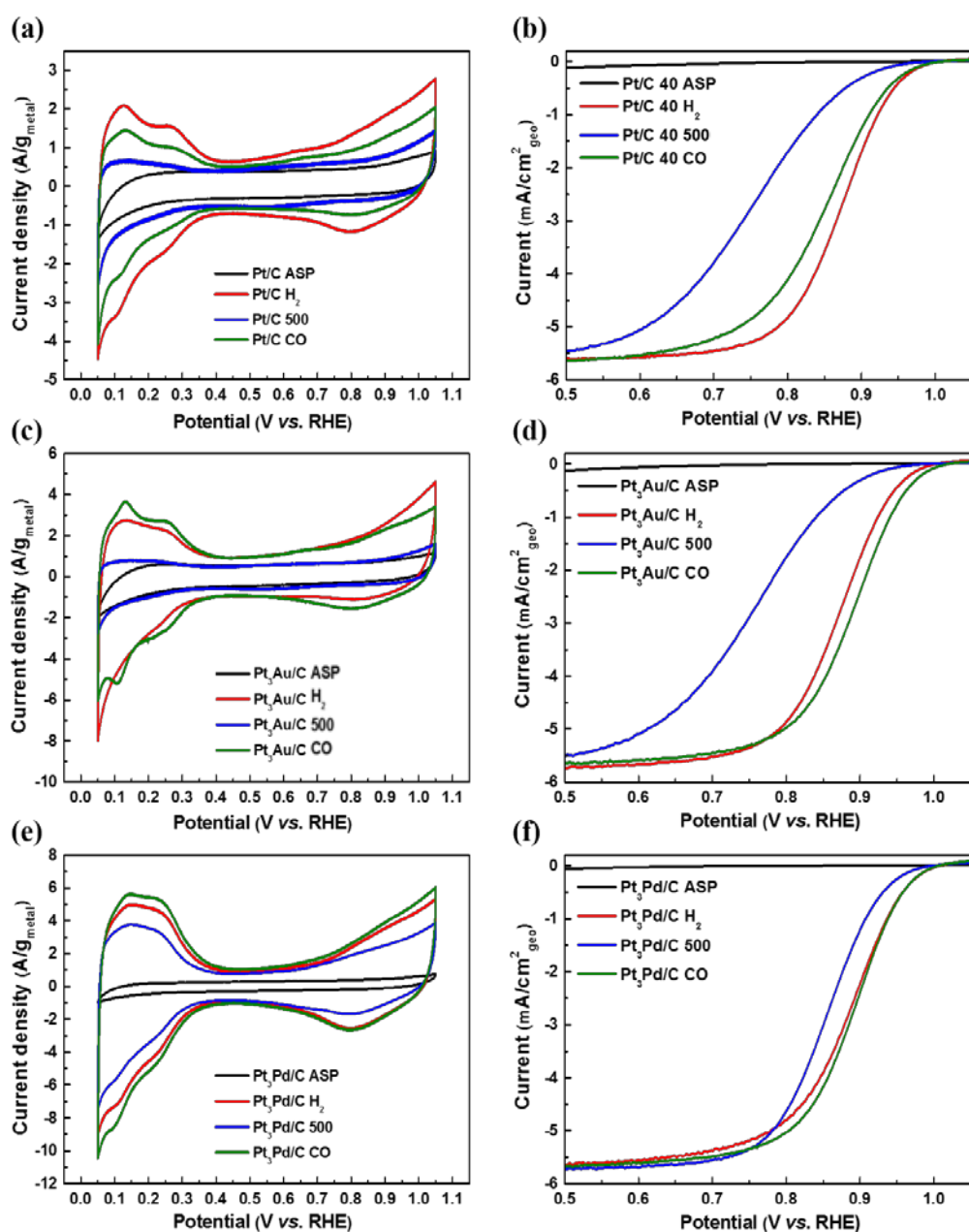


**Figure 3-8.** Cyclic voltammogram ((a), (c), (e)) and ORR polarization curve ((b), (d), (f)) of carbon supported Pt and Pt-M (Au, Pd) NPs prepared by Al pitting corrosion method with various conditions.

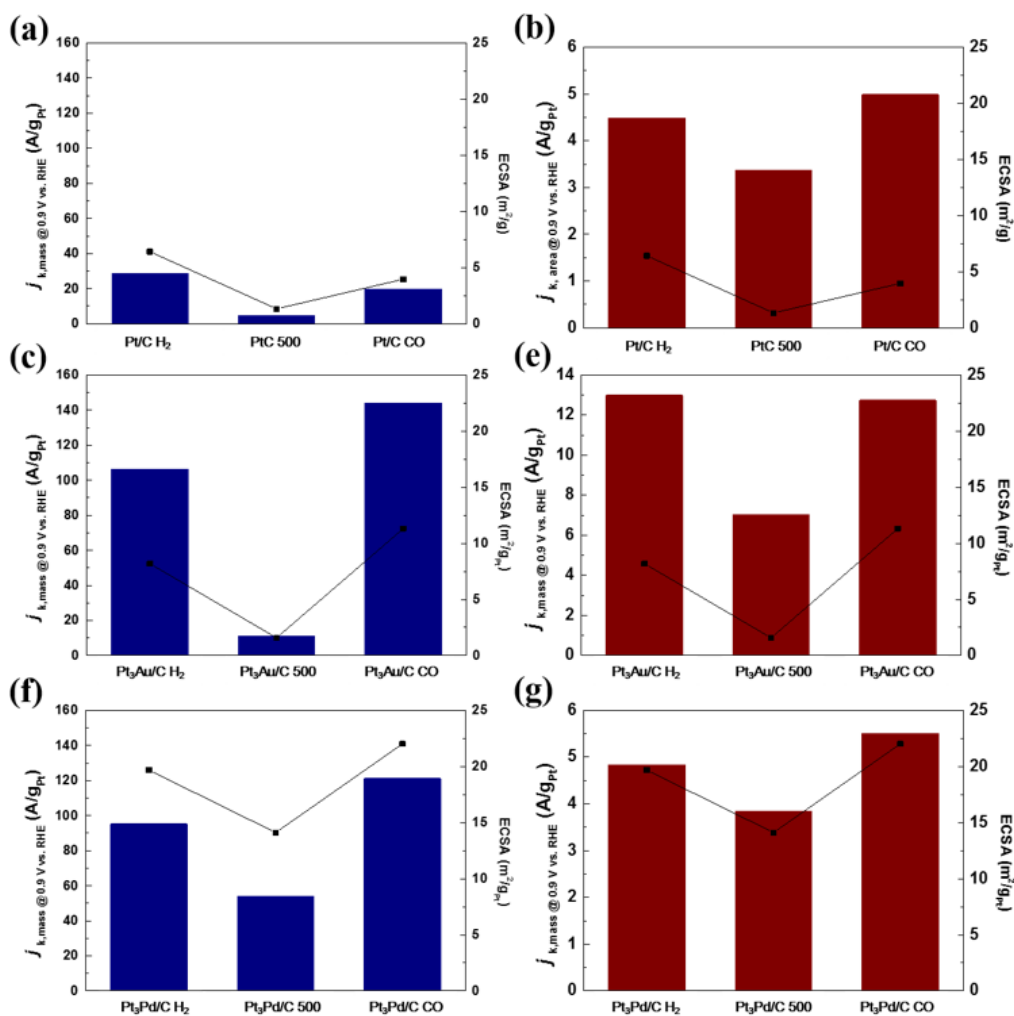


**Figure 3-9.** Relationship between ECSA and mass and specific activity at 0.9 V vs. RHE of carbon supported Pt and Pt-M (Au, Pd) NPs synthesized via Al pitting corrosion with various conditions.

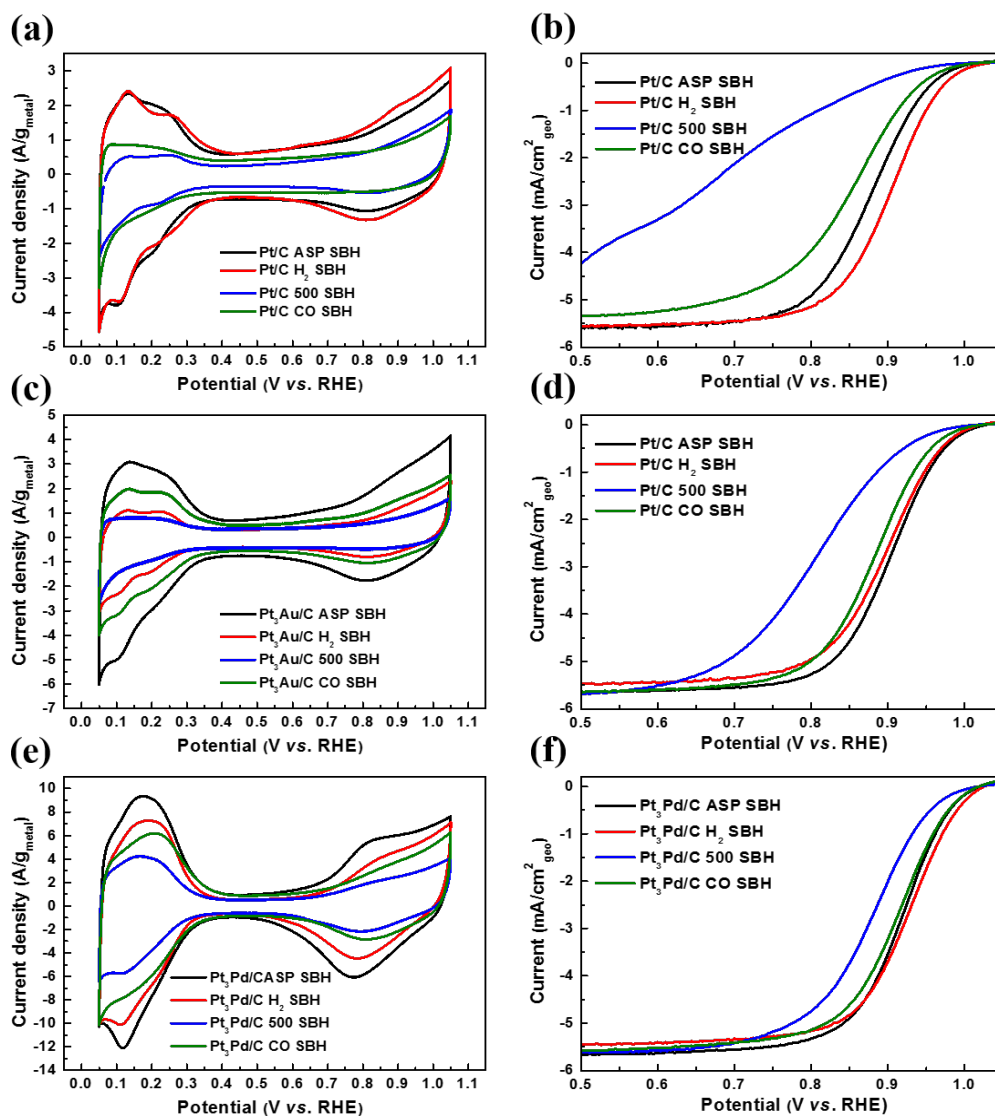


**Figure 3-10.** Cyclic voltammogram ((a), (c), (e)) and ORR polarization curve ((b), (d), (f)) of carbon supported Pt and Pt-M (Au, Pd) NPs prepared by sodium borohydride method with various conditions.

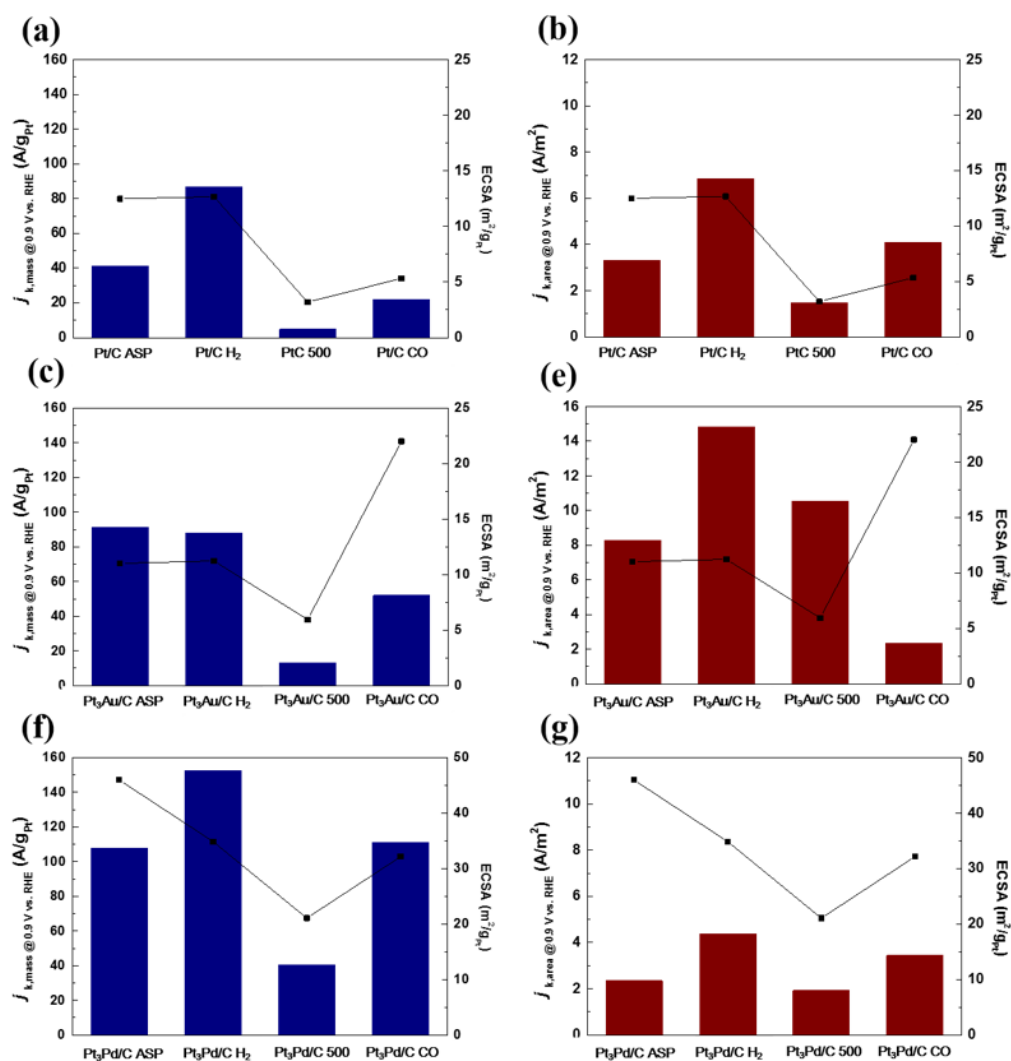


**Figure 3-11.** Relationship between ECSA and mass and specific activity at 0.9 V vs. RHE of carbon supported Pt and Pt-M (Au, Pd) NPs synthesized via sodium borohydride method with various conditions.

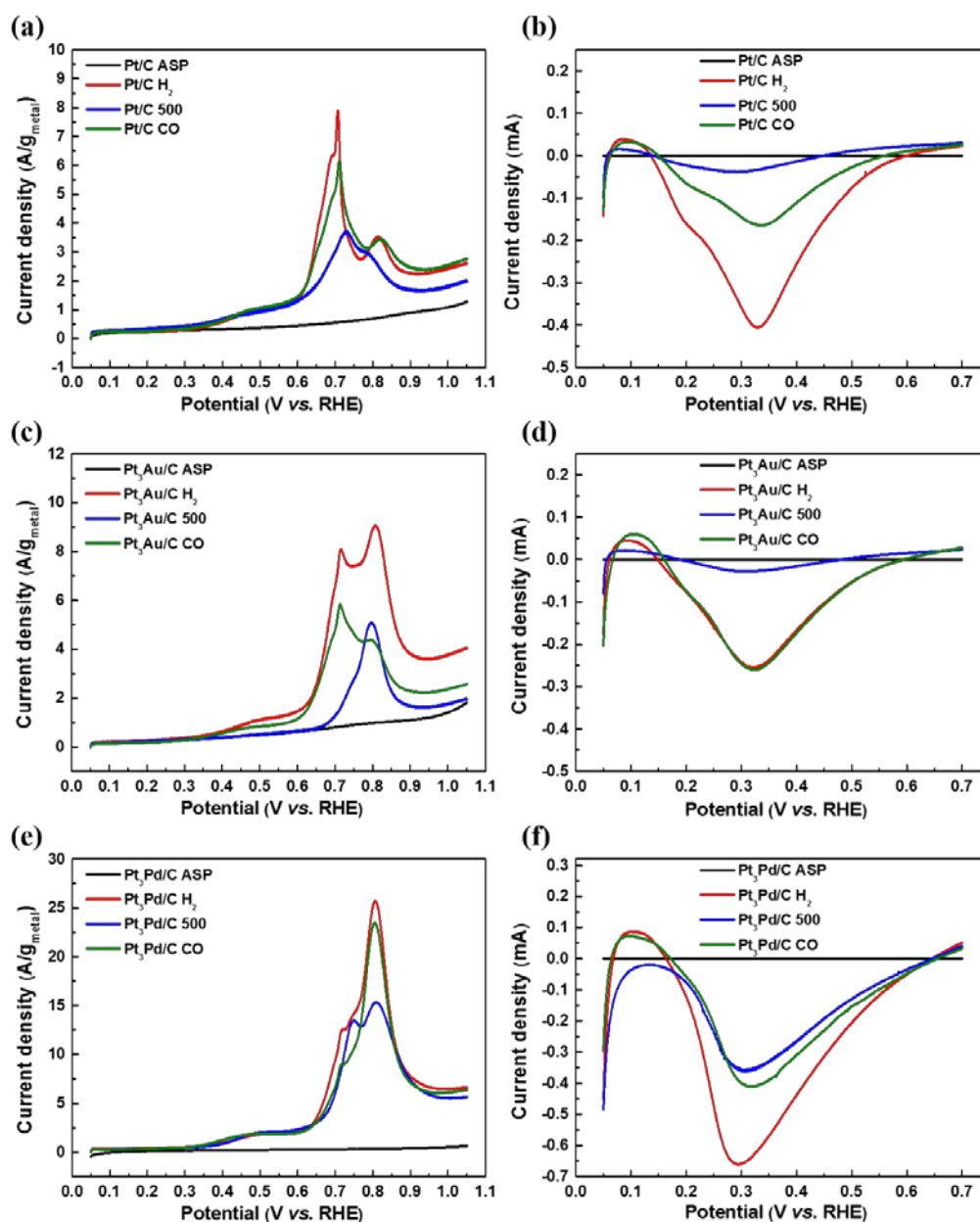


**Figure 3-12.** CO stripping voltammogram ((a), (c), (e)) and  $N_2O$  reduction curve ((b), (d), (f)) of carbon supported Pt and Pt-M (Au, Pd) NPs prepared by Al pitting corrosion method with various conditions.

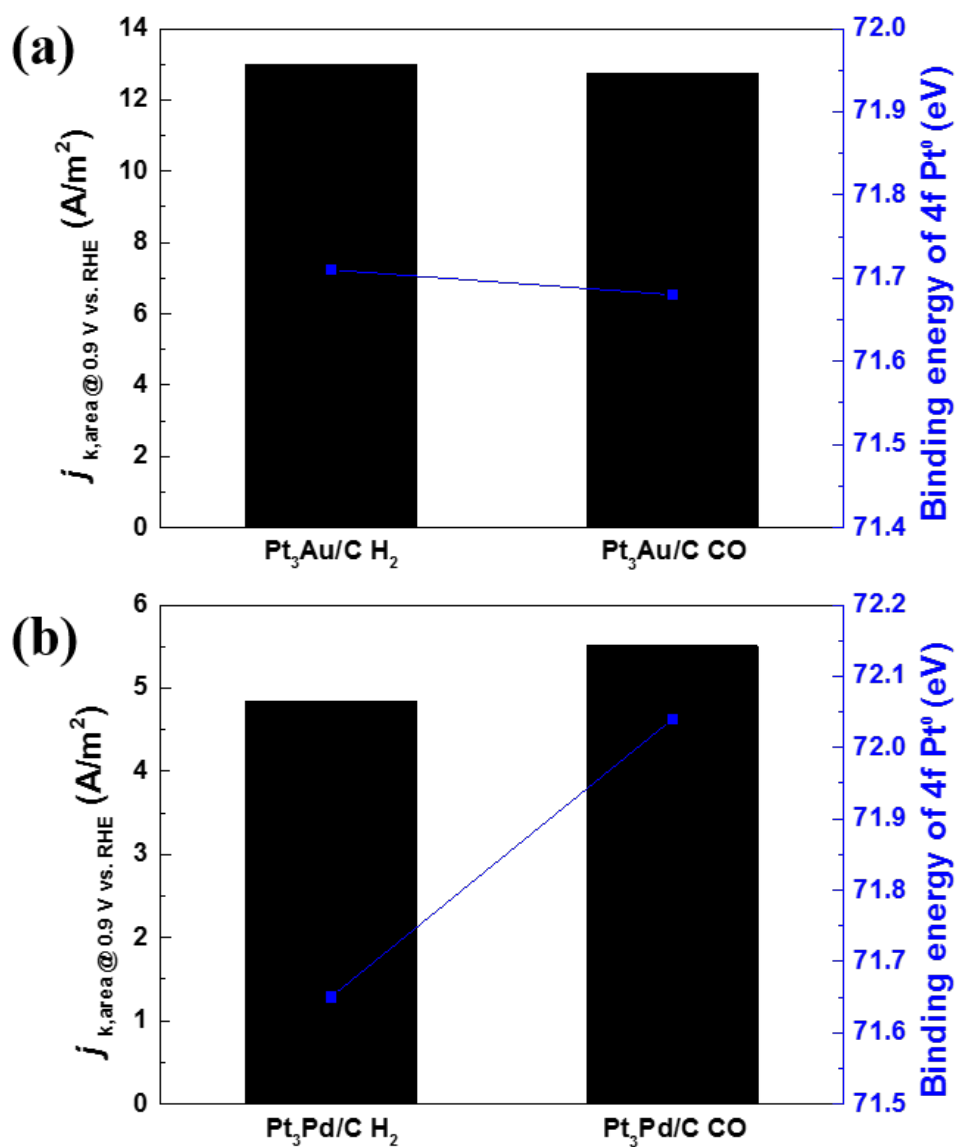


**Figure 3-13.** Comparison area normalized ORR activity at 0.9 V vs. RHE and binding energies of 4f Pt<sup>0</sup> of Pt bimetallic alloy NPs prepared by Al pitting corrosion method.

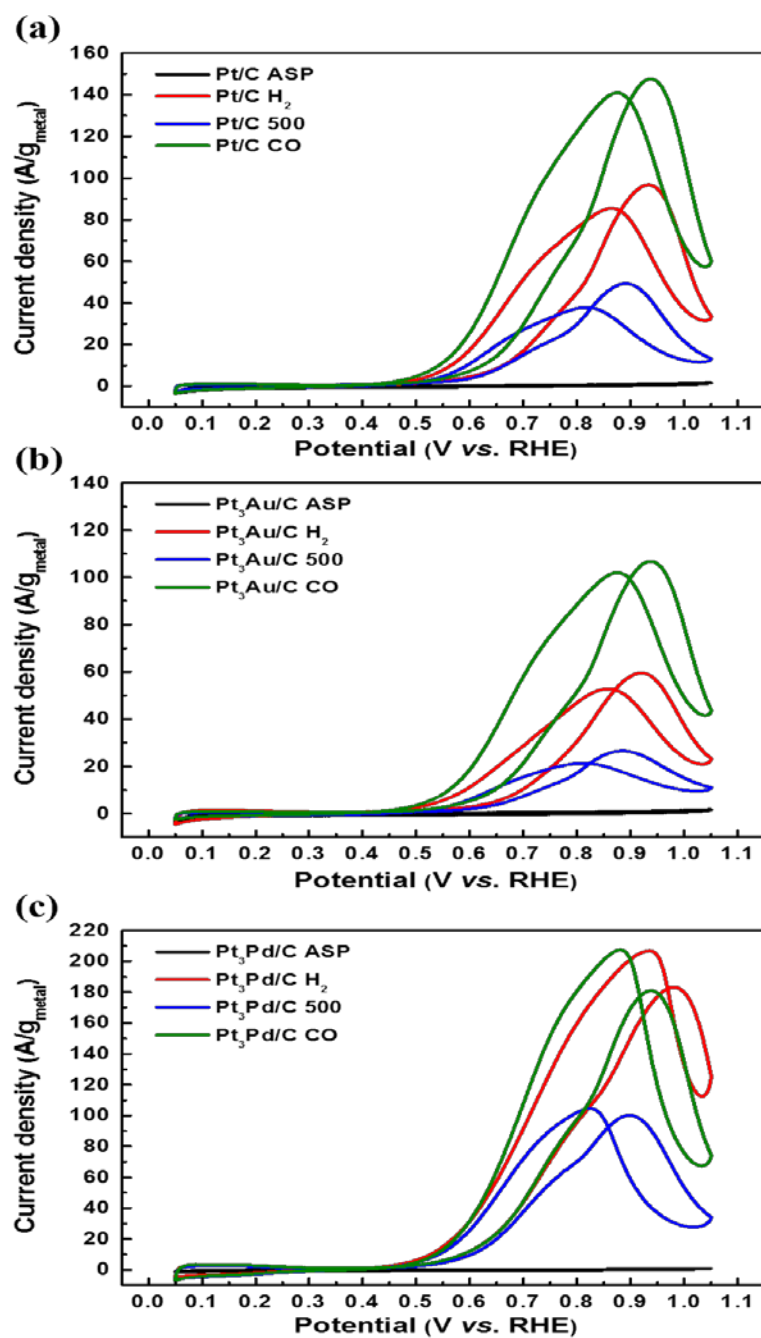


**Figure 3-14.** MOR data of carbon supported Pt and Pt-M (Au, Pd) NPs prepared by Al pitting corrosion method with various conditions.



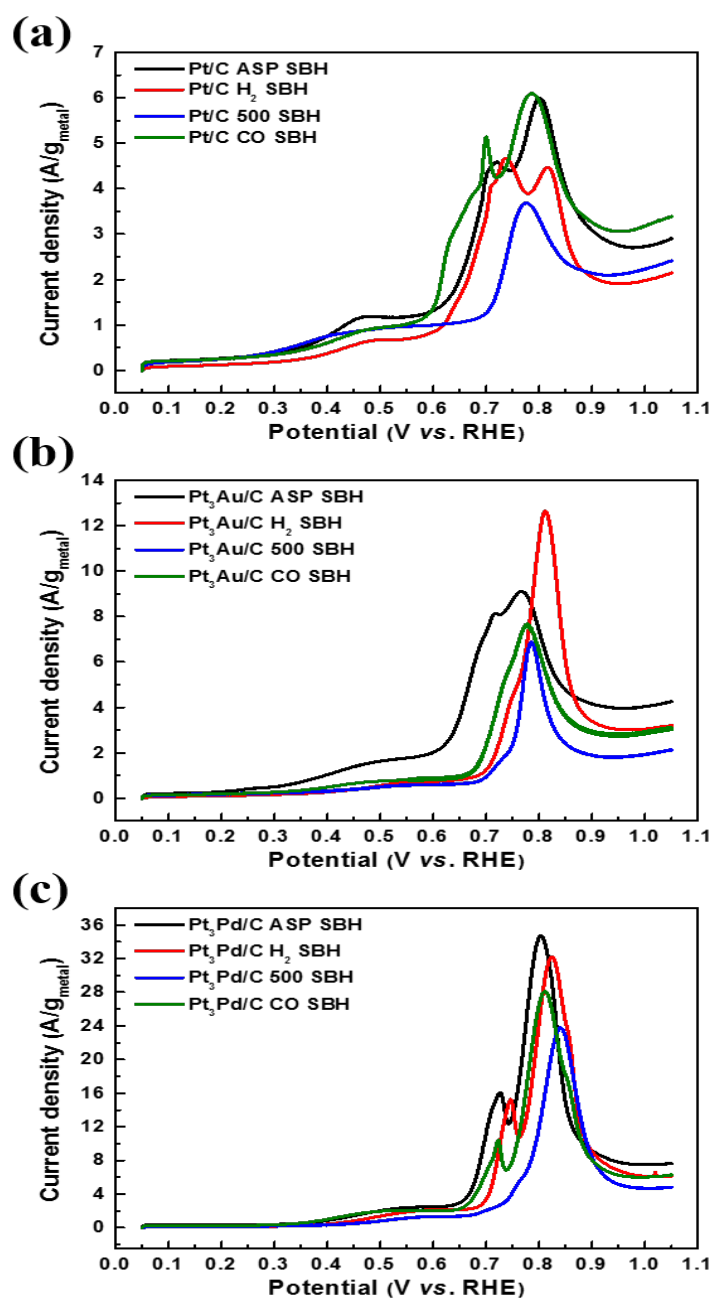


**Figure 3-15.** CO stripping voltammogram of carbon supported Pt and Pt-M (Au, Pd) NPs prepared by sodium borohydride method with various conditions.

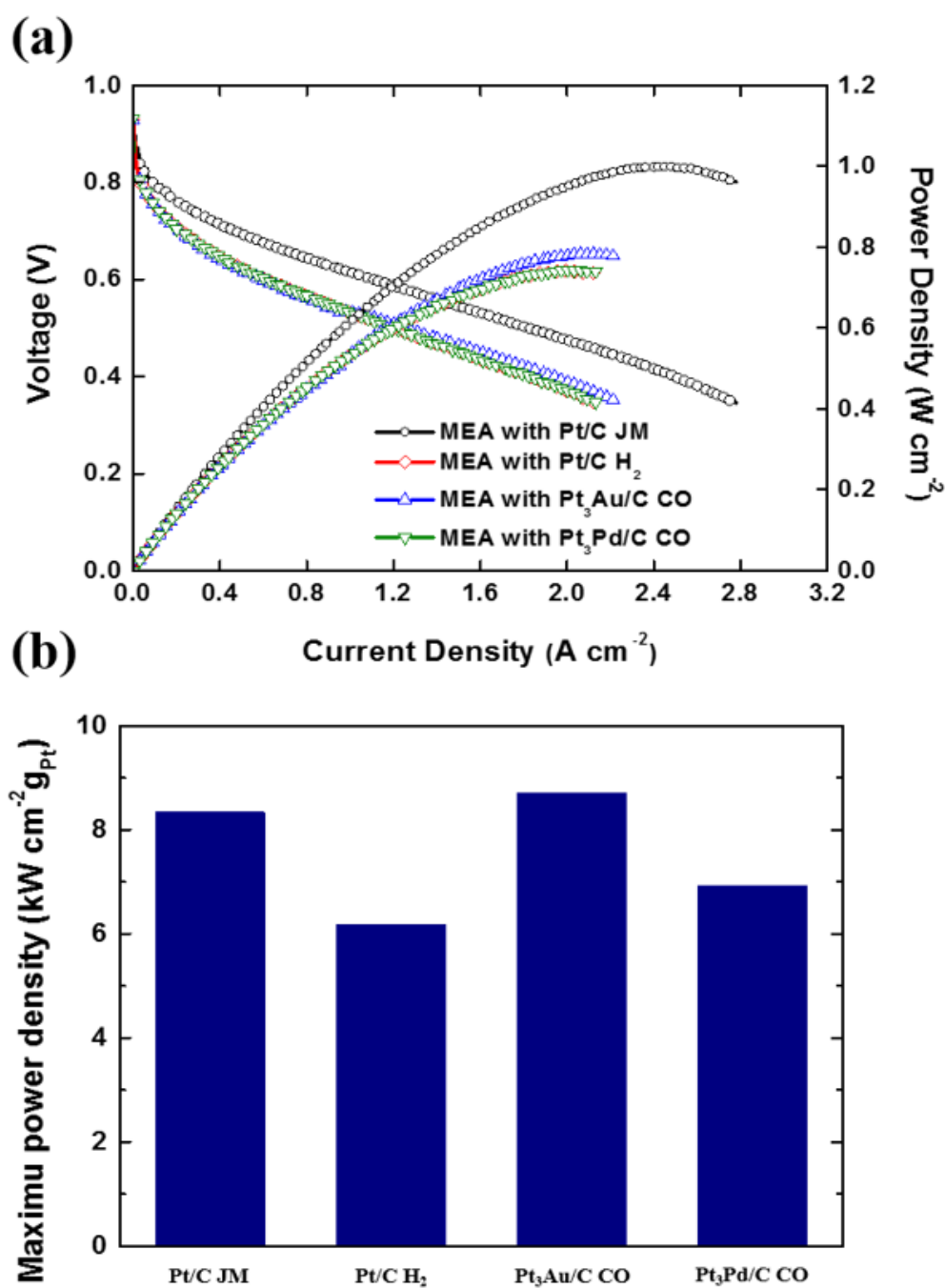


**Figure 3-16.** Single cell test of Pt bimetallic alloy NPs prepared by Al pitting corrosion method and their Pt mass normalized maximum power density.

Sample	Pt 4f						Au 4f (Pd 3d)	
	Pt <sup>0</sup>		Pt <sup>2+</sup>		Pt <sup>4+</sup>		Au <sup>0</sup> (Pd)	
	Peak (eV)	Area ratio	Peak (eV)	Area ratio	Peak (eV)	Area ratio	Peak (eV)	Area ratio
Pt/C ASP	71.53	0.66	72.7	0.21	74.58	0.13	-	-
Pt/C H <sub>2</sub>	71.78	0.74	73.07	0.19	74.75	0.07	-	-
Pt/C 500	71.85	0.70	73.14	0.20	74.99	0.10	-	-
Pt/C CO	71.82	0.67	73.08	0.24	75.09	0.09	-	-
Pt <sub>3</sub> Au/C ASP	71.72	0.64	72.82	0.28	75.01	0.08	84.50	1
Pt <sub>3</sub> Au/C H <sub>2</sub>	71.71	0.65	72.96	0.26	75.04	0.09	84.47	1
Pt <sub>3</sub> Au/C 500	71.63	0.65	72.69	0.26	74.8	0.09	84.36	1
Pt <sub>3</sub> Au/C CO	71.68	0.63	72.49	0.27	74.49	0.10	84.47	1
Pt <sub>3</sub> Pd/C ASP	71.72	0.52	72.53	0.38	74.5	0.10	336.31	-
Pt <sub>3</sub> Pd/C H <sub>2</sub>	71.65	0.63	72.69	0.25	74.55	0.12	336.38	-
Pt <sub>3</sub> Pd/C 500	71.62	0.64	72.73	0.24	74.69	0.12	336.37	-
Pt <sub>3</sub> Pd/C CO	72.04	0.62	73.07	0.24	74.72	0.14	336.39	-

**Table 3-1.** XPS deconvolution data of carbon supported Pt and Pt-M (Au, Pd) NPs prepared by Al pitting corrosion method.

Sample	Pt 4f						Au 4f (Pd 3d)	
	Pt <sup>0</sup>		Pt <sup>2+</sup>		Pt <sup>4+</sup>		Au <sup>0</sup> (Pd)	
	Peak (eV)	Area ratio	Peak (eV)	Area ratio	Peak (eV)	Area ratio	Peak (eV)	Area ratio
Pt/C ASP	71.3	0.63	72.08	0.22	73.19	0.15	-	-
Pt/C H <sub>2</sub>	71.34	0.68	72.2	0.26	73.27	0.06	-	-
Pt/C 500	71.36	0.70	72.28	0.26	73.24	0.04	-	-
Pt/C CO	71.33	0.65	72.1	0.17	73.06	0.18	-	-
Pt <sub>3</sub> Au/C ASP	71.35	0.67	72.16	0.18	73.03	0.15	84.11	1
Pt <sub>3</sub> Au/C H <sub>2</sub>	71.35	0.69	72.31	0.24	73.69	0.07	84.08	1
Pt <sub>3</sub> Au/C 500	71.33	0.70	72.31	0.28	73.91	0.02	84.09	1
Pt <sub>3</sub> Au/C CO	71.3	0.63	72.11	0.21	73.24	0.16	84.06	1
Pt <sub>3</sub> Pd/C ASP	71.51	0.49	72.22	0.44	74.25	0.07	335.82	-
Pt <sub>3</sub> Pd/C H <sub>2</sub>	71.83	0.61	72.71	0.26	73.91	0.13	335.59	-
Pt <sub>3</sub> Pd/C 500	71.38	0.60	72.19	0.27	73.37	0.13	335.77	-
Pt <sub>3</sub> Pd/C CO	71.32	0.53	72.02	0.26	72.89	0.21	335.72	-

**Table 3-2.** XPS deconvolution data of carbon supported Pt and Pt-M (Au, Pd) NPs prepared by sodium borohydride method.

## **3.2. Palladium-Iron Alloy Electrocatalyst via Modified Chemical Synthesis**

Published in doctorate thesis and reedited

(Kwang-Hyun Choi, 2013, Studies on Highly Active and Durable Pt

Nanocluster and PdFe Nanoparticles for Polymer Electrolyte Membrane Fuel Cells,

Seoul National University)

### **3.2.1. Physical characterization carbon supported Pd<sub>x</sub>Fe<sub>y</sub> NPs**

TEM images of ASP and HT samples with particle size distribution and mean particle diameter are shown in Figure 3-17. Particle growth was detected after the heat-treatment in the reductive atmosphere. The mean particle diameters of ASP and HT samples were found to be 3.89 nm, 3.44 nm, 3.52 nm for ASP Pd<sub>3</sub>Fe<sub>1</sub>, Pd<sub>1</sub>Fe<sub>1</sub> and Pd<sub>1</sub>Fe<sub>3</sub> and 12.23 nm, 10.23 nm, 8.05 nm for HT Pd<sub>3</sub>Fe<sub>1</sub>, Pd<sub>1</sub>Fe<sub>1</sub> and Pd<sub>1</sub>Fe<sub>3</sub>, respectively. The particle growth were significant as Pd/Fe ratio increased while the mean particle diameters of ASP samples were similar from one to another.

As shown in HRPD patterns (Figure 3-18.), broad polycrystalline Pd diffraction patterns are observed implying the formation of Pd-based alloy NPs (Peaks at 38°, 45° and 65° are assigned to Pd (111), (200), and (220) diffractions, respectively). (85) For ASP samples, sharp extra peaks are shown and the peaks become

prominent as Pd/Fe ratio decreases. The sharp extra peaks are probably ascribed to Fe precursor or complexes of Fe precursor and the stabilizer that were not reduced in the synthesis process. After the heat-treatment, the main peaks were moved to higher angle, which means the decrease in lattice parameter and the increase of alloying degrees of samples. (86, 87) In addition, the peak split and generation of new peaks at  $\sim 43.3^\circ$ ,  $51.6^\circ$ ,  $62.9^\circ$ ,  $83.1^\circ$ ,  $95.1^\circ$ ,  $129.3^\circ$  and more were detected especially in case of HT Pd<sub>1</sub>Fe<sub>1</sub> and Pd<sub>1</sub>Fe<sub>3</sub>. This is attributed to the appearance of new crystalline phases after the heat treatment. To identify these clearly, we conducted whole pattern profile matching method of HT samples. The fitted HRPD patterns of HT samples were expressed in Figure 3-2 (b), (c) and (d). From the fitted data, it is proved that in case of HT Pd<sub>1</sub>Fe<sub>1</sub> and Pd<sub>1</sub>Fe<sub>3</sub>, there are 3 phases, i) 3PdFe phase (space group : Fm3m), ii) PdFe phase (space group : P4/mmm) and iii) Fe phase, contrary to Pd<sub>3</sub>Fe<sub>1</sub>, only 3PdFe phase (space group : Fm3m). The phase 1 and 2 lattice parameters of HT samples are smaller than the lattice parameter of Pd-Pd as a reference (3.89 Å), resulted from alloying Pd with Fe. (The values are listed in Table 3-3) In other words, after the heat treatment, the alloying degree of samples increased and due to the difference in segregation energy of Pd and Fe, new crystalline phases were appeared. For the comparison, Pd<sub>x</sub>Fe<sub>y</sub> NPs were prepared via one-step polyol method at 165 °C for 1 h. TEM images of ASP and HT samples via one-step synthesis with particle size distribution and mean particle diameter are shown in Figure 3-19. Particle growth was detected after the heat-

treatment in the reductive atmosphere. The mean particle diameters of ASP and HT samples were found to be 4.65 nm, 3.28 nm, 4.78 nm for ASP Pd<sub>3</sub>Fe<sub>1</sub>, Pd<sub>1</sub>Fe<sub>1</sub> and Pd<sub>1</sub>Fe<sub>3</sub> and 14.61 nm, 7.14 nm, 6.47 nm for HT Pd<sub>3</sub>Fe<sub>1</sub>, Pd<sub>1</sub>Fe<sub>1</sub> and Pd<sub>1</sub>Fe<sub>3</sub>, respectively. In addition, to analyze the crystalline structure, X-ray powder diffraction data was obtained (Figure 3-20). Compared their diffraction spectra, the samples prepared by one-step synthesis have low crystallinity than samples with two-step synthesis due to its insufficient reducing power. In addition, due to incomplete synthesis, the order of the main peaks is different from the contents of Fe after the heat-treatment. In other words, two-step synthesis method is essential for complete synthesis of PdFe samples, especially for samples with high Fe contents.

In X-ray absorption near edge structure (XANES) region, a core-bound electron excited to quasi-bound states. The edge position is related to the valence of the absorbing atom. Figure 3-21 (a) presents Pd K-edge XANES spectra of the prepared samples. The absorption edges of the samples except ASP Pd<sub>1</sub>Fe<sub>3</sub> and HT Pd<sub>3</sub>Fe<sub>1</sub> are located at the same energy, indicating that the valence state of Pd element in the samples did not change significantly by the heat treatment and the Pd<sub>x</sub>Fe<sub>y</sub> composition. However, the absorption edge of ASP Pd<sub>1</sub>Fe<sub>3</sub> shifted to higher energy while that of HT Pd<sub>3</sub>Fe<sub>1</sub> shifted to lower energy. This suggests that the Pd element tend to have a metallic character by the heat treatment and the tendency is noticeable as the Pd/Fe ratio increased. On the other hand, higher valence state of Pd was

noticeable on the sample of low Pd/Fe ratio that did not undergo the heat-treatment. In Figure 3-21 (b), Fourier transformed Pd K-edge spectra were compared with that of Pd foil. The main peak centered at 2.5 Å corresponds to Pd-M (M = Pd and Fe) first coordination shell. FT magnitude increases on the HT samples and, among the HT samples, the FT magnitude increases with Pd/Fe ratio implying that the crystallinity of the samples were improved after the heat-treatment. The improved crystallinity of the HT samples becomes prominent as the Pd/Fe ratio increases while the crystallinity of ASP samples basically remained at the same extent in all Pd/Fe ratios. In addition to the main peak, a shoulder peak appears at 2.1 Å, which comes from the interference between the EXAFS oscillations of Pd-Pd and Pd-Fe. The shoulder peak is more remarkable as the Pd/Fe ratio decreases on the HT samples indicating formation of alloy structure. The Pd K-edge EXAFS spectra of HT samples were fitted and the results are shown in Table 3-3. As the Pd/Fe ratio decreases, the coordination number of Pd-Pd ( $N_{\text{Pd-Pd}}$ ) decreases and the coordination number of Pd-Fe ( $N_{\text{Pd-Fe}}$ ) increases. Considering the reported error range in Table 3-3, the changes in  $R_{\text{Pd-Pd}}$  and  $R_{\text{Pd-Fe}}$  is not detectable.

Fe K-edge XANES spectra of the prepared samples and Fe oxide references are shown in Figure 3-21 (c). The absorption edges of ASP samples are located at higher energy relative to HT samples and FeO<sub>2</sub> indicating that Fe elements in ASP samples has higher oxidation states than those in HT samples have and the Fe valence states are higher than Fe<sup>4+</sup>. The absorption edges of HT samples are found



to be in-between those of FeO and Fe<sub>3</sub>O<sub>4</sub>. Therefore, the valence states of HT samples must be higher than Fe<sup>2+</sup> and lower than Fe<sup>2.67+</sup>. As Pd/Fe ratio increases, the Fe elements were more reduced in the synthesis process. Pre-edge peaks centered at 7115 eV corresponds to an electron transition from 1s to 3d states of p-d hybridized. The pre-edge peaks are found to be higher on HT samples than on ASP samples reflecting more reduced states of Fe element in HT samples. Fourier transforms of Fe K-edge spectra are displayed in Figure 3-21 (d). Peaks of Fe foil centered at 2.2, 3.6, 4.5 Å reveal the body-centered cubic structure. The prepared samples, however, exhibits no bcc features. Peaks located at 1.45 Å account for Fe-O shell while peaks located at around 2.5 Å account for Fe-M shell (M = Fe and Pd). ASP samples exhibit mainly Fe-O magnitude with negligible Fe-M magnitude while HT samples exhibit remarkable Fe-M magnitude with significantly decreased Fe-O magnitude. (The fitted data is expressed in Table 3-3) Therefore, Fe elements in ASP samples are composed of oxide phase with low crystallinity, whereas considerable amounts of Fe elements in HT samples are reduced to metallic phase with better crystallinity.

From the HRPD fitted data and XAS analysis, we can make a description of crystalline structures of samples. After the heat treatment, the alloying degree and crystallinity of HT samples increased due to the reduction of Fe oxide from HRPD peak shift and XAS fitting data. In addition, from the fitted HRPD data, in case of HT Pd<sub>1</sub>Fe<sub>1</sub> and Pd<sub>1</sub>Fe<sub>3</sub>, the appearance of new crystalline phases after the heat

treatment was identified because of the difference in segregation energy of Pd and Fe.

XPS spectra were obtained to analyze the surface and electronic structure of ASP and HT samples. (Figure 3-22, 23) As shown in Figure 3-22 (a), the core-level Pd 3d spectra of ASP and HT Pd<sub>x</sub>Fe<sub>y</sub> display a doublet signal for Pd 3d<sub>3/2</sub> and Pd 3d<sub>5/2</sub>, respectively and these spectra were deconvoluted to Pd<sup>0</sup>, Pd<sup>2+</sup> and Pd<sup>4+</sup>. The XPS deconvolution data are presented in Table 3-4. When compared with the binding energy 334.9 eV of pure Pd, a shift of Pd<sup>0</sup> to a higher binding energy was detected for every sample, induced by alloying with Fe and much higher binding energy shift was identified for HT Pd<sub>x</sub>Fe<sub>y</sub> (especially in HT Pd<sub>1</sub>Fe<sub>1</sub> and Pd<sub>1</sub>Fe<sub>3</sub>) (Figure 3-24). It is interpreted that the electron transfer from Fe to Pd due to the Pd<sub>x</sub>Fe<sub>y</sub> alloy formation and the difference in electronegativity between Pd and Fe makes the d-band of Pd broader than before and results in downshift of d-band center of Pd. As the consequence of this, the binding energy of Pd<sup>0</sup> in ASP and HT samples shifted to higher values.

It is commonly believed that the value of d-band center is regarded as the important descriptor to explain ORR activity of electrocatalyst because this value determines the affinity with oxygen species such as O, OH generated during ORR. High affinity with oxygen species results from high value of d-band center, vice versa. In other words, by tailoring the value of d-band center, the rate of ORR can be changed. Therefore, from electron transfer or structural modifications caused by

alloying and post heat treatment, the value of d-band center and the affinity with oxygen species can be decreased to optimum point for ORR. In this study, by alloying Pd with Fe and the heat treatment, binding energy of Pd<sup>0</sup> was shifted to higher values in XPS spectra and d-band center of Pd moved to lower values. Therefore, it is expected that HT Pd<sub>x</sub>Fe<sub>y</sub> samples will exhibit good ORR activity and among these, HT Pd<sub>1</sub>Fe<sub>1</sub> will show the highest catalytic performance. (58)

In addition, after the heat treatment, the amount of Pd<sup>0</sup> increases due to the reducing atmosphere of the heat treatment. Figure 3-22 (b) presents the XPS spectra for the Fe 2p core level region, characterized by the 2p peaks around 712 eV for 2p<sub>3/2</sub> and 727 eV for 2p<sub>1/2</sub> which can be assigned to the formation of Fe oxide species. Peaks of metallic Fe (near 707 eV for 2p<sub>3/2</sub>) were hardly detected, indicating that Fe oxides were dominant on their surface. In addition, after the heat treatment, the intensities of Fe 2p peaks of samples is decreased, which means the surface atomic composition of Pd is very high due to Pd surface segregation induced by thermal energy.

The surface atomic composition of Pd and Fe was calculated from the XPS intensity of Pd 3d<sub>3/2</sub> and Fe 2p<sub>3/2</sub> with correction of the photoelectron cross section and was compared to the bulk composition of samples. (Figure 3-25, 26) (88) The surface and bulk composition of samples calculated from XPS spectra are presented in Figure 3-24. As mentioned above, it is reported that when PdFe NPs are treated in high temperature of reducing atmosphere, Pd atoms are segregated and the

surface composition of Pd after heat treatment increases. In this study, HT samples exhibited higher Pd surface composition than those of ASP samples. The surface atomic fractions of Pd of ASP and HT Pd<sub>x</sub>Fe<sub>y</sub> are 36.6 %, 26.9 % and 19.6 % for ASP Pd<sub>3</sub>Fe<sub>1</sub>, Pd<sub>1</sub>Fe<sub>1</sub> and Pd<sub>1</sub>Fe<sub>3</sub> and 92.5 %, 87.5 % and 87.4 % for HT Pd<sub>3</sub>Fe<sub>1</sub>, Pd<sub>1</sub>Fe<sub>1</sub> and Pd<sub>1</sub>Fe<sub>3</sub>. The bulk Pd fractions of samples are 72.0 %, 50.0 % and 25.0 % for Pd<sub>3</sub>Fe<sub>1</sub>, Pd<sub>1</sub>Fe<sub>1</sub> and Pd<sub>1</sub>Fe<sub>3</sub>, confirmed by ICP-AES. It is concluded that due to the heat treatment, surface composition of samples was changed and atomic fraction of Pd increased, resulting in Pd rich surface structures. For samples prepared by one-step synthesis, the surface atomic fractions of Pd of ASP and HT Pd<sub>x</sub>Fe<sub>y</sub> are 41.4 %, 26.2 % and 14.2 % for ASP Pd<sub>3</sub>Fe<sub>1</sub>, Pd<sub>1</sub>Fe<sub>1</sub> and Pd<sub>1</sub>Fe<sub>3</sub> and 54.9 %, 51.0 % and 45.0 % for HT Pd<sub>3</sub>Fe<sub>1</sub>, Pd<sub>1</sub>Fe<sub>1</sub> and Pd<sub>1</sub>Fe<sub>3</sub>. The bulk Pd fractions of samples are 71.2 %, 40.1 % and 18.6 % for Pd<sub>3</sub>Fe<sub>1</sub>, Pd<sub>1</sub>Fe<sub>1</sub> and Pd<sub>1</sub>Fe<sub>3</sub>, confirmed by ICP-AES.

### **3.2.2. Electrochemical characterizations of carbon supported Pd<sub>x</sub>Fe<sub>y</sub> NPs**

In Figure 3-27 (a) and (c), the results of the CV was expressed. All CV measurement were repeated to obtain stable CV curves and as a result, there are no any evidences of Fe oxide (or hydroxide) in CV. Every sample exhibited typical hydrogen region at 0.2 V vs. RHE and Pd oxide formation and reduction peak near 0.8 V vs. RHE. In addition, when comparing the onset potential of the formation and reduction of Pd oxide, HT Pd<sub>1</sub>Fe<sub>1</sub> and Pd<sub>1</sub>Fe<sub>3</sub> showed higher onset potential

than HT Pd<sub>3</sub>Fe<sub>1</sub>. It is interpreted HT Pd<sub>1</sub>Fe<sub>1</sub> and Pd<sub>1</sub>Fe<sub>3</sub> has lower oxophilicity than Pd<sub>3</sub>Fe<sub>1</sub> and it is expected that HT Pd<sub>1</sub>Fe<sub>1</sub> and Pd<sub>1</sub>Fe<sub>3</sub> will exhibit higher ORR activities than Pd<sub>3</sub>Fe<sub>1</sub>. (89, 90) The rotating disk electrode (RDE) technique was used to conduct assessment of the activity for oxygen reduction reaction in 0.1 M HClO<sub>4</sub> solution in Figure 3-27 (b) and (d). The ORR polarization curve measurements were initiated in the positive direction from 0.05 V to 1.05 V vs RHE. It is manifested that half-wave potentials increased in following order: ASP Pd<sub>1</sub>Fe<sub>3</sub> < ASP Pd<sub>1</sub>Fe<sub>1</sub> < ASP Pd<sub>3</sub>Fe<sub>1</sub>, respectively. HT samples exhibited dramatic increase in ORR half wave potential. The half-wave potentials increased in following order: HT Pd<sub>3</sub>Fe<sub>1</sub> < HT Pd<sub>1</sub>Fe<sub>3</sub> < HT Pd<sub>1</sub>Fe<sub>1</sub>. In case of HT Pd<sub>1</sub>Fe<sub>1</sub> and HT Pd<sub>1</sub>Fe<sub>3</sub>, the activity of this exceed that of conventional Pt catalyst. The Pd mass normalized kinetic current density of HT Pd<sub>1</sub>Fe<sub>1</sub> and Pd<sub>1</sub>Fe<sub>3</sub> at 0.9 V vs. RHE was higher than that of commercial Pt catalyst by about 3 times (Figure 3-28.).

To analyze the structural changes and elucidate the enhancement of ORR activity after the heat treatment, CO oxidation method was conducted by using CV technique in Figure 3-90 (a) and (c). Before the measurement, CO molecules was adsorbed on Pd<sub>x</sub>Fe<sub>y</sub> NPs at potential of 0.05 V vs. RHE for 15 min and electrolyte was purged with Ar gas for 30 min. Then, adsorbed CO molecules were oxidized electrochemically via potentials sweep from 0.05 V to 1.05 V vs. RHE. From this, we calculated electrochemically active surface area (ECSA) with a charge density of 490  $\mu\text{C}/\text{cm}^2$  for CO adsorption area on Pd. (91) The ECSAs of ASP and HT

samples were 103.65 m<sup>2</sup>/g, 55.45 m<sup>2</sup>/g, 47.62 m<sup>2</sup>/g for ASP Pd<sub>3</sub>Fe<sub>1</sub>, Pd<sub>1</sub>Fe<sub>1</sub> and Pd<sub>1</sub>Fe<sub>3</sub> and 33.81 m<sup>2</sup>/g, 18.48 m<sup>2</sup>/g, 18.67 m<sup>2</sup>/g for HT Pd<sub>3</sub>Fe<sub>1</sub>, Pd<sub>1</sub>Fe<sub>1</sub> and Pd<sub>1</sub>Fe<sub>3</sub>, respectively. After the heat treatment, particle size of samples largely increased and because of that (Figure 3-17), the ECSA of samples was decreased greatly by ~70 %. In addition, in case of Pd<sub>1</sub>Fe<sub>1</sub> and Pd<sub>1</sub>Fe<sub>3</sub>, the peak shape was changed and oxidation peaks moved to higher potentials. For Pd<sub>3</sub>Fe<sub>1</sub>, however, changes in peak shape and potentials were not significant. (Figure 3-30 (c)) It means due to the heat treatment, Pd<sub>1</sub>Fe<sub>1</sub> and Pd<sub>1</sub>Fe<sub>3</sub> samples underwent structural modifications causing changes in electronic structure. In Table 3-4, HT Pd<sub>1</sub>Fe<sub>1</sub> and Pd<sub>1</sub>Fe<sub>3</sub> showed large binding energy shift to higher value compared to Pd<sub>3</sub>Fe<sub>1</sub> after the heat treatment, which means great downshift of d-band center. It is regarded as the decrease in binding energy for oxygen species and oxophilicity of Pd. In the same vein, as oxophilicity of samples decreases, adsorbed CO oxidation peaks will move to higher potentials. Therefore, these results are in good agreement with the ORR activity trends of samples. Additionally, N<sub>2</sub>O reduction analysis was conducted to obtain information about electronic structure of samples indirectly (Figure 3-31 (b) and (d)). As the adsorption and reduction of N<sub>2</sub>O can occur only at free sites, the reduction rate will be maximized when the amount of adsorbed ions becomes minimum value, indicating the potential of zero total charge (PZTC). (92) It is believed that the value of PZTC has a relationship with work function, surface structure and specific adsorption properties of electrocatalyst, the ORR activity can be analyzed in terms

of PZTC. When it comes to the relationship between ORR activity and PZTC, as the PZTC value increases to higher potential, the binding energy with oxygen species decreases and ORR activity also increases. In other words, the increase in PZTC value means that it becomes hard to oxidize the surface of electrocatalyst and it can be interpreted that the affinity with oxygen species decreases and it facilitates the kinetics of ORR consequently. For ASP  $\text{Pd}_x\text{Fe}_y$ , the trend of potential at maximum reduction current is different from ORR activity. It might be due to the oxide (or hydroxide) formation of ASP samples. For HT  $\text{Pd}_x\text{Fe}_y$  samples, however, HT  $\text{Pd}_1\text{Fe}_1$  has the highest potential value and HT  $\text{Pd}_1\text{Fe}_3$ , HT  $\text{Pd}_3\text{Fe}_1$  follow in turn, which has the same trend with ORR activity.

Drastic increase of half wave potentials and the trends of these among HT  $\text{Pd}_x\text{Fe}_y$  NPs for oxygen reduction reaction can be explained as follows. First, HT  $\text{Pd}_x\text{Fe}_y$  NPs have higher alloying degrees from the reduction of Fe oxide (or hydroxide) by the heat treatment and because of this, the electronic states of samples can be tuned to get optimal values for ORR, which are supported by XAS and XPS data before mentioned. The shift of binding energy of XPS spectra to higher value after the heat treatment induces downshift of d-band center of Pd, resulting in better ORR activity. Among HT  $\text{Pd}_x\text{Fe}_y$  samples, HT  $\text{Pd}_1\text{Fe}_1$  exhibited the biggest binding energy shift to higher value, which means the most downshift of d-band center and shows best ORR activity in turn. Second, by the heat treatment, HT  $\text{Pd}_x\text{Fe}_y$  NPs have higher concentration of Pd on their surface compared to ASP  $\text{Pd}_x\text{Fe}_y$  confirmed by XPS

quantitative analysis. Because of those, these HT samples showed better ORR performance compared to ASP samples. As reported in previous works, it is believed that high Pd concentration on the surface of Pd alloys induced by the heat treatment results in higher ORR activity. In addition, due to the heat treatment, new crystalline structures were generated in case of HT Pd<sub>1</sub>Fe<sub>1</sub> and HT Pd<sub>1</sub>Fe<sub>3</sub>, which are detected in HRPD patterns. In recent researches about electrocatalyst for ORR, Pt bimetallic alloys (PtFe, PtCo etc.) with ordered crystalline structure exhibited better ORR activity compared to disordered one. Therefore it is possible to apply this theory to Pd based alloy electrocatalyst for elucidating outstanding ORR performance. Because of the effects of both above, HT Pd<sub>1</sub>Fe<sub>1</sub> exhibited the best ORR activity among samples and HT Pd<sub>1</sub>Fe<sub>3</sub>, HT Pd<sub>3</sub>Fe<sub>1</sub> follow in turn.

For the comparison, the electrochemical properties of Pd<sub>x</sub>Fe<sub>y</sub> NPs prepared via one-step was measured (Figure 3-29 and 3-31). For ASP samples, except Pd<sub>3</sub>Fe<sub>1</sub> sample, they did not exhibit H<sub>upd</sub> region, which means that their surfaces were deactivated by oxide and high Fe fraction on their surface due to low reducing power of one-step synthesis in case of high Fe contents. Contrary to this, after the heat treatment, HT samples exhibited H<sub>upd</sub> area, which means that due to thermal energy, surface segregation of Pd on NPs was triggered. The ECSAs of ASP and HT samples prepared by one-step synthesis were 40.61 m<sup>2</sup>/g, 6.49 m<sup>2</sup>/g, 2.85 m<sup>2</sup>/g for ASP Pd<sub>3</sub>Fe<sub>1</sub>, Pd<sub>1</sub>Fe<sub>1</sub> and Pd<sub>1</sub>Fe<sub>3</sub> and 16.86 m<sup>2</sup>/g, 10.74 m<sup>2</sup>/g, 9.37 m<sup>2</sup>/g for HT Pd<sub>3</sub>Fe<sub>1</sub>, Pd<sub>1</sub>Fe<sub>1</sub> and Pd<sub>1</sub>Fe<sub>3</sub>, respectively. For ORR activity, due to the reasons



before mentioned, HT samples have better ORR activity than ASP samples, however, their activity are much lower than HT samples prepared by two-step synthesis and conventional Pt catalyst. CO oxidation curves of samples prepared by one-step synthesis are very different from those of samples prepared by two-step synthesis. It is because of different surfaces structure with deactivated surface by oxide and high Fe fraction due to low reducing power. In addition, the order of onset potential values of CO oxidation and ORR activity is different, which is because of different surfaces structure before mentioned.

In addition, accelerated durability test (ADT) of HT samples prepared by two-step synthesis was conducted via potential cycling method in the range of 0.6 to 1.0 V vs. RHE with a scan rate of 100 mV/s for 5000 cycles (Figure 3-32 and 3-33). After ADT, their ORR activities decreased significantly. It is due to the dissolution of Pd and Fe during the potential cycling, which is displayed in CV. The CV graph after ADT is different from those of samples before ADT. Especially in HT Pd<sub>3</sub>Fe<sub>1</sub> and Pd<sub>1</sub>Fe<sub>1</sub>, their shape of H<sub>upd</sub> region became similar to that of Pd, which means during the potential cycling, Fe dissolved electrochemically faster than Pd. Due to this, among samples, HT Pd<sub>3</sub>Fe<sub>1</sub> showed the highest half-wave potential and ORR activity after ADT.

Lastly, the single cell performance test was conducted with HT Pd<sub>x</sub>Fe<sub>y</sub> NPs under the condition that fully humidified H<sub>2</sub> and O<sub>2</sub> gas were supplied into the anode and cathode, respectively (Figure 3-34). It is shown that MEA with the synthesized Pd

alloy NPs exhibited comparable performance without any modifications of electrode structure and system. In addition, they showed much higher Pd mass normalized maximum power density by  $\sim 2.5$  times in case of HT Pd<sub>1</sub>Fe<sub>3</sub>, which is in the same vein with above mentioned ORR data.

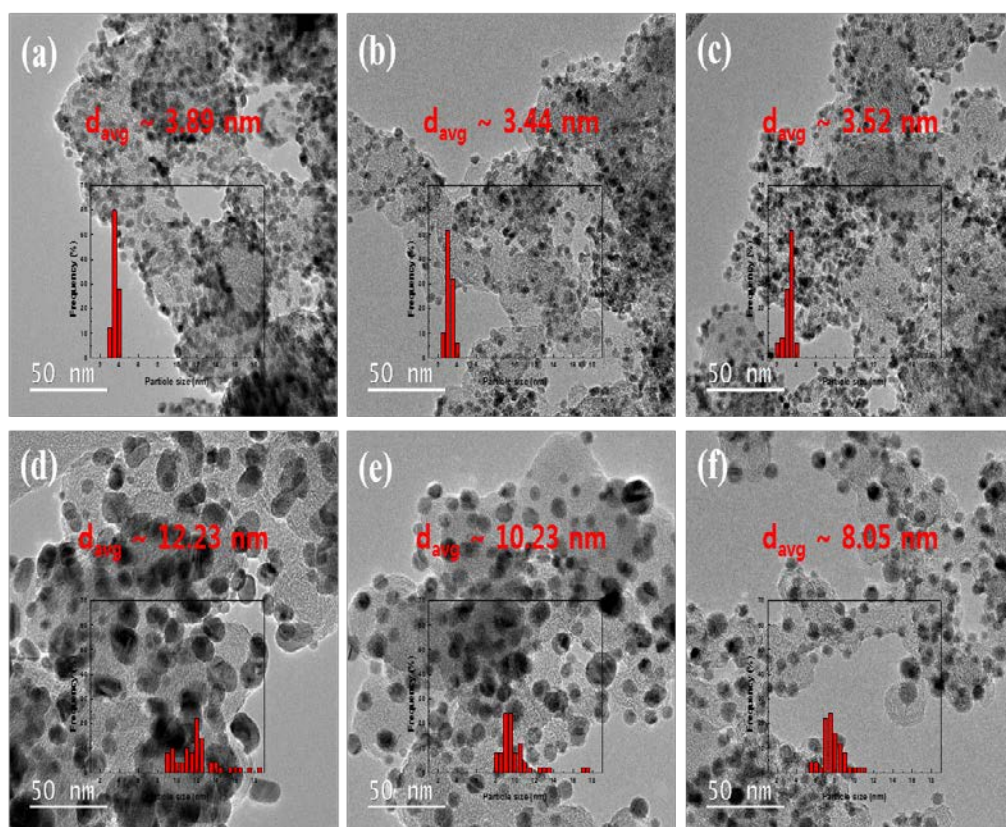


**Figure 3-17.** TEM images of ASP and HT  $\text{Pd}_x\text{Fe}_y$  samples prepared by two-step synthesis with particle size distribution and mean particle diameter. (a) and (d) for ASP and HT  $\text{Pd}_3\text{Fe}_1$ , (b) and (e) for ASP and HT  $\text{Pd}_1\text{Fe}_1$ , (c) and (f) for ASP and HT  $\text{Pd}_1\text{Fe}_3$ .

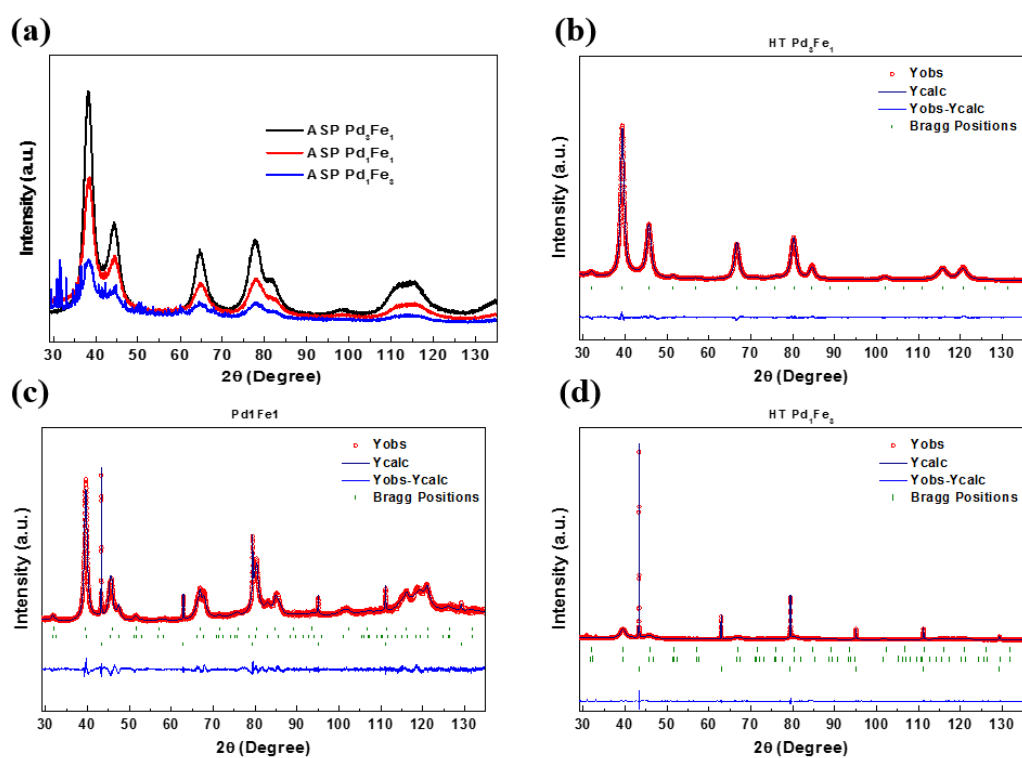


**Figure 3-18.** HRPD patterns of ASP and HT samples prepared by two-step synthesis and their whole pattern matching data.

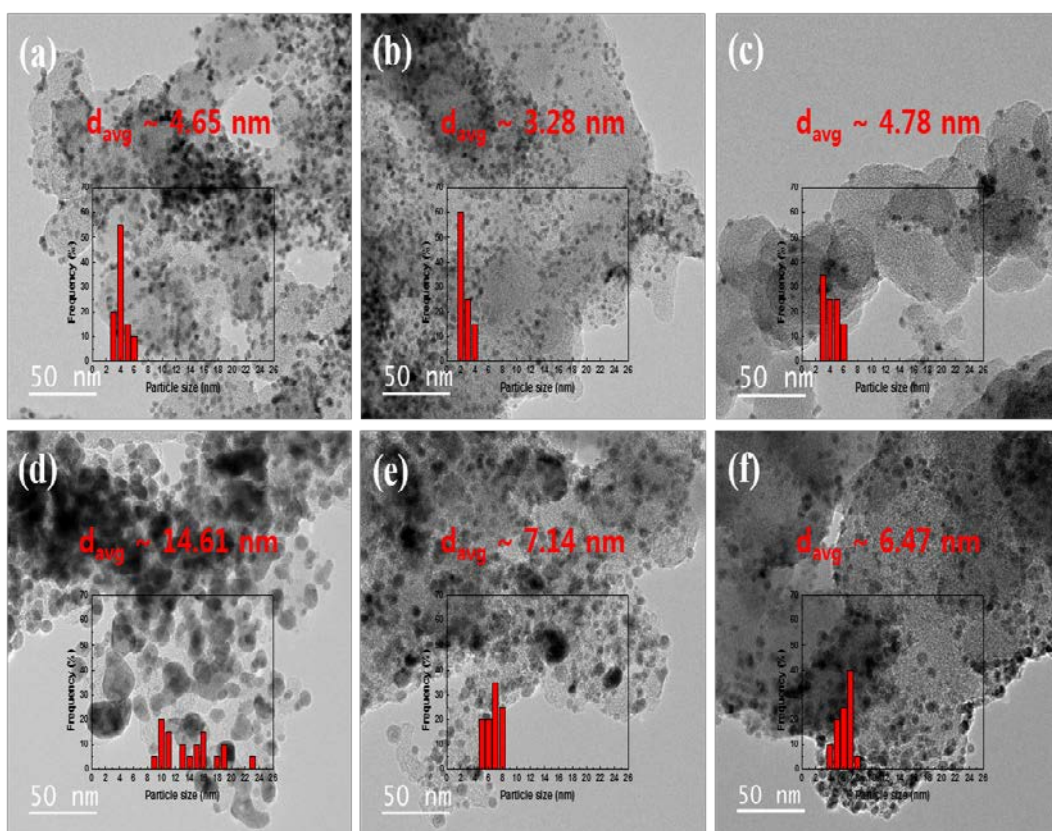


**Figure 3-19.** TEM images of ASP and HT  $\text{Pd}_x\text{Fe}_y$  samples prepared by one-step synthesis with particle size distribution and mean particle diameter. (a) and (d) for ASP and HT  $\text{Pd}_3\text{Fe}_1$ , (b) and (e) for ASP and HT  $\text{Pd}_1\text{Fe}_1$ , (c) and (f) for ASP and HT  $\text{Pd}_1\text{Fe}_3$ .

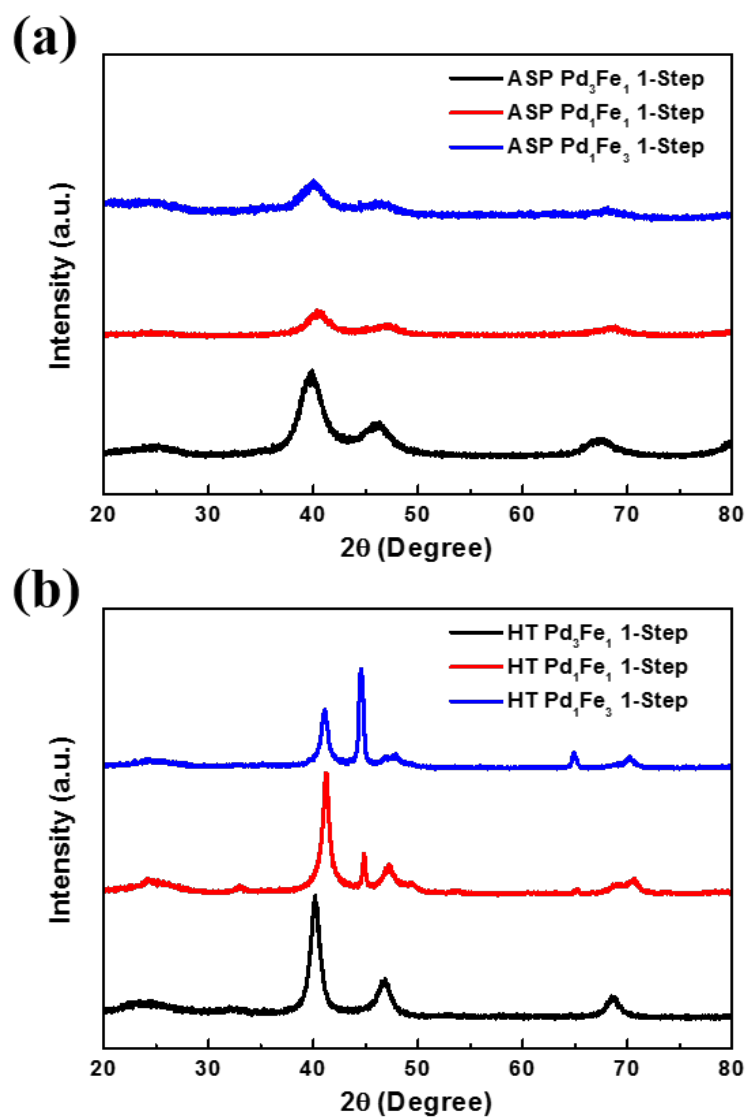


**Figure 3-20.** XRD patterns of ASP and HT samples prepared by one-step synthesis.

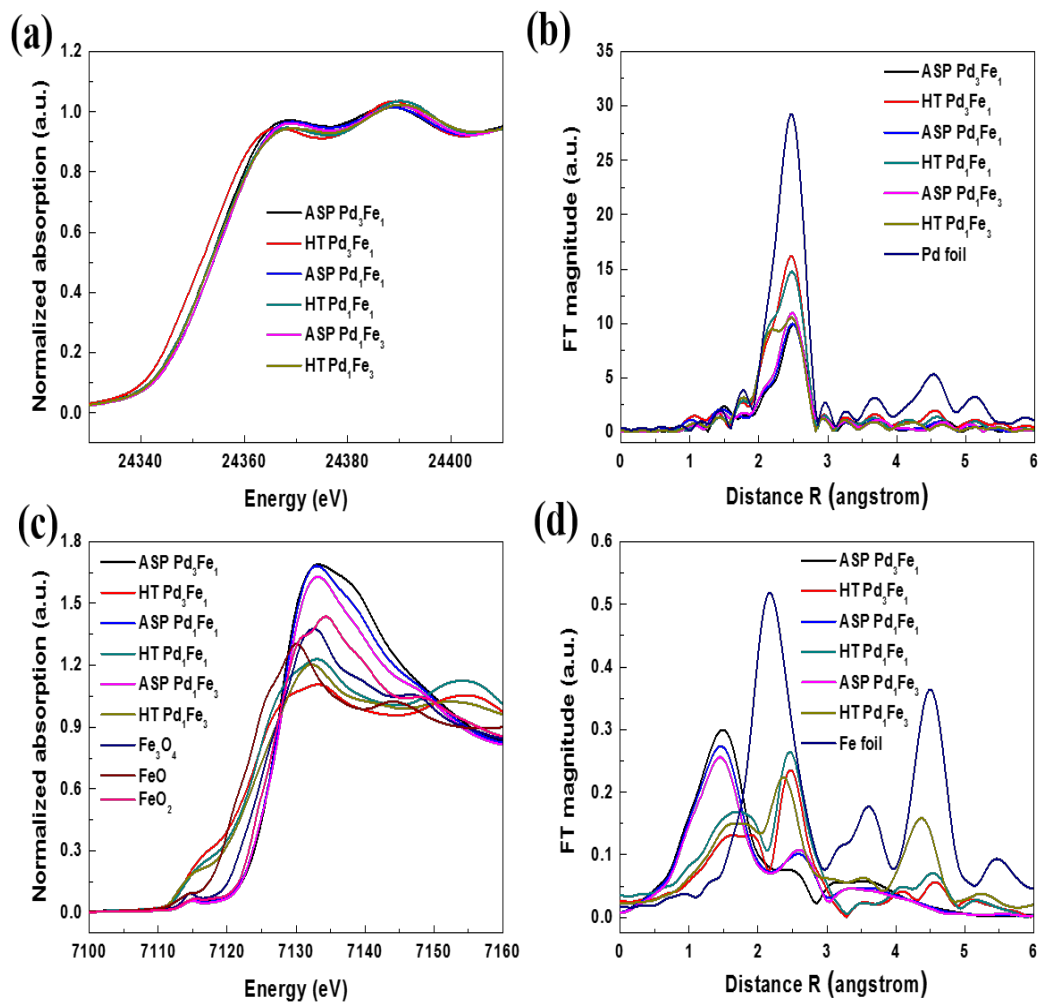


**Figure 3-21.** XAS characterization of ASP and HT Pd<sub>x</sub>Fe<sub>y</sub> samples prepared by two-step synthesis for (a) Pd K-edge and (c) Fe K-edge and their Fourier transformed spectra for (a) Pd K-edge and (c) Fe K-edge.

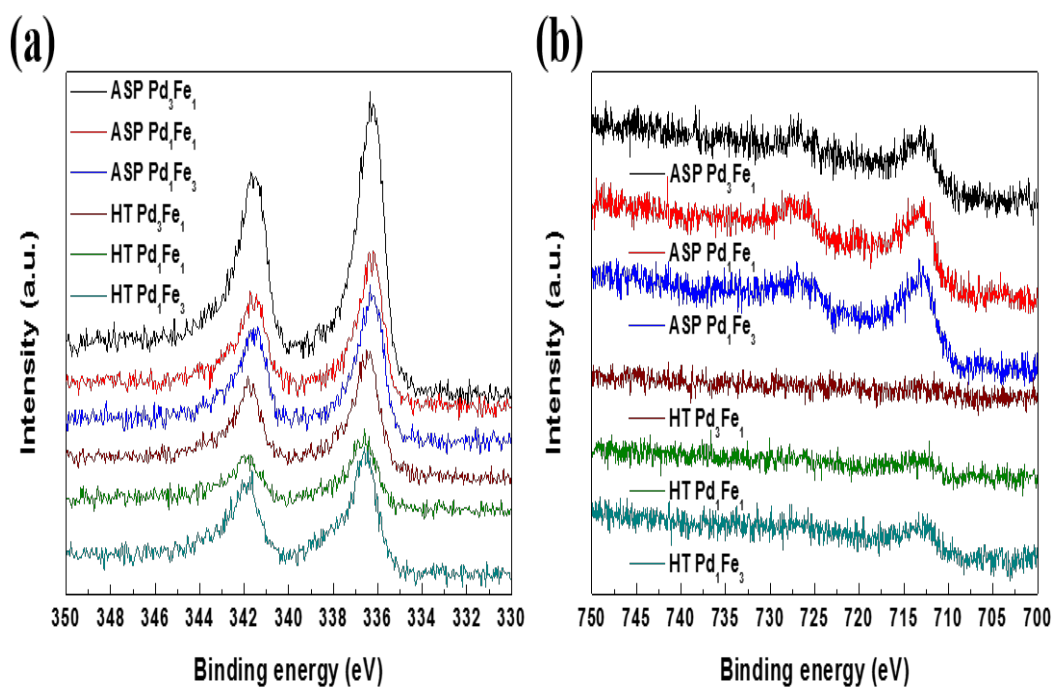


**Figure 3-22.** XPS spectra of ASP and HT Pd<sub>x</sub>Fe<sub>y</sub> samples prepared by two-step synthesis (a) Pd 3d and (b) Fe 2p.



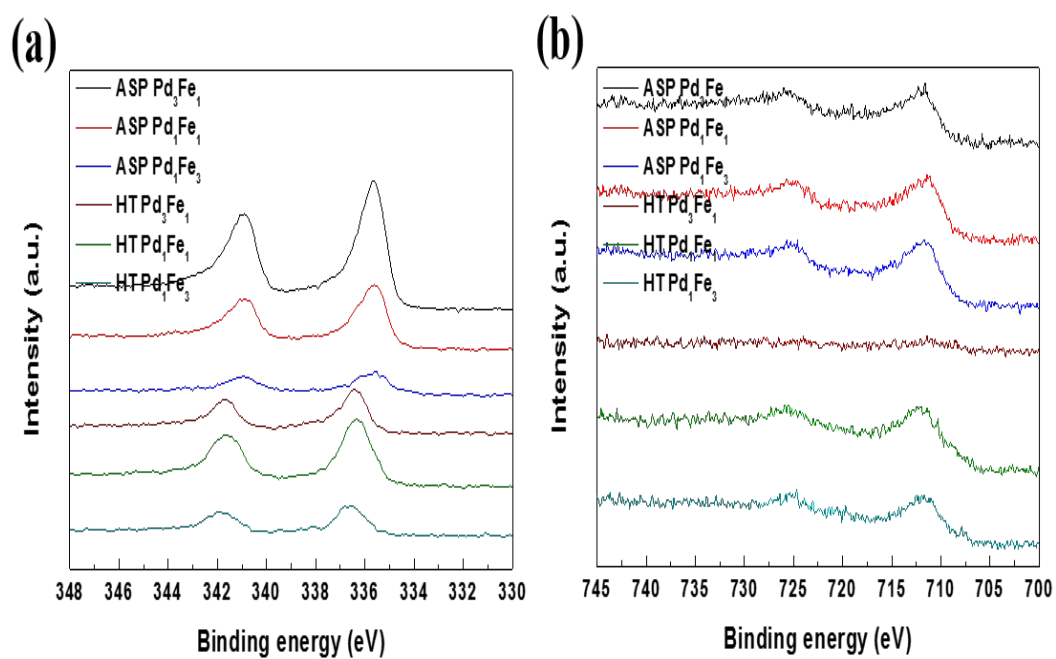


**Figure 3-23.** XPS spectra of ASP and HT  $\text{Pd}_x\text{Fe}_y$  samples prepared by one-step synthesis (a) Pd 3d and (b) Fe 2p.

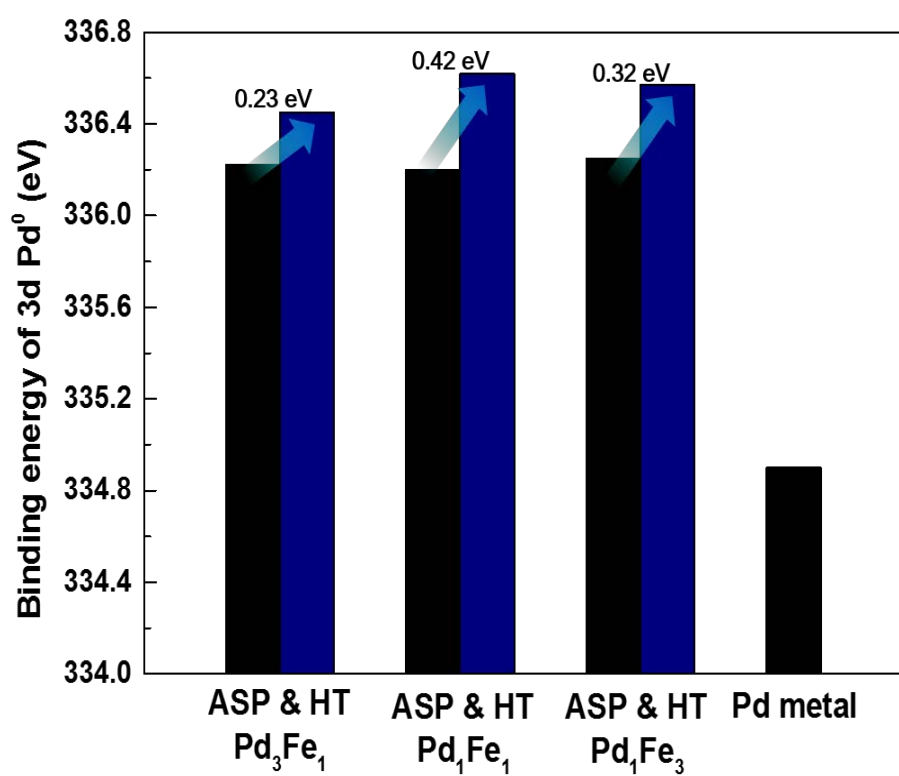


**Figure 3-24.** Comparison of binding energies of 3d Pd<sup>0</sup> of Pd<sub>x</sub>Fe<sub>y</sub> alloy NPs prepared by two-step synthesis.

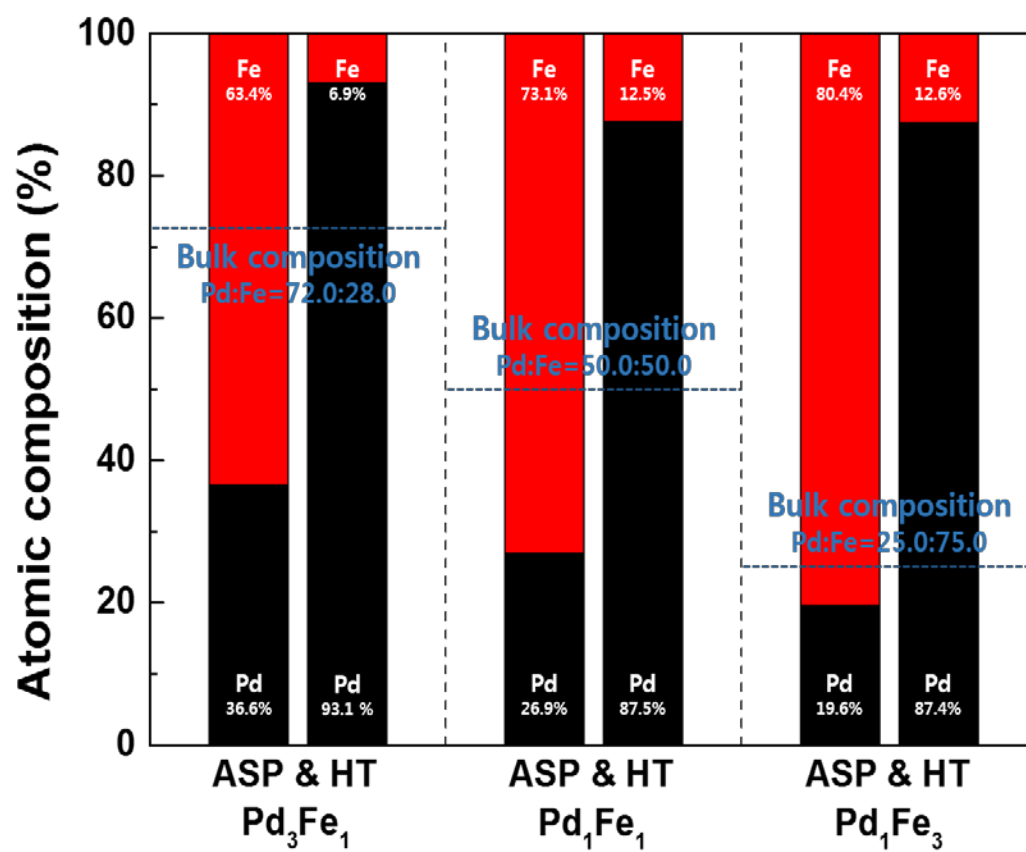


**Figure 3-25.** Comparison of bulk and surface atomic composition of ASP and HT Pd<sub>x</sub>Fe<sub>y</sub> samples prepared by two-step synthesis.

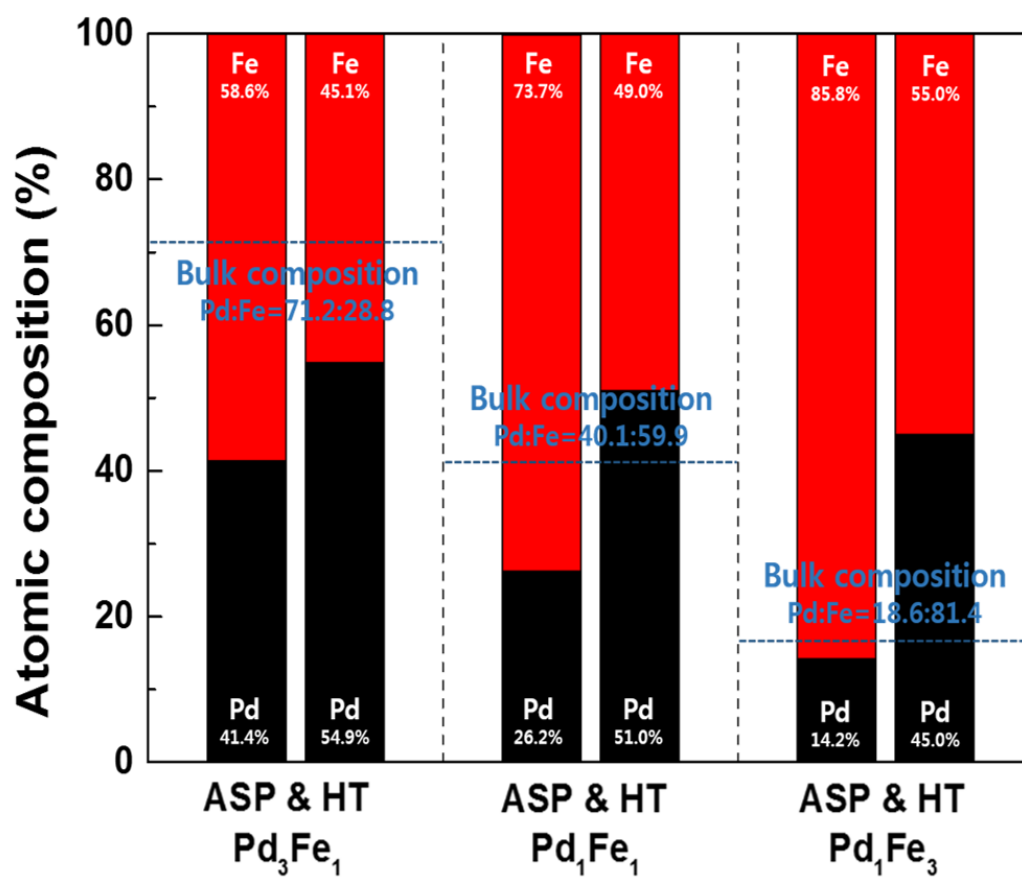


**Figure 3-26.** Comparison of bulk and surface atomic composition of ASP and HT Pd<sub>x</sub>Fe<sub>y</sub> samples prepared by one-step synthesis.

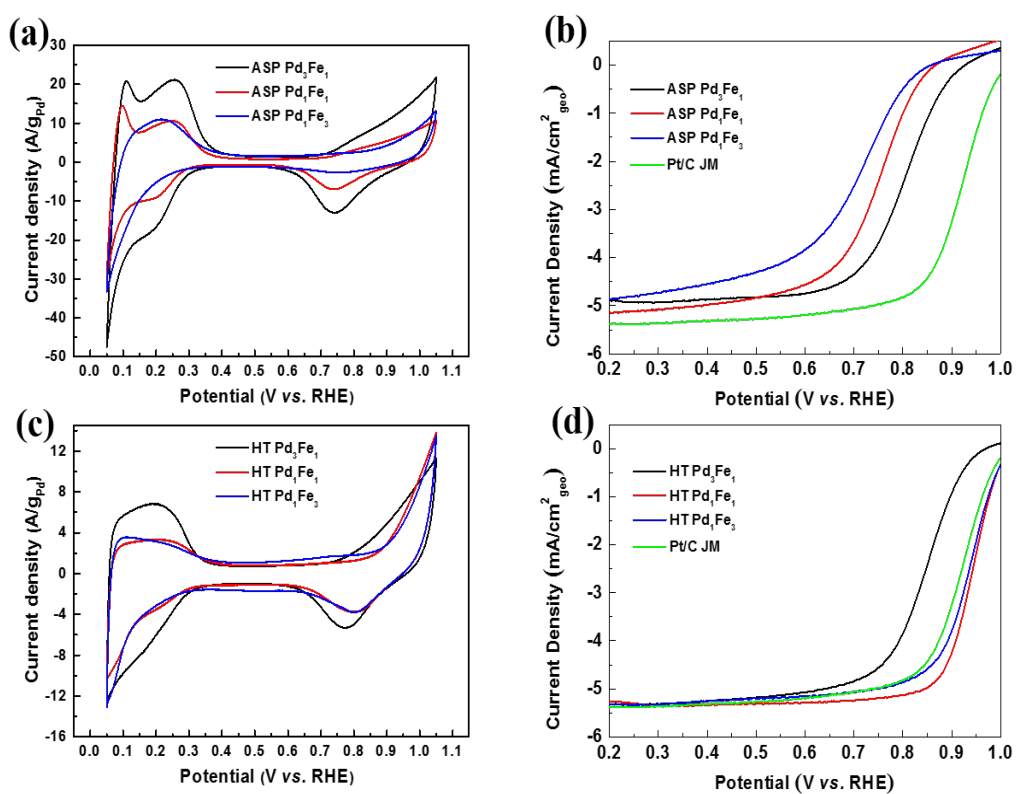


**Figure 3-27.** Cyclic voltammogram ((a), (c)) and ORR polarization curve ((b), (d)) of ASP and HT Pd<sub>x</sub>Fe<sub>y</sub> samples prepared by two-step synthesis.

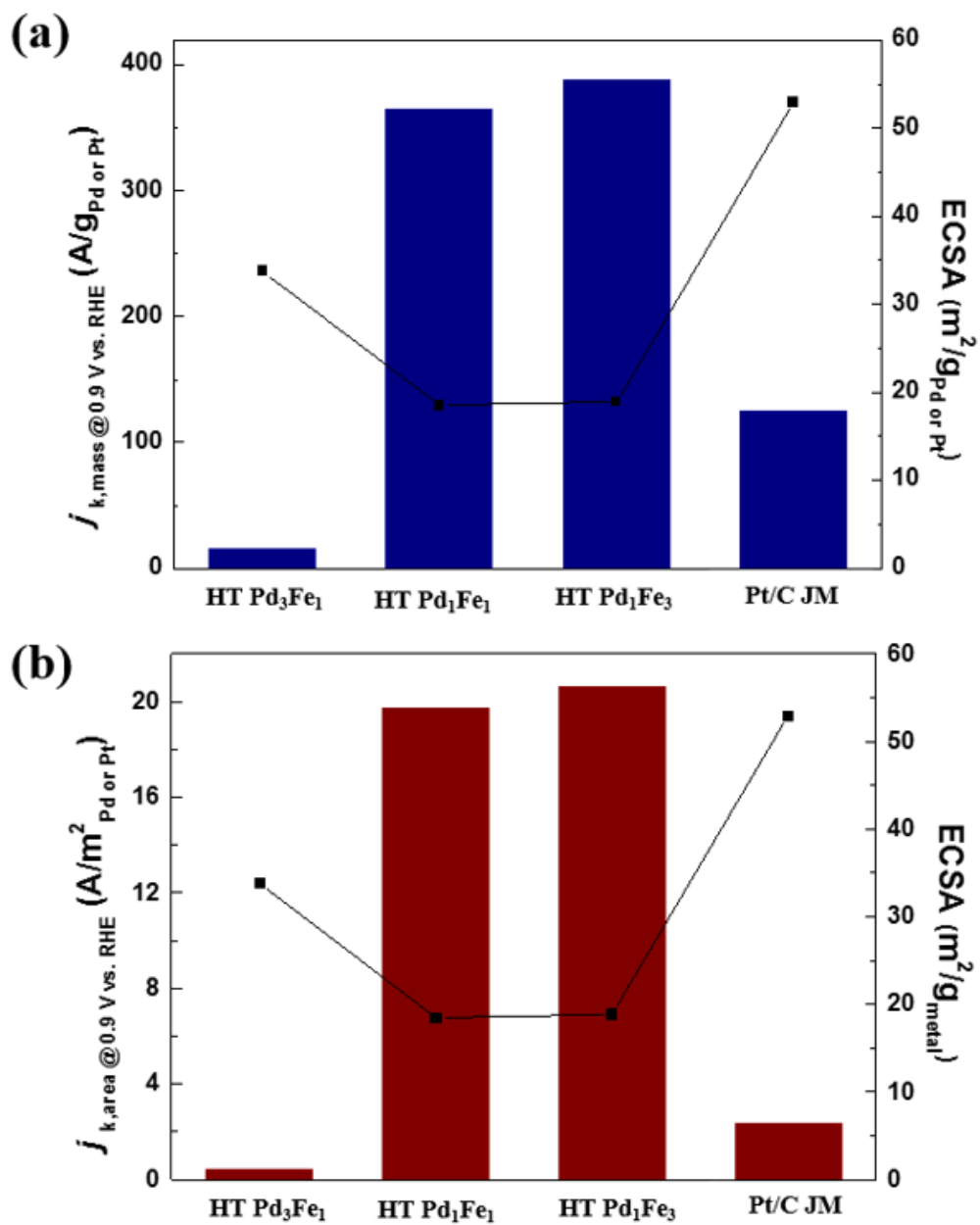


**Figure 3-28.** (a) Mass and (b) area normalized ORR activity at 0.9 V vs. RHE.

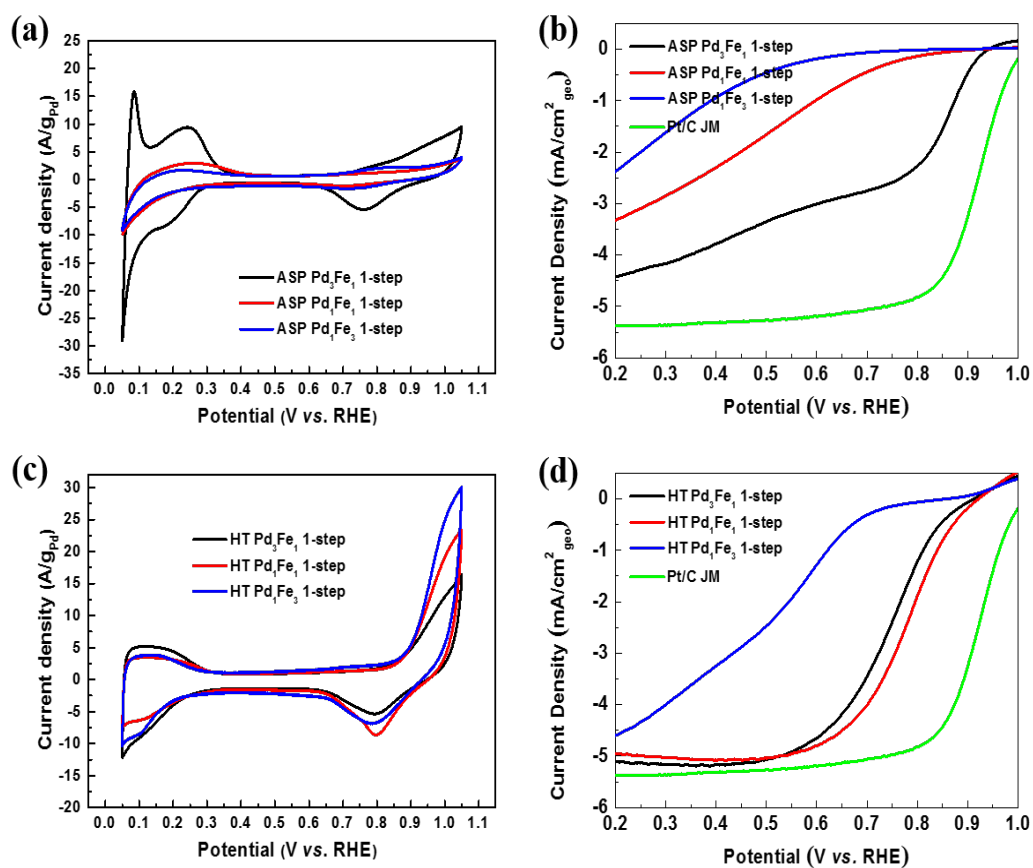


**Figure 3-29.** Cyclic voltammogram ((a), (c)) and ORR polarization curve ((b), (d)) of ASP and HT  $\text{Pd}_x\text{Fe}_y$  samples prepared by one-step synthesis.

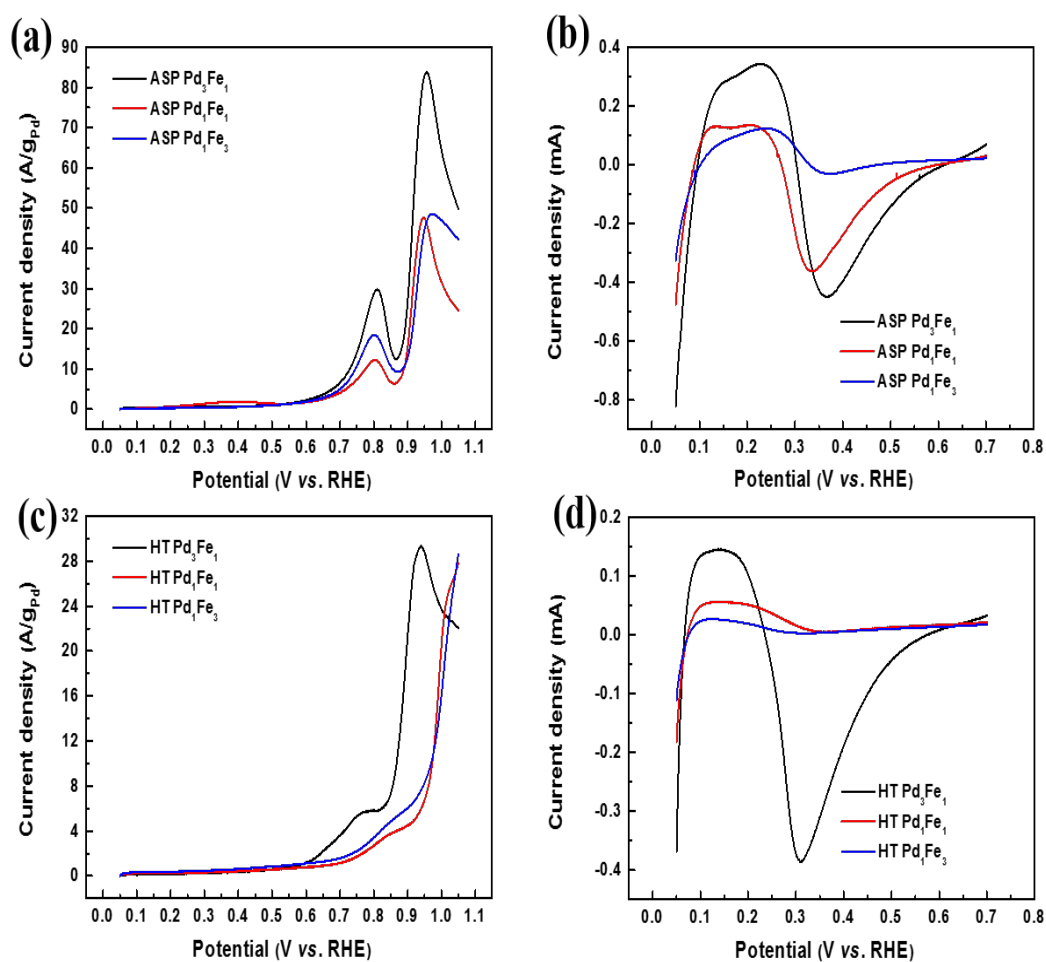


**Figure 3-30.** CO stripping voltammogram ((a), (c)) and  $\text{N}_2\text{O}$  reduction curve ((b), (d)) of ASP and HT  $\text{Pd}_x\text{Fe}_y$  samples prepared by two-step synthesis.



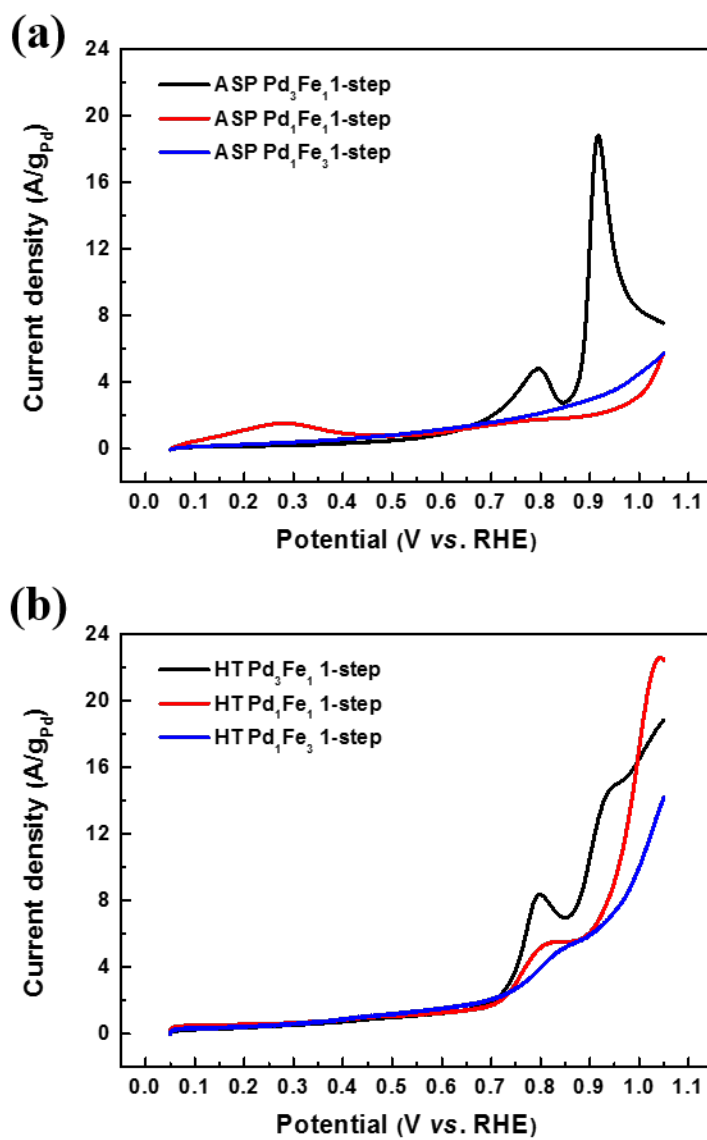


**Figure 3-31.** CO stripping voltammogram of ASP and HT Pd<sub>x</sub>Fe<sub>y</sub> samples prepared by one-step synthesis.

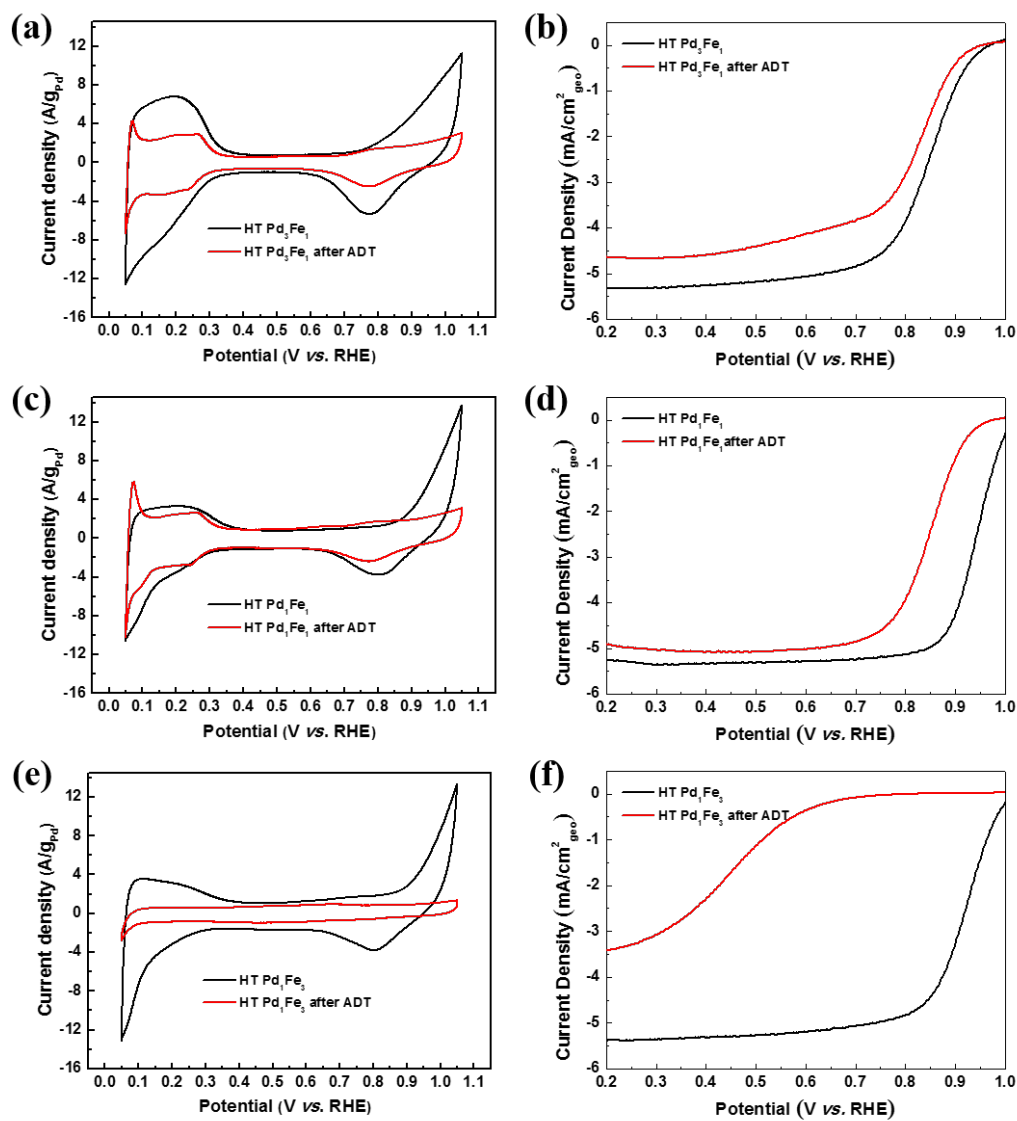


**Figure 3-32.** Cyclic voltammogram ((a), (c)) and ORR polarization curve ((b), (d)) of ASP and HT Pd<sub>x</sub>Fe<sub>y</sub> samples prepared by two-step synthesis after ADT.

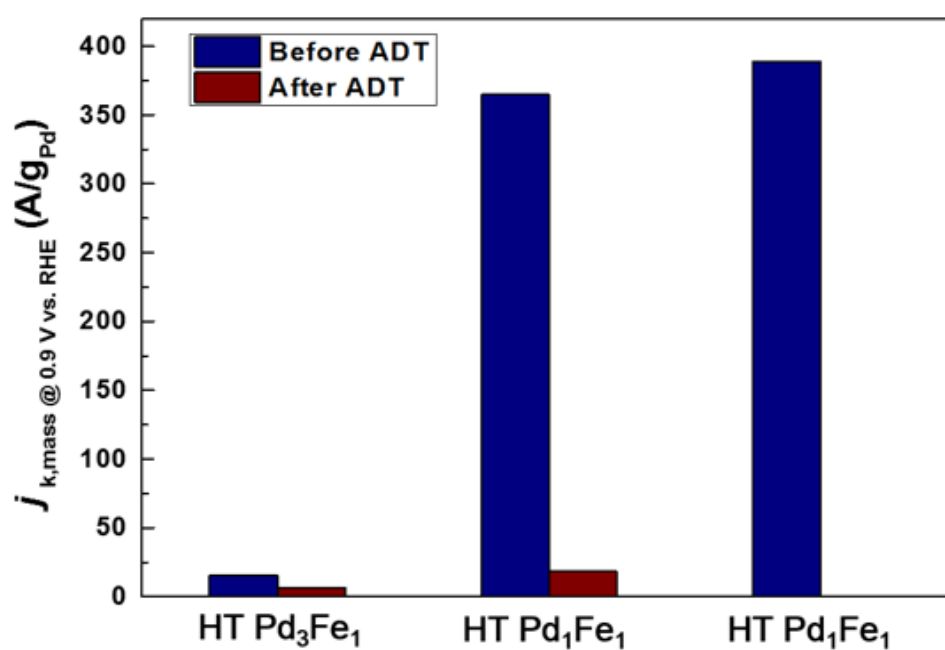


**Figure 3-33.** Pd mass normalized ORR activity as 0.9 V vs. RHE of HT Pd<sub>x</sub>Fe<sub>y</sub> NPs prepared by two-step synthesis before and after ADT.



Sample	M-M	N	$\sigma^2$	$\Delta E$ (eV)	R ( $\text{\AA}$ )	R-factor (%)
HT Pd <sub>3</sub> Fe <sub>1</sub>	Pd-Pd	8.1	0.0066 (3)	-1.64 (59)	2.728 (5)	0.17
	Pd-Fe	1.4	0.0076 (22)	-6.39 (678)	2.626 (51)	
HT Pd <sub>1</sub> Fe <sub>1</sub>	Pd-Pd	7.6	0.0065 (3)	0.47 (52)	2.724 (4)	0.14
	Pd-Fe	2.5	0.0085 (12)	-1.54 (353)	2.644 (28)	
HT Pd <sub>1</sub> Fe <sub>3</sub>	Pd-Pd	5.2	0.0059 (1)	-0.27 (30)	2.721 (2)	0.06
	Pd-Fe	5.4	0.0141 (4)	-2.49 (104)	2.642 (9)	

**Table 3-3.** EXAFS fitting data of ASP and HT Pd<sub>x</sub>Fe<sub>y</sub> samples by two-step synthesis.

Sample	Pd <sup>0</sup>		Pd <sup>2+</sup>		Pd <sup>4+</sup>	
	Peak (eV)	Area ratio (%)	Peak (eV)	Area ratio (%)	Peak (eV)	Area ratio (%)
ASP Pd <sub>3</sub> Fe <sub>1</sub>	336.22	0.736825774	337.2	0.17472299	338.41	0.088451237
ASP Pd <sub>1</sub> Fe <sub>1</sub>	336.2	0.726852521	337.15	0.186966765	338.55	0.086180714
ASP Pd <sub>1</sub> Fe <sub>3</sub>	336.25	0.719931775	337.43	0.160038985	338.85	0.120029239
HT Pd <sub>3</sub> Fe <sub>1</sub>	336.45	0.822200809	337.65	0.122880688	338.78	0.054918504
HT Pd <sub>1</sub> Fe <sub>1</sub>	336.62	0.825850037	337.83	0.104489978	338.79	0.069659985
HT Pd <sub>1</sub> Fe <sub>3</sub>	336.57	0.79097757	337.89	0.139348287	338.88	0.069674143

**Table 3-4.** XPS Pd 3d deconvolution data of ASP and HT Pd<sub>x</sub>Fe<sub>y</sub> samples by two-step synthesis.

### **3.3. Polymer Electrolyte Membrane Fuel Cell with Multiscale Nafion membrane**

Published in doctorate thesis and reedited

(Sang Moon Kim, 2015, Multiscale Design and Fabrication of Polymeric

Architectures for Wettability Control and Fuel Cell Applications, Seoul National University)

#### **3.3.1. Achieving complex and multiscale structures via multiplex lithography**

The main features of multiplex lithography are illustrated in Figure 3-35. Soft lithography typically yields single-scale structures from a one-step curing process with mother moulds (Figure 3-35 (a)), whereas a multiscale perspective reveals complex three-dimensional architectures from various soft polymers, containing independent nanopatterns into each level of hierarchical surface via multiplex lithography. Note that vertical and parallel nanolines are clearly placed on the different levels of architectures (blue and red colours, respectively), together with nanodots (green colour), which integrates designed nanoscale patterns onto the hierarchical complex microstructures as shown in Figure 3-35 (b). In the experiments, this unique structural hierarchy is oriented from the scavenging effect of infiltrated oxygen near a highly permeable polydimethyl siloxane (PDMS) blanket, with a thin layer or “gray zone” that contains the infiltrated oxygen and inhibits radical-induced polymerizations (93), where the layer enables viscoelastic

and multiplex deformations of the structures to form multiscale structures by performing secondary/tertiary treatment on the surfaces (Figure 3-35 (c)). Experimental monitoring of the relative peak heights of Fourier-transform infrared (FT-IR) spectra onto the insufficiently cured polymeric surface near the gray zone shows a gradual, multiplex curing of the top surface of polyurethane acrylate (PUA) under a time-dependent UV-curing reaction (Figure 3-35 (d)) (94). According to the experiments we performed, the PUA resins with a low conversion ratio or “curing contrast ( $c$ )” (i.e., 30-55 %) typically remain with many cross-linkable bonds on soft, viscoelastic surfaces of PUA bricks that are deformed in strict guidance, and then stacked in serial LEGO®-like integrating procedures. For an easy understanding of our strategies with the multiple curing steps, we hypothesize that two curing speeds are possible based on the permeability differences in the boundary conditions: i) slow curing under a highly permeable blanket (PDMS, dashed red line) and ii) rapid curing under a blanket with low permeability (PUA, dashed black line), where close correspondence in slope is represented with the same colour (arrows and dashed lines) (Figure 3-35 (e)). A detailed explanation of this hypothesis with multiplex curing steps is further provided below, consisting of the preparation of MCBs ( $\alpha$  and  $\alpha'$ ), a confined deformation via imprinting ( $\beta'$ ) and a monolithic bonding of each brick ( $\beta$  and  $\gamma$ ).

The first step of multiplex lithography is the generation of a MCB by slightly curing the PUA resin between two permeable PDMS layers that are constructed in



a sandwich-like assembly (Figure 3-36 (a)). Here, an overlapped oxygen-inhibition layer (OIL) within the confined, thin PUA resin was readily achieved through simple squeezing due to the hydrophobicity differences near the interfaces (i.e., the contact angles of PUA and PDMS are approximately  $88^\circ$  and  $104^\circ$ , respectively). After an initial short UV treatment as a 1<sup>st</sup> curing, the confined, partially cured PUA layer was spontaneously divided into two parts during their disassembly, readily generating a partially cured PUA brick with low curing contrast (red dashed box in Figure 3-36 (a) and (b)). Then, the uncured PUA brick experiences a spontaneous dewetting that produces many individual micro ebb tides of viscoelastic resin on an array of exposed PDMS pillars (purple arrows). This is mainly due to the fact that the uncured PUA resin exhibited quietly low affinity for the exposed hydrophobic PDMS surface (top surface of the pillars of bottom PDMS mould). Thus, the viscoelastic micro ebb tides (the movement of insufficiently cured PUA droplets) were slowly headed for a neighboring PUA surface to avoid the contact with the PDMS surface (Figure 3-36 (b)). We discussed that three unique boundary conditions were possible in accordance with the oxygen concentrations ( $\#1 < \#2 < \#3$ ) that affect and reduce the curing speed of PUA resins ( $\#1 > \#2 > \#3$ ) within the sandwich-like moulding setup; thus the micro ebb tides resulted in a dramatic decrease in the curing contrast ( $c: \alpha \rightarrow \alpha'$ ) at the top surface of MCB by enabling the viscoelastic coating because the each droplet was initially placed at overlapped OIL regions ( $\#3$ ) such that infiltrated oxygen could strongly inhibit the UV reaction

( $c \sim \alpha'$ ) than that of other regions.

The microscopic images in Figure 3-36 (b) are monitoring the events for the micro ebb tides that act as an automatic viscoelastic coating on a neighboring PUA brick. As an initial step, a long wave occurs rapidly by the surface tension of the uncured PUA resin (green arrows). Then, the individual viscoelastic droplet starts to move as a result of affinity mismatching (purple arrows). This type of constant, slow dewetting lasted for several minutes ( $> 1$  min), where similar dewetting is also detectable on the disintegrated flat PDMS layer. After dewetting, a self-supporting polymer brick with a viscoelastic coating on the top surface was obtained by removing the underlying PDMS mould from the assembly. Independent of the pattern shapes and dimensions, various MCBs can be achieved through the process presented. In addition, the brick is sufficiently robust to be handled with tweezers without cracking or tearing due to the connected frameworks (#1) of the highly cured PUA brick, which possess a relatively high elastic modulus ( $\sim 320$  MPa) (Figure 3-36 (c)). Figure 3-36 (c) is a representative digital image of the MCB with 150- $\mu\text{m}$  apertures over a large area of up to 2 inches, which is used in a LEGO<sup>®</sup>-like multiplex process as a basic deformable brick.

Next, we vertically stacked the obtained MCB on a holey polymeric substrate under a surface selection ( $\alpha$  and  $\alpha'$ ) to elucidate the role of deformation of the viscoelastic coating on the MCB (Figure 3-37 (a)). According to the calculation based on the relative peak height of the FT-IR spectra with respect to the uncured

resin, the curing contrast of the top surface of MCB showed a low value ( $\alpha' \sim 45\%$ ) due to the coating with viscoelastic micro ebb tides, whereas the bottom surface of MCB had a relatively high curing contrast ( $\alpha \sim 55\%$ ). In the stacking experiments, the both surfaces ( $\alpha$  and  $\alpha'$ ) of MCB ensured stable connecting results, although the underlying holey bottom substrate (PUA) was prepared with a relatively high curing contrast ( $c \sim 60\%$ ) for good pattern fidelity at the submicron scales as well as high-resolution replications of the hierarchical polymeric structures. The scanning electron microscopy (SEM) images in Figure 3-37 (b) show the clearly attached 20- $\mu\text{m}$  holes on the underlying substrate with an array of 800-nm patterns. To match the cross-sectional profile with the calculated curing contrast, a focused ion beam (FIB) study was performed by revealing the connected interface under the stacked MCB at a fixed ratio with a diameter of 25 ( $= d_{\text{Top}}/d_{\text{Bottom}}$ ,  $d_{\text{Top}} = 20, 100\ \mu\text{m}$ ,  $d_{\text{Bottom}} = 0.8, 4\ \mu\text{m}$ , respectively), which guaranteed the proper shape of the hierarchical structure after the monolithic stacking of each MCB. When a surface with a curing contrast of  $\alpha$  ( $d_{\text{Top}} = 20\ \mu\text{m}$ ) is selected and attached to the pattern with nanoholes ( $d_{\text{Bottom}} = 0.8\ \mu\text{m}$ ), these underlying nanoholes remain clearly unfilled under a bonding interface after the monolithic integration (we termed this as “surficial bonding”) (Figure 3-37 (c)). However, for a stacking with the viscoelastic coating of  $\alpha'$  ( $d_{\text{Top}} = 100\ \mu\text{m}$ ), even the microholes ( $d_{\text{Bottom}} = 4\ \mu\text{m}$ ) were completely filled with the resin (we termed this as “structural interconnection”), suggesting that the structural deformation from fluidity of the viscoelastic coating was sufficiently high

at the interface (Figure 3-37 (d)). The existence of top surface of MCB with low curing contrast of  $\alpha'$  is surely important to perform the multiplex lithography and we utilized the layer for nanopatterns via a secondary nano-moulding process. We note that the bottom surface with curing contrast of  $\alpha$  is also possible to be connected with the underlying nanopatterns; thus various combinations with bricks were demonstrated to form two-level hierarchical structures via the stacking strategies. The replication results showed a facile generation of two-level hierarchical structures from various polymers by combining two bricks under a facile manner as shown in the Figure 3-37 (e)-(g), which directly enables the rapid prototyping of multilevel hierarchical architectures through this simple vertical stacking method.

The significant advantage in the aforementioned monolithic stacking using MCB over previous strategies for polymeric hierarchical structures (95-98) is that the multilevel hierarchical structures can be fabricated rapidly ( $< 10$  min) over a large area simply by carrying out a replication from the integrated bricks using various polymers, such as PUA, Norland Optical Adhesive (NOA), perfluoropolyether (PFPE) and even PDMS. This monolithic integration concept was further verified by stacking various shapes of bricks under combinations of the top and bottom layers for a generation of successful multilevel architectures of up to four levels (Figure 3-38 (a)). By monolithically stacking the four bricks, which constituted a series of increasing holes in sizes (150 nm/8  $\mu$ m/165  $\mu$ m/500  $\mu$ m), and executing

facile UV-replicating processes, a four-level hierarchical architecture was precisely formed with or without the alignment of the MCBs (Figure 3-38 (b)). When the ratio of the hole diameter in the MCBs was sufficiently larger than 15, a hierarchical structure was easily generated from the bonded bricks without the alignment of the MCBs. However, for the same order of magnitude ( $d_{\text{Top}}/d_{\text{Bottom}} < 15$ ) of the hole size, pre-designed MCBs with the same pitch as the array of pattern were required to avoid mechanical fractures or defects in the hierarchical replica. The four-level architecture shown in the Figure 3-38 (b) was formed based on these design rules, providing a key idea for indeed multiplex lithography under a utilization of viscoelastic deformation of the top surface with a low curing contrast ( $\alpha'$ ) and multiple exposure of UV to generate independent nano patterns on every projection on the hierarchical multilevel structures.

By performing the multiplex lithography that utilizes the concept of both the LEGO<sup>®</sup>-like vertical stacking and the deformation of the viscoelastic coating layer in a MCB, we can build a designed multiscale structure of only polymers with using simple moulding processes, which provides a new protocol for fabricating various types of multiscale devices and systems. The schematic illustration in Figure 3-39 (a) depicts a LEGO<sup>®</sup>-like multiplex process that employs the aforementioned two independent curing paths (slow and fast curing under the different permeability) related to sequential imprinting and bonding. The brick has two different curing contrasts on both sides ( $\alpha$  and  $\alpha'$ ); monolithic integration is performed on the bottom

of the brick with the curing contrast of  $\alpha$  ( $c \sim 55\%$ ) by placing the brick onto a pre-patterned PUA with a curing contrast of  $\beta$  ( $c \sim 60\%$ ). The SEM image in Figure 3-39 (b) shows 800-nm-patterned PUA holes (depth: 800 nm) as the underlying substrate for this monolithic integration. Then, both bricks with 20- $\mu\text{m}$  holes (thickness of 20  $\mu\text{m}$ , Figure 3-39 (c)) and permeable mould with nanopatterns (800-nm dots) were vertically placed and pressed to deform the top viscoelastic layer ( $\alpha'$ ) for confined nanostructures (imprinting), whereas the bottom layer ( $\alpha$ ) bonded to the underlying patterns (bonding) during the second UV exposure (Figure 3-39 (d)). According to the hypothesis, the PUA brick has low permeability, thus the underlying bonding follows the rapid curing regime. However, the same exposure, when repeated, leads to small, stepwise increases in the curing contrast of up to 60 % for the imprinting of top surface under a permeable mould with 800-nm pillars, which ensures a sufficient degree of curing for the preparation of the next bonding step (iv) during the third exposure. By repeating the multiplex stacking (iv, v, vi) with a brick with larger holes ( $\sim 500\ \mu\text{m}$  in diameter), a third layer was successfully integrated (Figure 3-39 (e)) onto the imprinted and deformed top surface of MCB, where 800-nm holes are clearly observed on every projected surface. As a final step, we performed a replica moulding with various pre-polymers to robustly form a tri-level multiscale architecture from the fully cured, stacked assembly ( $\gg 60\%$ , vii) as shown in Figure 3-39 (f). The multiplex curing and stacking is rationally performed by controlling the curing contrast with permeability, together with the

micro ebb tides for the effective reduction of the curing contrast on the top surface of the brick for the next deformation process, which would be a unique strategy as a guide for multiscale, hierarchical engineering with polymers through this simple moulding approach.

### **3.3.2. Physical and electrochemical characterization**

Before the application of multiscale Nafion membrane on PEMFC, the analysis of mechanical properties of the membrane was conducted. (Figure 3-40) At first, the mechanical strengths of multiscale Nafion membrane and flat one were compared. The results showed that multiscale Nafion membrane has only ~12 % lower tensile strength than the Nafion 212 membrane (~31.11 MPa) but ~16 % higher maximum tensile strength than the Nafion 211 membrane (~23.55 MPa). Elongation before break for our multiscale case is in the same range as that of 50  $\mu\text{m}$  Nafion 212. (Figure 3-40 (a)). It is interpreted that these results support the idea of using Nafion membrane with multiscale structure which not only provides a lower proton resistance, but also ensures the mechanical robustness. In addition, the simulation study was conducted to mimic the situation when applying the force perpendicular to the membrane surface to examine whether the membrane could withstand during catalyst spraying process. The simulation results showed that the multiscale Nafion membrane (thickness of ~10  $\mu\text{m}$  in certain areas) yields almost the same level of

stress distribution as that of Nafion 212 while the case of Nafion 211 showed high stress concentration region near side grips. This result supports the robustness of our multiscale membrane.

For an evaluation of multiscale engineering that utilizes the advantages from each micro/nanoscale structure simultaneously, we constructed a multiscale PEMFC by incorporating multiscale architectures into a Nafion membrane that selectively transports protons ( $H^+$ ) from the anode to the cathode in the PEMFC (Figure 3-41 (a)). To enhance the device performance, the development of a high-performance electrode materials (99-103), membrane (104, 105) and novel structure for a membrane electrode assembly (MEA) (106, 107) have been extensively studied over several decades. Of these advancements, approaches for reducing the resistance to high conduction in a Nafion membrane has been explored, including lowering the thickness of the membrane (108). However, reducing the Nafion thickness in an MEA remains challenging and impractical due to the low mechanical properties of the thin Nafion membrane. Here, we demonstrate a first trial toward multiscale engineering on a Nafion membrane (Figure 3-41 (a), (b)). Remarkably, the multiscale Nafion membrane resulted from this approach offers two distinct structural and physicochemical advantages for enhanced performance from the multi hierarchy with complex patterns as well as a high robustness for the handling of weak membranes by a multiscale leveling: i) an outstandingly elevated surface area for augmenting the triple phase boundaries (TPBs), which are areas for



electrochemical reactions, and ii) a reduced effective thickness that increases proton conductivity due to the short transport path. Figure 3-41 (c) shows enhanced proton conductivity in accordance with the different dimension of patterns on the Nafion membrane. This is mainly due to the fact that the proton conductivity is inversely proportional to the average thickness, which is rationally reduced after the multiscale imprinting from the height of the carved patterns. The trilevel architectures (multiscale Nafion membrane) ensured the best conductivity through the hierarchical leveling. Structurally, the multiscale Nafion membrane consists of three different thicknesses ( $L_1 > L_2 > L_3$ ), where  $L_1$  is the original thickness of the membrane ( $\sim 50 \mu\text{m}$ ) (Figure 3-41 (a)). As a thin Nafion membrane is often fragile during the catalyst coating process,  $L_1$  provides a clear geometrical supporting from the hierarchical leveling of relatively thin areas with a thickness of  $L_2$  ( $\sim 30 \mu\text{m}$ ) and  $L_3$  ( $\sim 10 \mu\text{m}$ ) (109). In this manner, both regions ( $L_2, L_3$ ) directly affected the reduced membrane resistance, leading to efficiently enhanced performance because the membrane resistance follows Ohm's law, whereby resistance is proportional to the distance between two points of a conductor.

Considering these structural advantages from the multiscale engineering, we constructed PEMFCs by spraying Pt/C catalysts onto both sides of the membrane (Pt loading:  $0.12 \text{ mg cm}^{-2}$ ). When operating the MEA with the multiscale membrane in a fully humidified condition of  $\text{H}_2/\text{O}_2$  (or  $\text{H}_2/\text{air}$ ), this MEA exhibited outstanding performance compared to a conventional one as shown in Figure 3-41 (d) and (e).

The MEA with a multiscale membrane exhibited superior performance of up to  $2.026 \text{ W/cm}^2$  within the conditions of the U.S. Department of Energy (DOE) (106, 110). The effective performance increases in the MEA with a multiscale membrane are maintained regardless of the outlet pressure. In particular, the maximum power density increment of  $\sim 42.3 \%$  was achieved in the case of  $\text{H}_2/\text{O}_2$  conditions under ambient pressure (Figure 3-41 (d)). This challenging enhancement is also partially due to the multiscale roughness, which enlarges the surface area of the Nafion membrane by as much as 1.96-fold compared to that of the conventional membrane. Both electrochemical impedance spectroscopy (EIS) and cyclic voltammetry (CV) (111) were used to further verify the effectiveness of this multiscale engineering, confirming the structural strategy of multiscale MEAs (Table 3-5, Figure 3-42). In addition, detailed values of the enhanced electrochemical active surface area (EAS) and Pt utilization are presented in Table 3-6.

In Addition, to figure out the robustness of MEA with multiscale membrane, accelerated durability test (ADT) was conducted using CV method in the potential range of 0.05 to 1.20 V vs. RHE and  $100 \text{ mV s}^{-1}$  at RT for 5000 cycles with fully humidified  $\text{H}_2/\text{N}_2$  gas supplied to anode and cathode, respectively. After ADT test, the performance of MEAs is decreased by  $\sim 20\text{-}30 \%$  for maximum power densities due to degradation of Pt electrocatalyst and increased interfacial resistance between Nafion membrane and cathode catalyst layer. (Figure 3-43,) To assure these, we compared ECSAs of MEAs before and after ADT test (Figure 3-44, 3-45). During

ADT test, it is proved that due to the dissolution of Pt electrocatalyst and increased interfacial resistance between MEA components, the ECSAs decreased by ~37 % before the test. However, the performance of MEA with multiscale membrane is much higher than conventional MEA by ~20 %. Hydrogen crossover rate of membranes was measured by using linear sweep voltammetry in the range from 0 to 0.7 V. vs. RHE and the moles of permeated hydrogen gas was calculated by Nernst equation. (Figure 3-46) It is concluded that MEA with multiscale membrane exhibited higher hydrogen crossover rate compared to MEA with Nafion 212, but lower than that of Nafion 211, which means that decreased membrane of multiscale membrane make hydrogen gas crossover easier than before. However, from the ADT test data before mentioned, it is proved that decreased membrane thickness which triggers higher hydrogen gas crossover doesn't break down the single cell after long term operation. Therefore, this multiscale approach for improving MEA performance will contribute the commercialization of PEMFC in the future without any failures related to membrane structure.

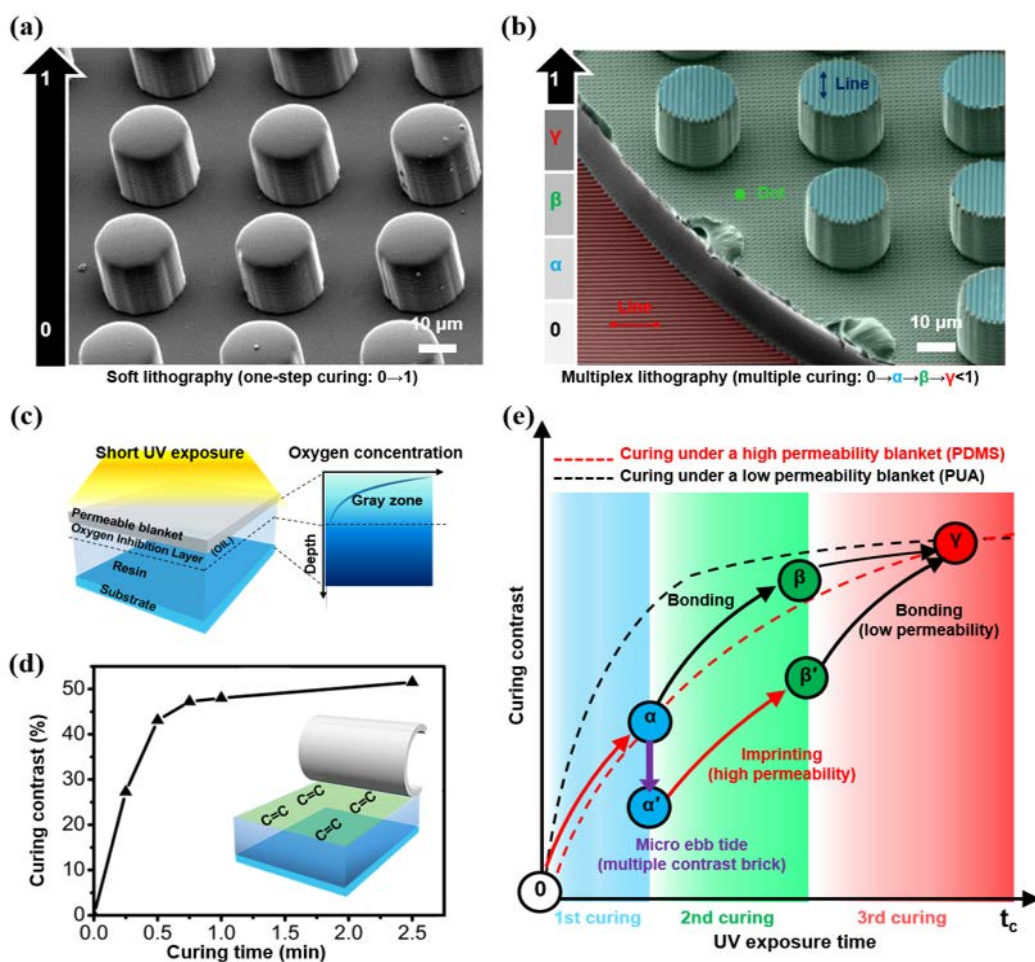


**Figure 3-35.** (a) Single-scale structures from soft lithography. (b) Multiscale perspective of a complex, hierarchical architecture from multiplex lithography. The architecture has independent nanopatterns (dots and lines) on each flat surface. (c) Illustration of a ‘gray zone’ with infiltrated oxygen from a permeable PDMS blanket. (d) Calculated curing contrast after short time-dependent UV exposure. (e) Hypothesis for multiple curing with UV to form complex hierarchical architectures from simple molding processes.

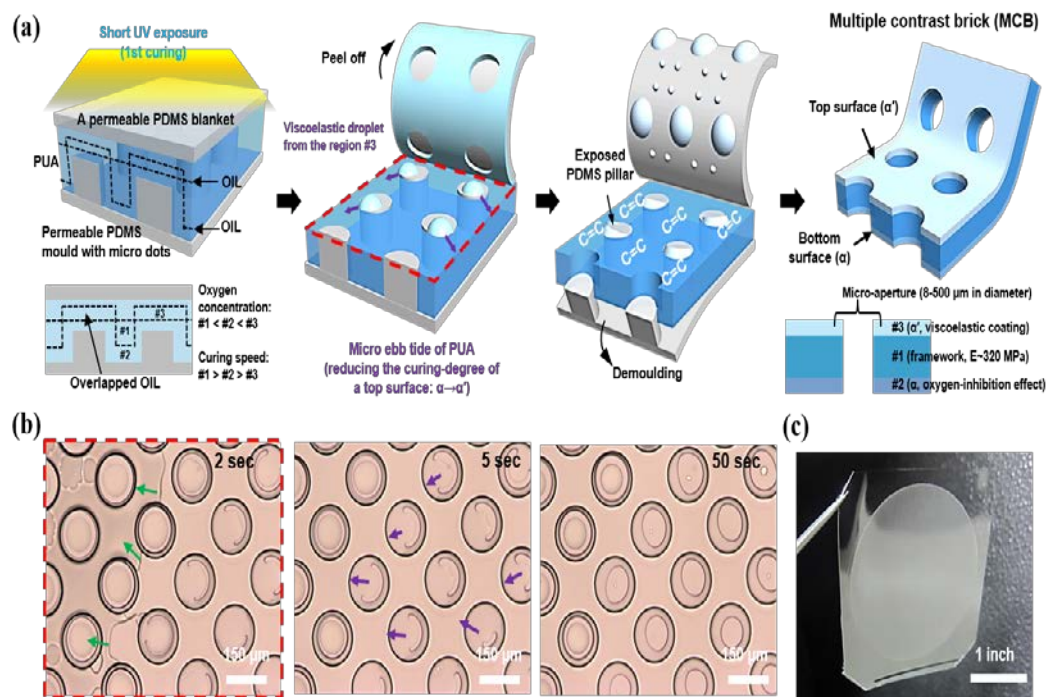


**Figure 3-36.** Micro ebb tides in partially cured resin for the generation of a multiple contrast brick (MCB). (a) Schematic illustration for the overlapping of OIL and the resulting micro ebb tide after the first UV exposure. The micro ebb tides gradually reduce the curing contrast on the top surface of the brick from  $\alpha$  to  $\alpha'$ . (b) Microscopic images of the real-time monitoring of micro ebb tides. The low affinity of viscoelastic PUA resin to PDMS pillars yields the spontaneous coating of partially cured resin on the top surface of the brick. (c) Digital image of the MCB produced as a unit part for LEGO®-like stacking.

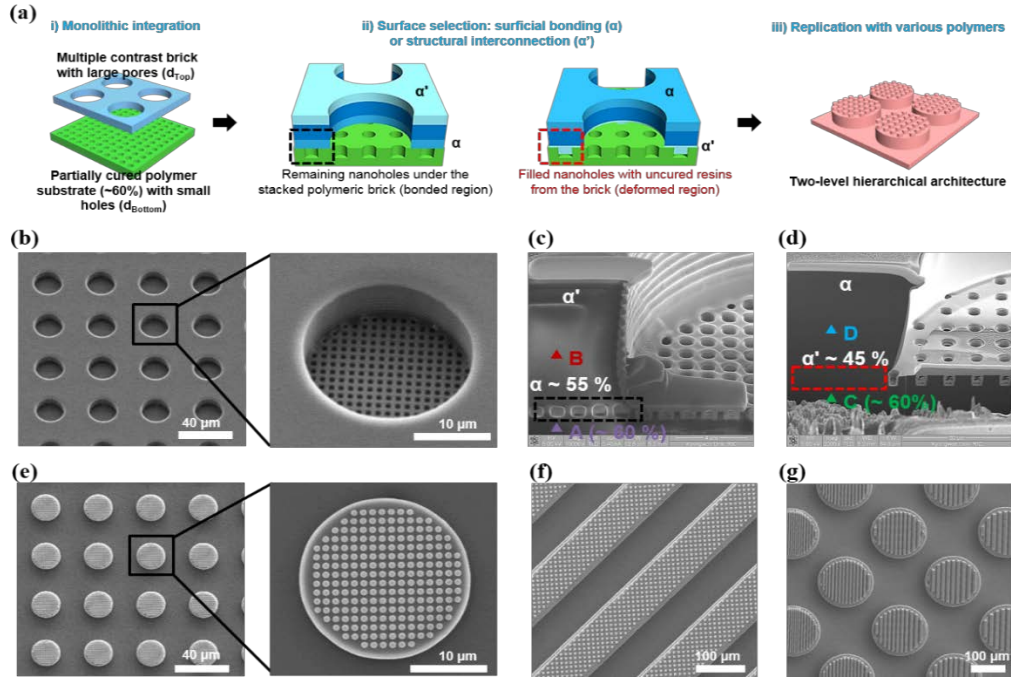


**Figure 3-37.** (a) Schematic illustration for the vertical stacking of MCBs and the connected interfaces under a surface selection between relatively high ( $\alpha$ ) and low ( $\alpha'$ ) curing contrasts of the MCB. (b) SEM images of the integrated MCB (20- $\mu$ m holes) on the underlying substrate (800-nm in diameter). (c), (d) Analysis for the deformability in accordance with the curing contrast under a surface selection. A focused ion beam (FIB) study reveals the differences in the deformability at a fixed ratio with a diameter of 25, where the bottom surface with relatively high curing contrast ( $\alpha \sim 55\%$ ) remained the unfilled nanoholes (c), while a large fluidity of the viscoelastic coating ( $\alpha \sim 45\%$ ) showed a sufficient deformation to fill even microholes (d). (e), (f), (g) SEM images of the replicated two-level hierarchical structures from the stacked bricks.

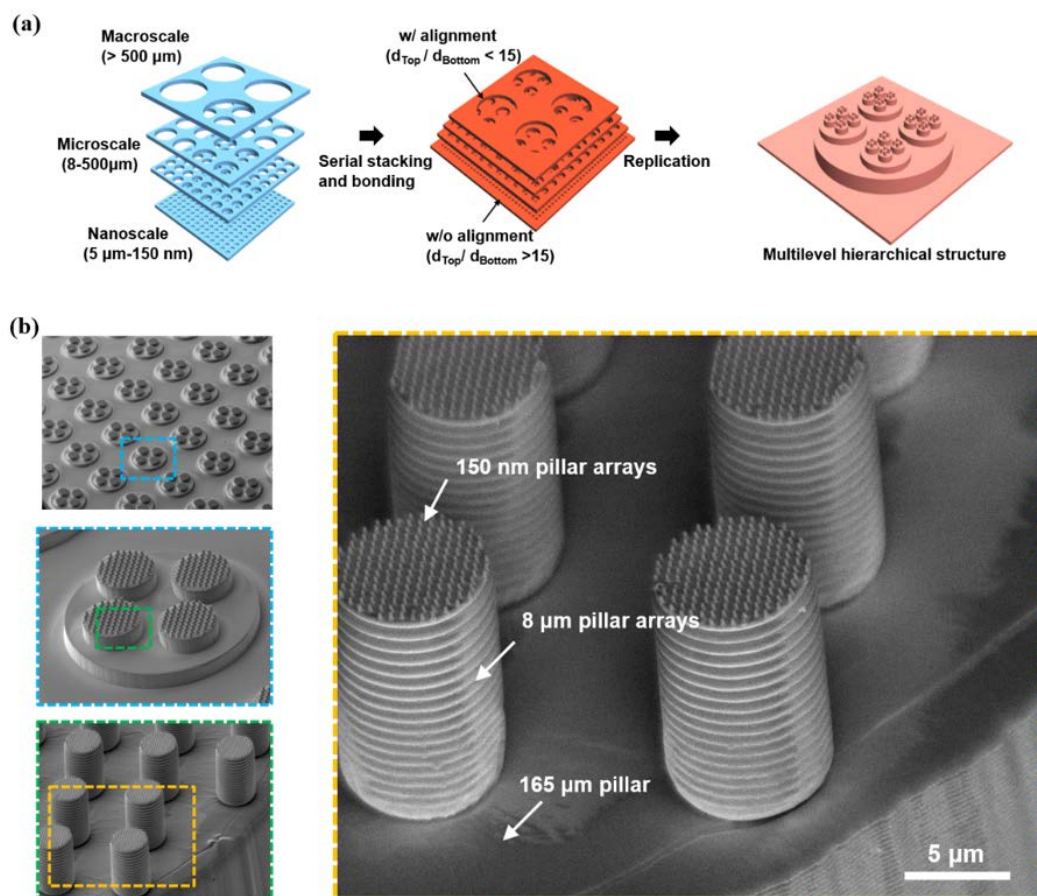


**Figure 3-38.** (a) Schematic illustration for the fabrication of a four-level polymeric architecture via the multi-stacking process with MCBs. (b) Multiscale perspective for the obtained four-level architecture with various pillars of increasing sizes (150 nm/8  $\mu\text{m}$ /165  $\mu\text{m}$ /500  $\mu\text{m}$ ).



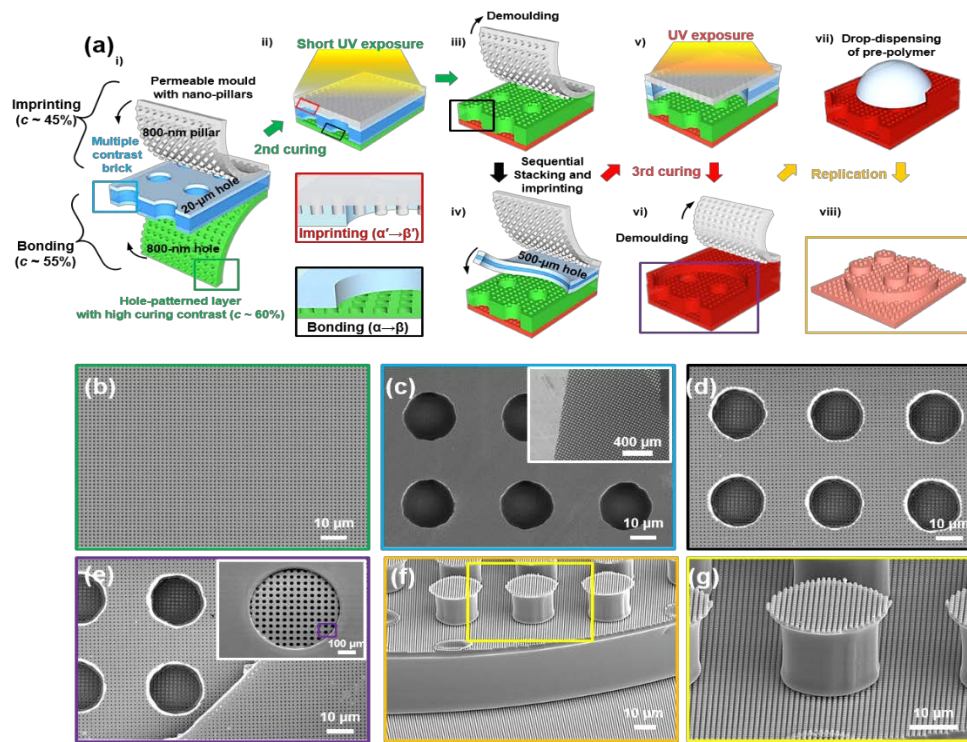


**Figure 3-39.** (a) Schematic illustration of the multiplex lithography. Both imprinting and bonding is achieved with the top and bottom surfaces of the brick ( $\alpha'$  and  $\alpha$ , respectively) to form complex hierarchical architectures. (b), (c), (d), (e), (f), (g) SEM images of the bricks (b, c), monolithic assemblies (d, e) and final architectures after replication (f, g).



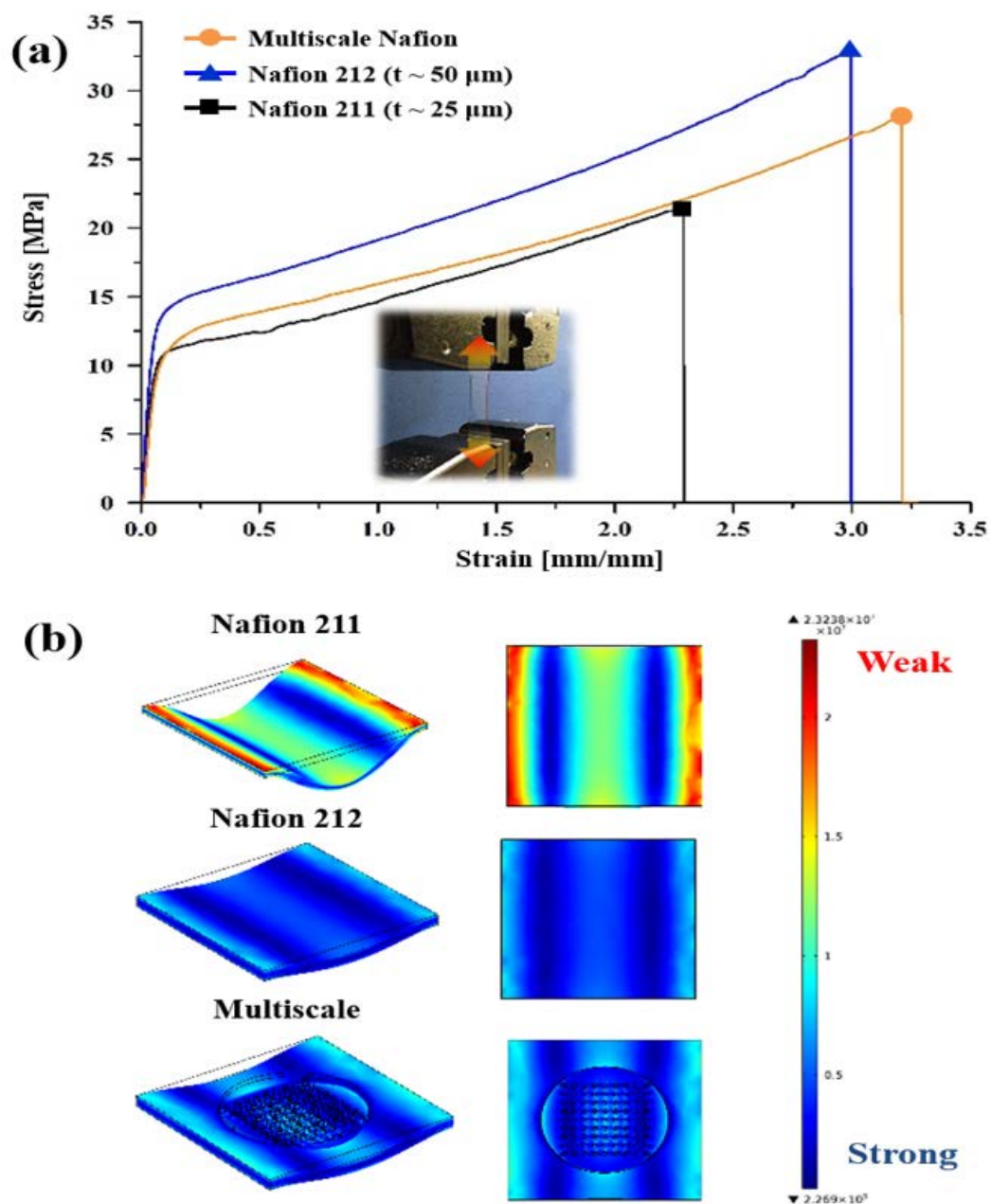


**Figure 3-40.** (a) Tensile strength test of membranes and (b) COMSOL simulation data related to force distribution.

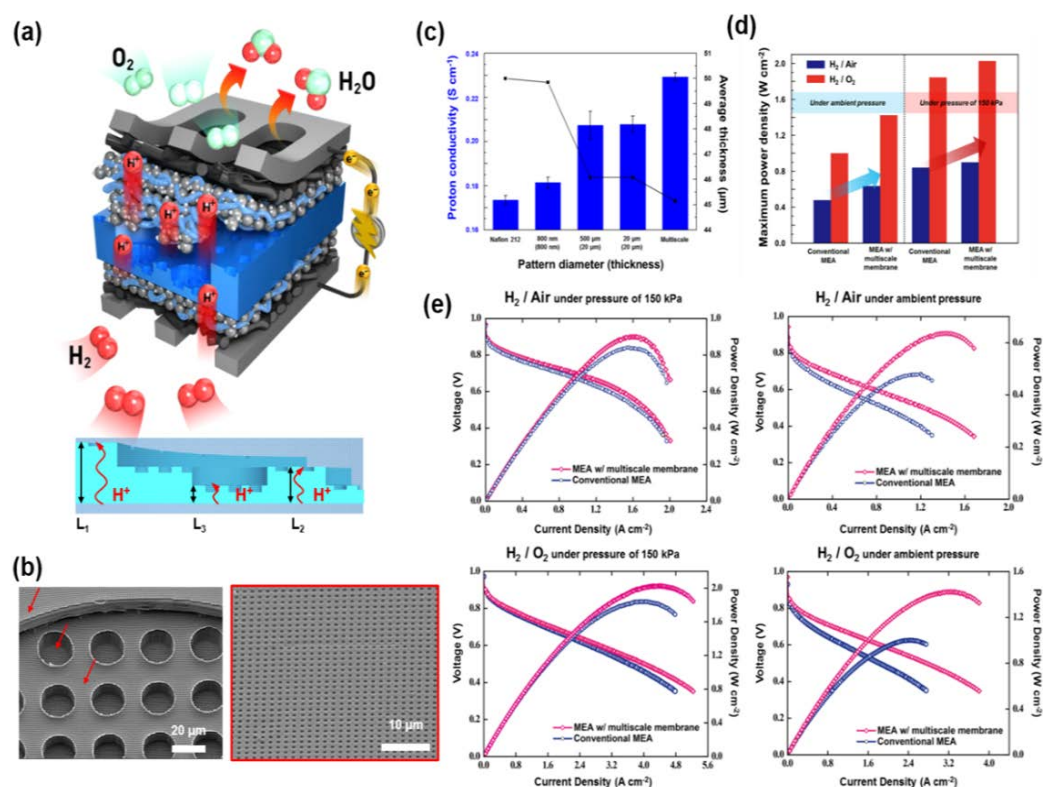


**Figure 3-41.** (a) Schematic illustration of the device operation with multiscale Nafion membrane. (b) SEM images of imprinted multiscale Nafion membrane. (c) Measured proton conductivities of each patterned Nafion membrane. (d) The difference between the maximum power densities of conventional membrane electrode assembly (MEA) and the MEA with a multiscale Nafion membrane under the conditions of  $H_2$ /Air and  $H_2$ / $O_2$  with or without outlet pressure. (e) Measured polarization curves.

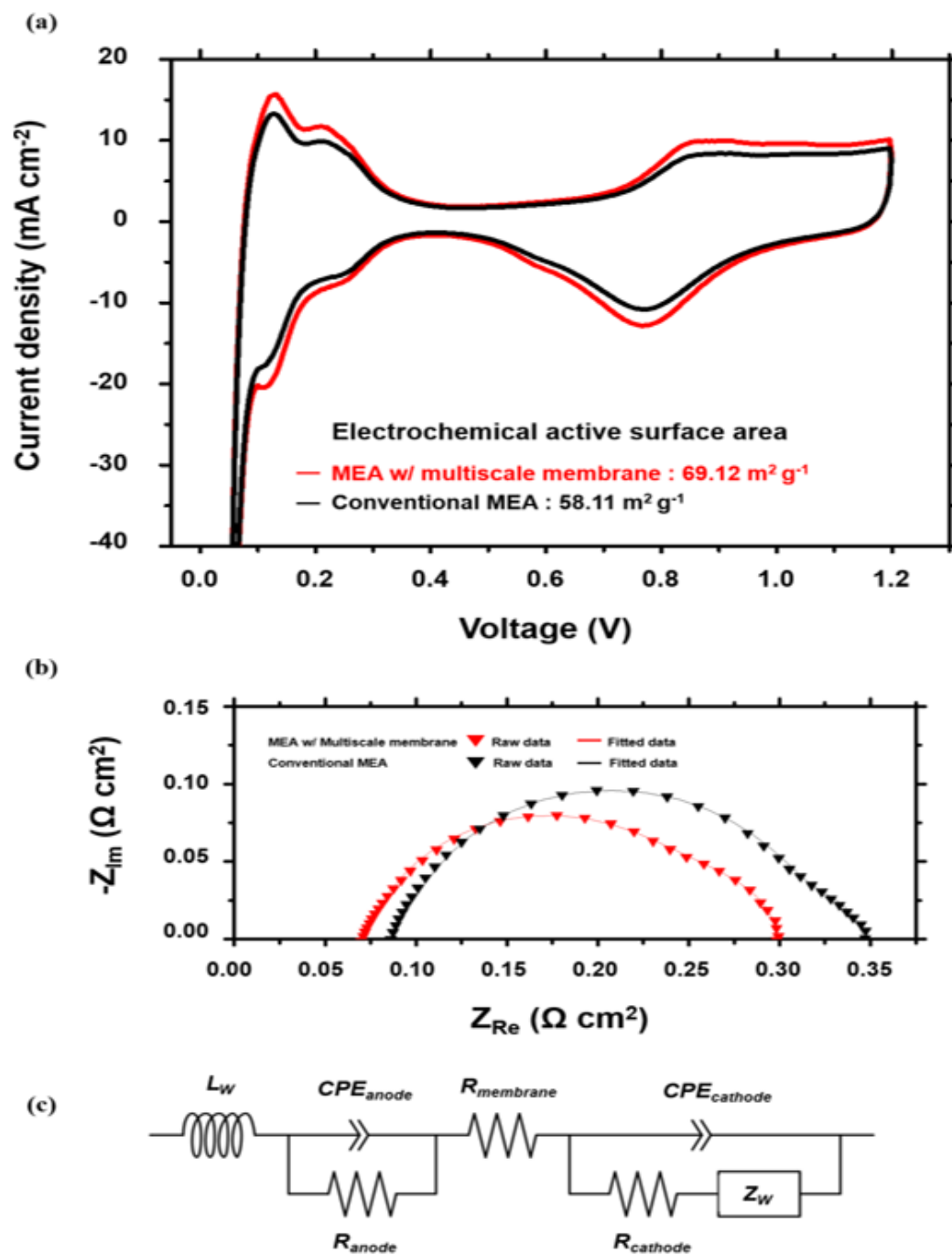


**Figure 3-42.** (a) Cyclic voltammogram (CV), (b) electrochemical impedance spectroscopy (EIS) of MEAs and (c) its equivalent circuit.

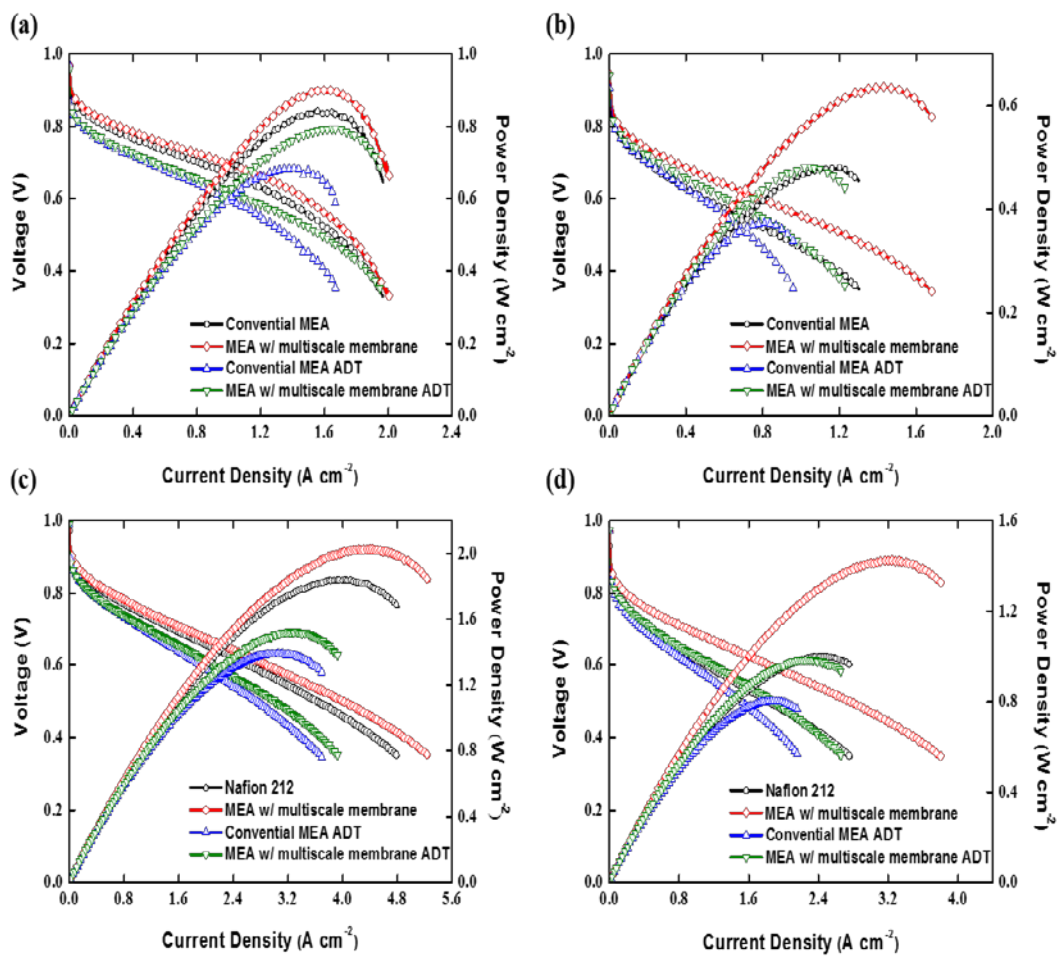


**Figure 3-43.** Polarization curves conventional MEA and the MEA with a multiscale Nafion membrane before and after ADT under the conditions of (a), (b)  $\text{H}_2/\text{Air}$  and (c), (d)  $\text{H}_2/\text{O}_2$  with or without outlet pressure of 150 kPa.

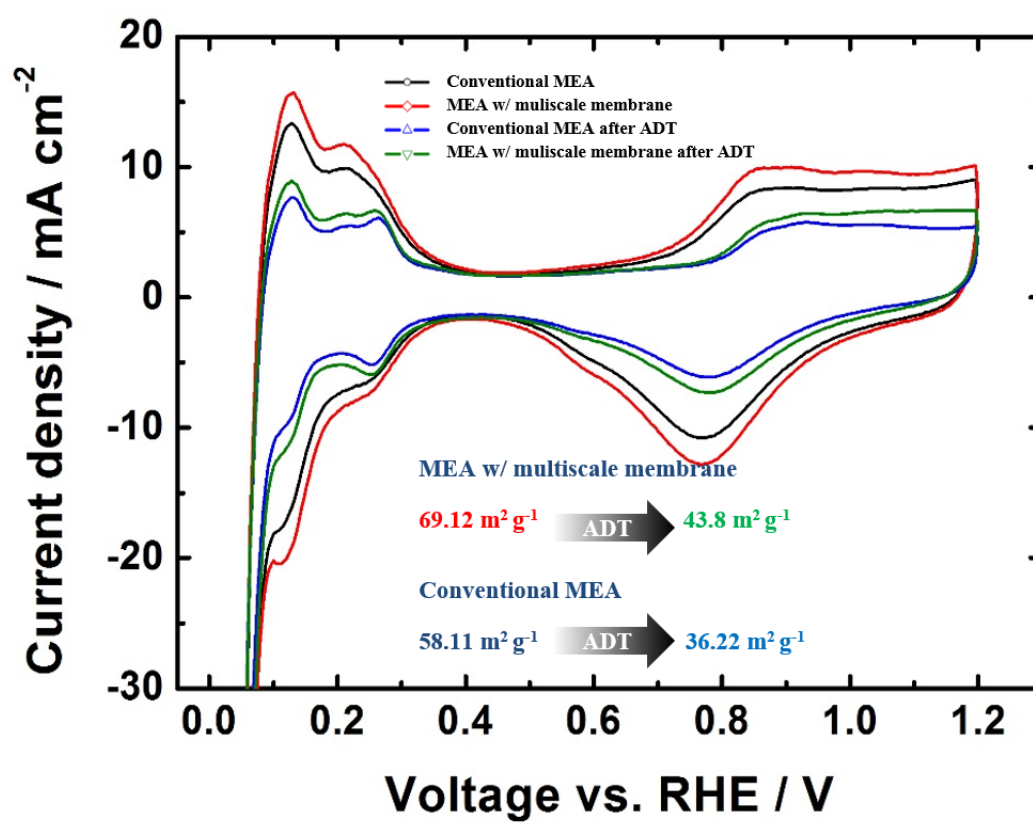
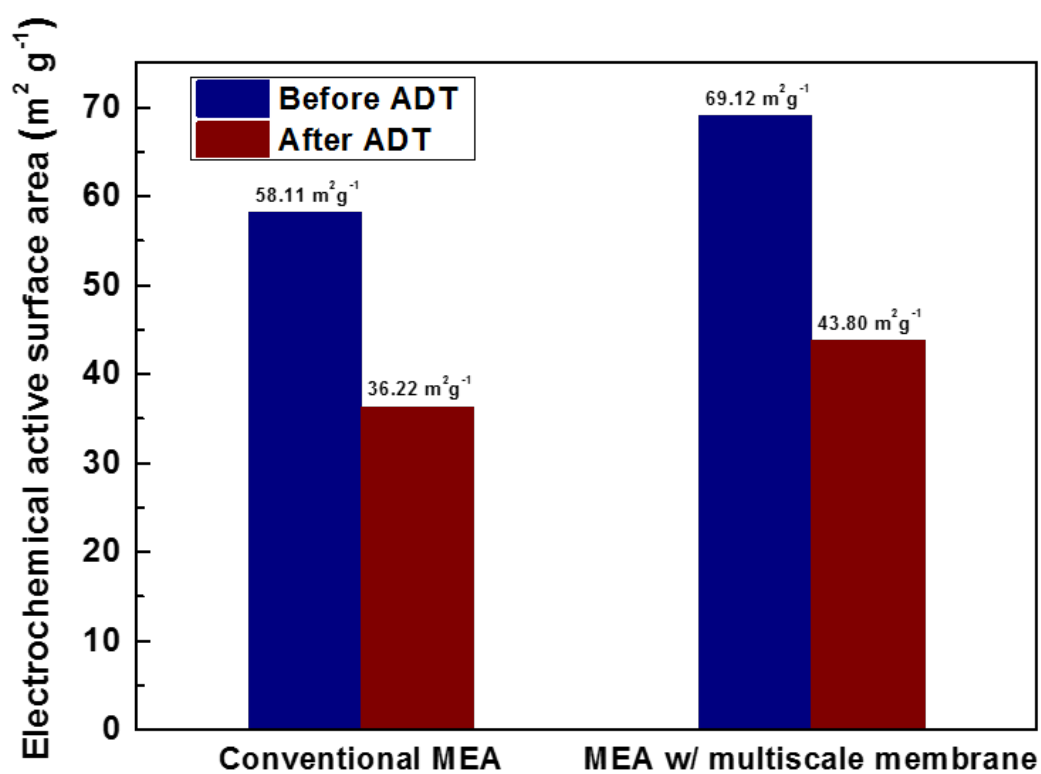
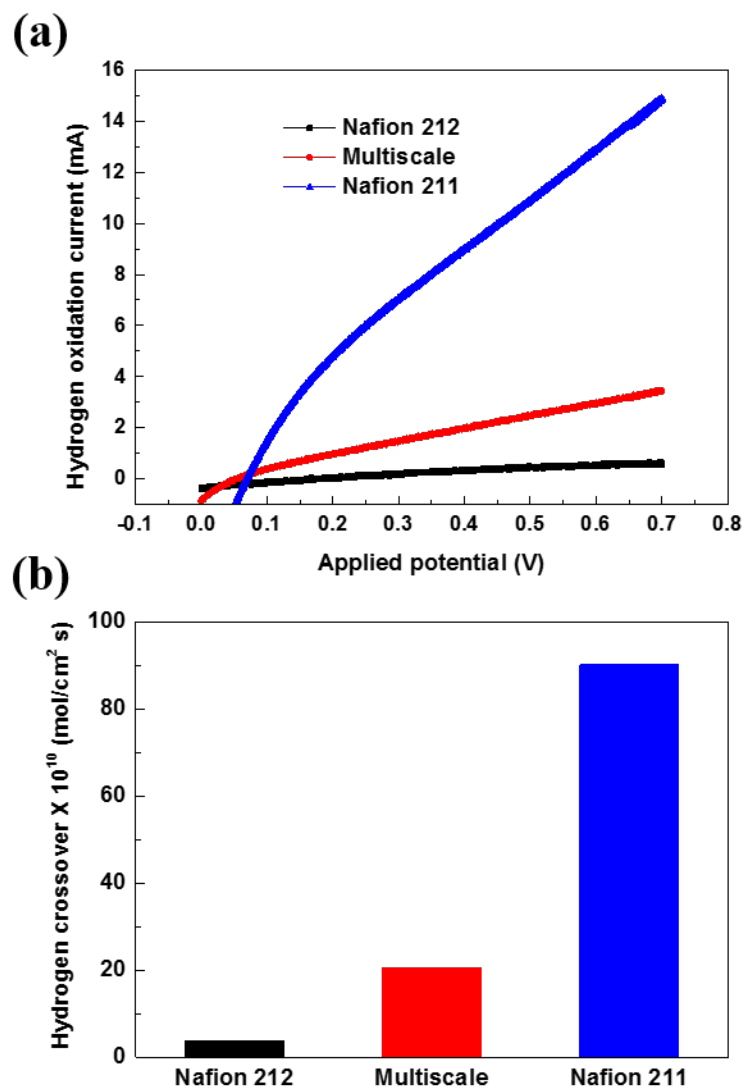


Figure 3-44. (a) Cyclic voltammogram (CV) and difference in ECSAs of MEAs after ADT.



**Figure 3-45.** Comparison of ECSAs of conventional MEA and the MEA with a multiscale Nafion membrane before and after ADT.



**Figure 3-46.** (a) Measurement of permeated hydrogen oxidation current via linear sweep voltammetry in the range from 0 to 0.7 V. vs. RHE and (b) the moles of permeated hydrogen gas at 0.5 V. vs. RHE calculated by Nernst equation.

	$R_{anode}$	$CPE_{anode-T}$	$R_{membrane}$	$R_{cathode}$	$CPE_{cathode-T}$
MEA w/ multiscale membrane	0.00250	0.0520	0.0131 (79.4 %)	0.0354 (80.5 %)	0.0660 (129.4 %)
Conventional MEA	0.00250	0.0510	0.0165 (100 %)	0.0440 (100 %)	0.0510 (100 %)

**Table 3-5.** EIS fitted data of MEAs.



Samples	Pt loading (mg cm <sup>-2</sup> )	Average Pt particle size (nm)	Geometric Surface Area (m <sup>2</sup> g <sup>-1</sup> )	Electroche mical Active Surface Area (m <sup>2</sup> g <sup>-1</sup> )	Pt utilization (%)	Maximum power density (W cm <sup>-2</sup> )	Current density @ 0.6 V (A cm <sup>-2</sup> )	Power density @ 0.6 V (W cm <sup>-2</sup> )	Current density @ 0.8 V (A cm <sup>-2</sup> )	Power density @ 0.8 V (W cm <sup>-2</sup> )
Conventional MEA	0.12	3.00 <sup>a</sup>	93.46 <sup>a</sup>	58.11	62.18	0.4786 <sup>b</sup> (1.000)	0.4906 <sup>b</sup> (1.1104)	0.2954 <sup>b</sup> (0.6662)	0.0202 <sup>b</sup> (0.09)	0.0162 <sup>b</sup> (0.072)
						0.8408 <sup>c</sup> (1.845)	1.3272 <sup>c</sup> (2.634)	0.799 <sup>c</sup> (1.5804)	0.2186 <sup>c</sup> (0.528)	0.1748 <sup>c</sup> (0.4224)
MEA w/ multiscale membrane				69.12	73.96	0.6356 <sup>b</sup> (1.423)	0.7810 <sup>b</sup> (1.842)	0.4702 <sup>b</sup> (1.1052)	0.0508 <sup>b</sup> (0.1906)	0.0408 <sup>b</sup> (0.1524)
						0.9000 <sup>c</sup> (2.026)	1.4672 <sup>c</sup> (2.894)	0.8818 <sup>c</sup> (1.7364)	0.3086 <sup>c</sup> (0.618)	0.2468 <sup>c</sup> (0.4944)
<sup>a</sup> Reference # 44 <sup>b</sup> Cell operation under ambient pressure with H <sub>2</sub> /air (H <sub>2</sub> /O <sub>2</sub> ). <sup>c</sup> Cell operation under pressure of 150 kPa with H <sub>2</sub> /air (H <sub>2</sub> /O <sub>2</sub> ).										

**Table 3-6.** Physical and electrochemical properties of MEAs.

## Chapter 4. Conclusions

---

This study proposed the novel methodologies for the enhancement of PEMFC performance via atomic scale and macroscale approaches as follows. First, in case of atomic scale approaches focusing on electrocatalyst itself, we proposed novel synthetic method of Pt bimetallic alloy nanoparticles (NPs) via Al pitting corrosion method and fabrication of highly active palladium-iron (PdFe) alloy NPs via modified two-step chemical synthesis. By utilizing this novel synthesizing method, we fabricated carbon supported Pt and Pt-M (Au,Pd) NPs very easily without any complex conditions and samples were analyzed via physical, chemical and electrochemical analysis. Additionally, post heat treatment with various conditions were conducted to elucidate the relationship between ORR activity and atomic structure of electrocatalyst. The prepared Pt bimetallic alloy NPs exhibited higher or comparable ORR activity compared to conventional Pt catalyst and due to post heat treatment, the surface structure and alloying degree of samples were changed for desirable ORR activity. Next, PdFe alloy NPs were synthesized via modified two-step chemical synthesis method, which combines polyol reduction method and conventional sodium borohydride method. In addition, the effect of post heat treatment on ORR activity was analyzed by using physical and electrochemical measurements. By the heat treatment, PdFe NPs exhibited intermetallic structures

with Pd rich surface shell and ordered PdFe core. Due to this structural modifications, heat treated PdFe NPs exhibited the downshift of d-band center of Pd from higher alloying degree and, as a result, much higher (2.5 folds) ORR activity compared to as prepared PdFe NPs and conventional Pt catalyst.

As a macroscale approach for modifications of catalyst layer and polymer electrolyte structures, multiscale approach was applied and optimized for enhancing performance of PEMFC. By using multiplex lithography, complex and multiscale architectures was embedded into polymer electrolyte membrane of PEMFC via thermal imprinting process. From the mechanical measurements, the prepared multiscale Nafion membrane exhibited enhance physical propertied due to its multiscale structure. The membrane electrode assembly (MEA) with multiscale patterned Nafion membrane exhibited higher PEMFC performance (by 1.4 folds) due to increased electrochemically active surface area (ECSA) and decrease of proton pathway in thinned polymer electrolyte membrane. The effects on enhanced PEMFC performance were proved by using physical and electrochemical measurements such as scanning electron microscopy (SEM), cyclic voltammogram (CV), electrochemical impedance spectroscopy (EIS) and etc. In addition, for realistic applications of PEMFC such as automotive, we conducted accelerated durability test (ADT) to mimic actual operating condition of PEMFC by potential cycling according to DOE protocols. After ADT, MEA with multiscale membrane still exhibited higher performance than conventional one, which means multiscale

approach for PEMFC can be one of the best ways to increase PEMFC performance and utilization of Pt.

In conclusion, these structural and compositional modifications of Pt group electrocatalysts and its electrode system in PEMFC cathode via atomic scale (Pt and Pd alloy) and macroscale approaches (Structural change in Pt catalyst layer) will contribute to give highly enhanced catalytic activity of electrocatalyst itself and higher performance of PEMFC, which are helpful for commercialization of PEMFC. In addition, the strategies before mentioned can be helpful for designing new materials and systems for another energy conversion devices such as secondary batteries or solar cells.

## References

1. R. P. O'Hayre, S.-W. Cha, W. Colella, F. B. Prinz, *Fuel cell fundamentals*. (John Wiley & Sons New York, 2006).
2. F. Barbir, *PEM fuel cells: theory and practice*. (Academic Press, 2012).
3. W. Grove, On a gaseous voltaic battery. *Journal of the Franklin Institute* **35**, 277-280 (1843).
4. J. Andújar, F. Segura, Fuel cells: History and updating. A walk along two centuries. *Renewable and sustainable energy reviews* **13**, 2309-2322 (2009).
5. U. Paulus *et al.*, Oxygen reduction on carbon-supported Pt-Ni and Pt-Co alloy catalysts. *The Journal of Physical Chemistry B* **106**, 4181-4191 (2002).
6. I. E. Stephens, A. S. Bondarenko, U. Grønbjerg, J. Rossmeisl, I. Chorkendorff, Understanding the electrocatalysis of oxygen reduction on platinum and its alloys. *Energy & Environmental Science* **5**, 6744-6762 (2012).
7. M. T. Koper, S. Lai, E. Herrero, Fuel cell catalysis. *A surface science approach*, 159-207 (2009).
8. T. Toda, H. Igarashi, H. Uchida, M. Watanabe, Enhancement of the electroreduction of oxygen on Pt alloys with Fe, Ni, and Co. *Journal of The Electrochemical Society* **146**, 3750-3756 (1999).
9. C. M. Sánchez-Sánchez, A. J. Bard, Hydrogen peroxide production in the oxygen reduction reaction at different electrocatalysts as quantified by scanning electrochemical microscopy. *Analytical chemistry* **81**, 8094-8100 (2009).
10. O. Antoine, Y. Bultel, R. Durand, Oxygen reduction reaction kinetics and mechanism on platinum nanoparticles inside Nafion®. *Journal of Electroanalytical Chemistry* **499**, 85-94 (2001).
11. N. Markovic, T. Schmidt, V. Stamenkovic, P. Ross, Oxygen reduction reaction on Pt and Pt bimetallic surfaces: a selective review. *FUEL CELLS-WEINHEIM-* **1**, 105-116 (2001).
12. K. Mayrhofer *et al.*, The impact of geometric and surface electronic properties of Pt-catalysts on the particle size effect in electrocatalysis. *The Journal of Physical Chemistry B* **109**, 14433-14440 (2005).
13. E. Antolini, Formation of carbon-supported PtM alloys for low temperature fuel cells: a

- review. *Materials chemistry and physics* **78**, 563-573 (2003).
14. H. Yang, Platinum-Based Electrocatalysts with Core–Shell Nanostructures. *Angewandte Chemie International Edition* **50**, 2674-2676 (2011).
  15. K. J. Mayrhofer, V. Juhart, K. Hartl, M. Hanzlik, M. Arenz, Adsorbate-Induced Surface Segregation for Core–Shell Nanocatalysts. *Angewandte Chemie International Edition* **48**, 3529-3531 (2009).
  16. M. P. Hyman, J. W. Medlin, Effects of electronic structure modifications on the adsorption of oxygen reduction reaction intermediates on model Pt (111)-alloy surfaces. *The Journal of Physical Chemistry C* **111**, 17052-17060 (2007).
  17. J. Wu *et al.*, Truncated octahedral Pt<sub>3</sub>Ni oxygen reduction reaction electrocatalysts. *Journal of the American Chemical Society* **132**, 4984-4985 (2010).
  18. Y. Chen, Z. Liang, F. Yang, Y. Liu, S. Chen, Ni–Pt Core–Shell Nanoparticles as Oxygen Reduction Electrocatalysts: Effect of Pt Shell Coverage. *The Journal of Physical Chemistry C* **115**, 24073-24079 (2011).
  19. C. Wang, H. Daimon, T. Onodera, T. Koda, S. Sun, A General Approach to the Size-and Shape-Controlled Synthesis of Platinum Nanoparticles and Their Catalytic Reduction of Oxygen. *Angewandte Chemie International Edition* **47**, 3588-3591 (2008).
  20. J. R. Salgado, E. Antolini, E. R. Gonzalez, Structure and activity of carbon-supported Pt–Co electrocatalysts for oxygen reduction. *The Journal of Physical Chemistry B* **108**, 17767-17774 (2004).
  21. J. Kim, Y. Lee, S. Sun, Structurally ordered FePt nanoparticles and their enhanced catalysis for oxygen reduction reaction. *Journal of the American Chemical Society* **132**, 4996-4997 (2010).
  22. Y. Liu, C. M. Hangarter, U. Bertocci, T. P. Moffat, Oxygen Reduction Reaction on Electrodeposited Pt<sub>100–x</sub> Ni<sub>x</sub>: Influence of Alloy Composition and Dealloying. *The Journal of Physical Chemistry C* **116**, 7848-7862 (2012).
  23. T.-Y. Jeon, S. J. Yoo, Y.-H. Cho, S. H. Kang, Y.-E. Sung, Effect of de-alloying of Pt–Ni bimetallic nanoparticles on the oxygen reduction reaction. *Electrochemistry Communications* **12**, 1796-1799 (2010).
  24. C. Wang *et al.*, Design and synthesis of bimetallic electrocatalyst with multilayered Pt-skin surfaces. *Journal of the American Chemical Society* **133**, 14396-14403 (2011).

25. S. Chen *et al.*, Origin of oxygen reduction reaction activity on “Pt<sub>3</sub>Co” nanoparticles: atomically resolved chemical compositions and structures. *The Journal of Physical Chemistry C* **113**, 1109-1125 (2008).
26. D. F. van der Vliet *et al.*, Unique Electrochemical Adsorption Properties of Pt-Skin Surfaces. *Angewandte Chemie* **124**, 3193-3196 (2012).
27. Y. Liang *et al.*, Co<sub>3</sub>O<sub>4</sub> nanocrystals on graphene as a synergistic catalyst for oxygen reduction reaction. *Nature materials* **10**, 780-786 (2011).
28. B. Wang, Recent development of non-platinum catalysts for oxygen reduction reaction. *Journal of Power Sources* **152**, 1-15 (2005).
29. Z. Chen, D. Higgins, A. Yu, L. Zhang, J. Zhang, A review on non-precious metal electrocatalysts for PEM fuel cells. *Energy & Environmental Science* **4**, 3167-3192 (2011).
30. A. Morozan, B. Jousselme, S. Palacin, Low-platinum and platinum-free catalysts for the oxygen reduction reaction at fuel cell cathodes. *Energy & Environmental Science* **4**, 1238-1254 (2011).
31. Z. Chen, D. Higgins, H. Tao, R. S. Hsu, Z. Chen, Highly active nitrogen-doped carbon nanotubes for oxygen reduction reaction in fuel cell applications. *The Journal of Physical Chemistry C* **113**, 21008-21013 (2009).
32. Y. Wang, S. Song, V. Maragou, P. K. Shen, P. Tsiakaras, High surface area tungsten carbide microspheres as effective Pt catalyst support for oxygen reduction reaction. *Applied Catalysis B: Environmental* **89**, 223-228 (2009).
33. S. D. Poynton, J. P. Kizewski, R. C. Slade, J. R. Varcoe, Novel electrolyte membranes and non-Pt catalysts for low temperature fuel cells. *Solid State Ionics* **181**, 219-222 (2010).
34. R. Othman, A. L. Dicks, Z. Zhu, Non precious metal catalysts for the PEM fuel cell cathode. *international journal of hydrogen energy* **37**, 357-372 (2012).
35. K. B. Liew *et al.*, Non-Pt catalyst as oxygen reduction reaction in microbial fuel cells: A review. *international journal of hydrogen energy* **39**, 4870-4883 (2014).
36. D. H. Lee, W. J. Lee, W. J. Lee, S. O. Kim, Y.-H. Kim, Theory, synthesis, and oxygen reduction catalysis of Fe-porphyrin-like carbon nanotube. *Physical review letters* **106**, 175502 (2011).
37. T. H. Yu, Y. Sha, B. V. Merinov, W. A. Goddard III, Improved non-Pt alloys for the oxygen reduction reaction at fuel cell cathodes predicted from quantum mechanics. *The Journal of*

- Physical Chemistry C* **114**, 11527-11533 (2010).
38. K. Lee, L. Zhang, J. Zhang, Ternary non-noble metal chalcogenide (W–Co–Se) as electrocatalyst for oxygen reduction reaction. *Electrochemistry communications* **9**, 1704-1708 (2007).
  39. A. Brouzgou, S. Song, P. Tsiakaras, Low and non-platinum electrocatalysts for PEMFCs: current status, challenges and prospects. *Applied Catalysis B: Environmental* **127**, 371-388 (2012).
  40. G. Wu, Z. Chen, K. Artyushkova, F. H. Garzon, P. Zelenay, Polyaniline-derived non-precious catalyst for the polymer electrolyte fuel cell cathode. *ECS Transactions* **16**, 159-170 (2008).
  41. A. D. Taylor, B. D. Lucas, L. J. Guo, L. T. Thompson, Nanoimprinted electrodes for micro-fuel cell applications. *Journal of Power Sources* **171**, 218-223 (2007).
  42. K. Shah, W. Shin, R. Besser, Novel microfabrication approaches for directly patterning PEM fuel cell membranes. *Journal of power sources* **123**, 172-181 (2003).
  43. M. H. Yildirim, J. te Braake, H. C. Aran, D. Stamatialis, M. Wessling, Micro-patterned Nafion membranes for direct methanol fuel cell applications. *Journal of Membrane Science* **349**, 231-236 (2010).
  44. W. S. Chi, Y. Jeon, S. J. Park, J. H. Kim, Y. G. Shul, Fabrication of Surface-Patterned Membranes by Means of a ZnO Nanorod Templating Method for Polymer Electrolyte Membrane Fuel-Cell Applications. *ChemPlusChem* **79**, 1109-1115 (2014).
  45. Y. Qiu, H. Zhang, H. Zhong, F. Zhang, A novel cathode structure with double catalyst layers and low Pt loading for proton exchange membrane fuel cells. *International Journal of Hydrogen Energy* **38**, 5836-5844 (2013).
  46. Y.-H. Cho *et al.*, High performance direct methanol fuel cells with micro/nano-patterned polymer electrolyte membrane. *Journal of Membrane Science* **467**, 36-40 (2014).
  47. Y.-H. Cho *et al.*, Performance enhancement of membrane electrode assemblies with plasma etched polymer electrolyte membrane in PEM fuel cell. *international journal of hydrogen energy* **35**, 10452-10456 (2010).
  48. Y.-H. Cho *et al.*, Improved mass transfer using a pore former in cathode catalyst layer in the direct methanol fuel cell. *international journal of hydrogen energy* **37**, 11969-11974 (2012).



49. Z. Q. Tian *et al.*, A Highly Order-Structured Membrane Electrode Assembly with Vertically Aligned Carbon Nanotubes for Ultra-Low Pt Loading PEM Fuel Cells. *Advanced Energy Materials* **1**, 1205-1214 (2011).
50. W. Li, T. Cochell, A. Manthiram, Activation of Aluminum as an Effective Reducing Agent by Pitting Corrosion for Wet-chemical Synthesis. *Scientific reports* **3**, (2013).
51. J. L. Fernández, V. Raghuv eer, A. Manthiram, A. J. Bard, Pd-Ti and Pd-Co-Au electrocatalysts as a replacement for platinum for oxygen reduction in proton exchange membrane fuel cells. *Journal of the American Chemical Society* **127**, 13100-13101 (2005).
52. M.-H. Shao, K. Sasaki, R. R. Adzic, Pd-Fe nanoparticles as electrocatalysts for oxygen reduction. *Journal of the American Chemical Society* **128**, 3526-3527 (2006).
53. Y. Suo, L. Zhuang, J. Lu, First-Principles Considerations in the Design of Pd-Alloy Catalysts for Oxygen Reduction. *Angewandte Chemie International Edition* **46**, 2862-2864 (2007).
54. D. Wang *et al.*, Facile synthesis of carbon-supported Pd-Co core-shell nanoparticles as oxygen reduction electrocatalysts and their enhanced activity and stability with monolayer Pt decoration. *Chemistry of Materials* **24**, 2274-2281 (2012).
55. M. Shao, P. Liu, J. Zhang, R. Adzic, Origin of enhanced activity in palladium alloy electrocatalysts for oxygen reduction reaction. *The Journal of Physical Chemistry B* **111**, 6772-6775 (2007).
56. Z. Zhang, K. L. More, K. Sun, Z. Wu, W. Li, Preparation and characterization of PdFe nanoleaves as electrocatalysts for oxygen reduction reaction. *Chemistry of Materials* **23**, 1570-1577 (2011).
57. Y. Liu, C. Xu, Nanoporous PdTi Alloys as Non-Platinum Oxygen-Reduction Reaction Electrocatalysts with Enhanced Activity and Durability. *ChemSusChem* **6**, 78-84 (2013).
58. B. Han, C. Xu, Nanoporous PdFe alloy as highly active and durable electrocatalyst for oxygen reduction reaction. *International Journal of Hydrogen Energy* **39**, 18247-18255 (2014).
59. K. Liu, L. Jiang, Multifunctional integration: from biological to bio-inspired materials. *Acs Nano* **5**, 6786-6790 (2011).
60. J. J. Lerou, K. M. Ng, Chemical reaction engineering: A multiscale approach to a multiobjective task. *Chemical Engineering Science* **51**, 1595-1614 (1996).

61. M. Nosonovsky, B. Bhushan, Biomimetic superhydrophobic surfaces: multiscale approach. *Nano letters* **7**, 2633-2637 (2007).
62. M. Nosonovsky, B. Bhushan, Multiscale effects and capillary interactions in functional biomimetic surfaces for energy conversion and green engineering. *Philosophical Transactions of the Royal Society of London A: Mathematical, Physical and Engineering Sciences* **367**, 1511-1539 (2009).
63. H. E. Jeong, R. Kwak, A. Khademhosseini, K. Y. Suh, UV-assisted capillary force lithography for engineering biomimetic multiscale hierarchical structures: from lotus leaf to gecko foot hairs. *Nanoscale* **1**, 331-338 (2009).
64. X.-Z. Yuan, H. Li, S. Zhang, J. Martin, H. Wang, A review of polymer electrolyte membrane fuel cell durability test protocols. *Journal of Power Sources* **196**, 9107-9116 (2011).
65. A. J. Bard, L. R. Faulkner, *Electrochemical methods: fundamentals and applications*. (Wiley New York, 1980), vol. 2.
66. V. Mazumder, S. Sun, Oleylamine-mediated synthesis of Pd nanoparticles for catalytic formic acid oxidation. *Journal of the American Chemical Society* **131**, 4588-4589 (2009).
67. Z. Niu, Q. Peng, M. Gong, H. Rong, Y. Li, Oleylamine-Mediated Shape Evolution of Palladium Nanocrystals. *Angewandte Chemie* **123**, 6439-6443 (2011).
68. á. Ravel, M. Newville, ATHENA, ARTEMIS, HEPHAESTUS: data analysis for X-ray absorption spectroscopy using IFEFFIT. *Journal of synchrotron radiation* **12**, 537-541 (2005).
69. T. Ko *et al.*, Cross-Linked Sulfonated Poly (arylene ether sulfone) Membranes Formed by in Situ Casting and Click Reaction for Applications in Fuel Cells. *Macromolecules* **48**, 1104-1114 (2015).
70. J. Wu *et al.*, Diagnostic tools in PEM fuel cell research: Part I Electrochemical techniques. *International journal of hydrogen energy* **33**, 1735-1746 (2008).
71. X. Fu, F. Bei, X. Wang, S. O'Brien, J. R. Lombardi, Excitation profile of surface-enhanced Raman scattering in graphene–metal nanoparticle based derivatives. *Nanoscale* **2**, 1461-1466 (2010).
72. C. Xu, R. Wang, M. Chen, Y. Zhang, Y. Ding, Dealloying to nanoporous Au/Pt alloys and their structure sensitive electrocatalytic properties. *Physical Chemistry Chemical Physics*

- 12**, 239-246 (2010).
73. A. R. Denton, N. W. Ashcroft, Vegard's law. *Physical Review A* **43**, 3161 (1991).
  74. N. R. Jana, L. Gearheart, C. J. Murphy, Evidence for seed-mediated nucleation in the chemical reduction of gold salts to gold nanoparticles. *Chemistry of Materials* **13**, 2313-2322 (2001).
  75. B. L. Cushing, V. L. Kolesnichenko, C. J. O'Connor, Recent advances in the liquid-phase syntheses of inorganic nanoparticles. *Chem Rev* **104**, 3893-3946 (2004).
  76. A. N. Goldstein. (Google Patents, 2003).
  77. K.-S. Lee *et al.*, Reversible Surface Segregation of Pt in a Pt<sub>3</sub>Au/C Catalyst and Its Effect on the Oxygen Reduction Reaction. *The Journal of Physical Chemistry C* **117**, 9164-9170 (2013).
  78. I. Y. Cha, M. Ahn, S. J. Yoo, Y.-E. Sung, Facile synthesis of carbon supported metal nanoparticles via sputtering onto a liquid substrate and their electrochemical application. *RSC Advances* **4**, 38575-38580 (2014).
  79. M. Wakisaka *et al.*, Electronic structures of Pt-Co and Pt-Ru alloys for CO-tolerant anode catalysts in polymer electrolyte fuel cells studied by EC-XPS. *The Journal of Physical Chemistry B* **110**, 23489-23496 (2006).
  80. P. Urchaga, S. v. Baranton, C. Coutanceau, G. Jerkiewicz, Electro-oxidation of COchem on Pt nanosurfaces: solution of the peak multiplicity puzzle. *Langmuir* **28**, 3658-3663 (2011).
  81. J. Wang, N. Markovic, R. Adzic, Kinetic analysis of oxygen reduction on Pt (111) in acid solutions: Intrinsic kinetic parameters and anion adsorption effects. *The Journal of Physical Chemistry B* **108**, 4127-4133 (2004).
  82. X. Xia, T. Iwasita, F. Ge, W. Vielstich, Structural effects and reactivity in methanol oxidation on polycrystalline and single crystal platinum. *Electrochimica Acta* **41**, 711-718 (1996).
  83. J. Clavilier, C. Lamy, J. Leger, Electrocatalytic oxidation of methanol on single crystal platinum electrodes. Comparison with polycrystalline platinum. *Journal of Electroanalytical Chemistry and Interfacial Electrochemistry* **125**, 249-254 (1981).
  84. C. K. Rhee *et al.*, Size effect of Pt nanoparticle on catalytic activity in oxidation of methanol and formic acid: comparison to Pt (111), Pt (100), and polycrystalline Pt electrodes. *Langmuir* **25**, 7140-7147 (2009).

85. T.-Y. Jeon *et al.*, Electrocatalytic Effects of Carbon Dissolution in Pd Nanoparticles. *Langmuir* **28**, 3664-3670 (2012).
86. K.-S. Lee, S. J. Yoo, J. H. Jang, Y.-E. Sung, Effect of the amount of reducing agent on surface structures, electrochemical activity and stability of PtRu catalysts. *Electrochimica Acta* **56**, 8688-8694 (2011).
87. Z. Liu, X. Y. Ling, X. Su, J. Y. Lee, Carbon-supported Pt and PtRu nanoparticles as catalysts for a direct methanol fuel cell. *The Journal of Physical Chemistry B* **108**, 8234-8240 (2004).
88. H.-Y. Park *et al.*, Enhancement of oxygen reduction reaction on PtAu nanoparticles via CO induced surface Pt enrichment. *Applied Catalysis B: Environmental* **129**, 375-381 (2013).
89. K. Mayrhofer *et al.*, CO surface electrochemistry on Pt-nanoparticles: A selective review. *Electrochimica Acta* **50**, 5144-5154 (2005).
90. P. Hernández-Fernández *et al.*, Influence of the preparation route of bimetallic Pt-Au nanoparticle electrocatalysts for the oxygen reduction reaction. *The Journal of Physical Chemistry C* **111**, 2913-2923 (2007).
91. S.-Y. Lee *et al.*, Surface-Rearranged Pd<sub>3</sub>Au/C Nanocatalysts by Using CO-Induced Segregation for Formic Acid Oxidation Reactions. *ACS Catalysis* **4**, 2402-2408 (2014).
92. K.-S. Lee *et al.*, Phosphate adsorption and its effect on oxygen reduction reaction for Pt x Co y alloy and Au core–Pt shell electrocatalysts. *Electrochimica Acta* **56**, 8802-8810 (2011).
93. C. Decker, T. Nguyen Thi Viet, D. Decker, E. Weber-Koehl, UV-radiation curing of acrylate/epoxide systems. *Polymer* **42**, 5531-5541 (2001).
94. J. B. Lambert, H. F. Shurvell, D. A. Lightner, R. G. Cooks, *Introduction to organic spectroscopy*. (Macmillan New York, 1987).
95. A. del Campo, E. Arzt, Fabrication approaches for generating complex micro- and nanopatterns on polymeric surfaces. *Chem Rev* **108**, 911-945 (2008).
96. Y. Zhang, C. T. Lin, S. Yang, Fabrication of Hierarchical Pillar Arrays from Thermoplastic and Photosensitive SU-8. *Small* **6**, 768-775 (2010).
97. F. X. Zhang, J. Chan, H. Y. Low, Biomimetic, hierarchical structures on polymer surfaces by sequential imprinting. *Appl Surf Sci* **254**, 2975-2979 (2008).
98. M. S. Onses *et al.*, Hierarchical patterns of three-dimensional block-copolymer films formed by electrohydrodynamic jet printing and self-assembly. *Nat Nanotechnol* **8**, 667-675 (2013).

99. C. Chen *et al.*, Highly crystalline multimetallic nanoframes with three-dimensional electrocatalytic surfaces. *Science* **343**, 1339-1343 (2014).
100. G. Wu *et al.*, A carbon-nanotube-supported graphene-rich non-precious metal oxygen reduction catalyst with enhanced performance durability. *Chemical Communications* **49**, 3291-3293 (2013).
101. R. Bashyam, P. Zelenay, A class of non-precious metal composite catalysts for fuel cells. *Nature* **443**, 63-66 (2006).
102. E. Proietti *et al.*, Iron-based cathode catalyst with enhanced power density in polymer electrolyte membrane fuel cells. *Nature communications* **2**, 416 (2011).
103. Y.-C. Hsieh *et al.*, Ordered bilayer ruthenium–platinum core-shell nanoparticles as carbon monoxide-tolerant fuel cell catalysts. *Nature communications* **4**, (2013).
104. J. W. Bae, Y.-H. Cho, Y.-E. Sung, K. Shin, J. Y. Jho, Performance enhancement of polymer electrolyte membrane fuel cell by employing line-patterned Nafion membrane. *Journal of Industrial and Engineering Chemistry* **18**, 876-879 (2012).
105. J. K. Koh, Y. Jeon, Y. I. Cho, J. H. Kim, Y.-G. Shul, A facile preparation method of surface patterned polymer electrolyte membranes for fuel cell applications. *Journal of Materials Chemistry A* **2**, 8652-8659 (2014).
106. O.-H. Kim *et al.*, Ordered macroporous platinum electrode and enhanced mass transfer in fuel cells using inverse opal structure. *Nature communications* **4**, (2013).
107. R. Borup *et al.*, Scientific aspects of polymer electrolyte fuel cell durability and degradation. *Chem Rev* **107**, 3904-3951 (2007).
108. S. Slade, S. Campbell, T. Ralph, F. Walsh, Ionic conductivity of an extruded Nafion 1100 EW series of membranes. *Journal of The Electrochemical Society* **149**, A1556-A1564 (2002).
109. H. Cho *et al.*, Replication of flexible polymer membranes with geometry-controllable nano-apertures via a hierarchical mould-based dewetting. *Nature communications* **5**, (2014).
110. C. Houchins *et al.*, US DOE progress towards developing low-cost, high performance, durable polymer electrolyte membranes for fuel cell applications. *Membranes* **2**, 855-878 (2012).
111. S. Gouws, Voltammetric Characterization Methods for the PEM Evaluation of Catalysts. (2012).

## 국문초록

### 고분자 전해질 연료전지의 산소환원반응을 위한 백금족 전기촉매 및 멀티스케일 전극 구조

고분자 전해질 연료전지는 수소와 산소를 이용해 전기를 생산해내는 장치로서, 높은 에너지 변환 효율을 가지는 동시에 환경 오염을 일으키지 않는 장점을 가지고 있다. 이러한 장점으로 인해 차세대 자동차 동력기관, 고정 전력원 등 기타 다양한 분야에서의 적용이 가능하다고 알려져 있다. 현재 고분자 전해질 연료전지의 전극물질로 사용되는 탄소에 담지된 나노 크기의 백금 촉매는 환원극에서 일어나는 산소 환원 반응에 매우 적합한 물질이지만, 충분한 촉매 활성을 나타내지 못하고 있으며 물질의 높은 가격 또한 상용화에 큰 문제가 되고 있다. 이러한 문제점을 해결하기 위해 촉매적 관점에서의 연구로 최근 백금 합금 촉매 및 코어-셸 촉매, 비백금 계열 합금 촉매 또는 산화물 촉매, 전이금속-질소 화합물 촉매, 전도성 고분자 물질 등이 연구되고 있다. 또한 연료전지 구조 및 시스템 측면에서, 전지 활성 증대를 위한 기공형성제의 사용, 정렬 구조의 백금 촉매층 구현, 고분자 전해질 패터닝을 통한 전극 구조 개선 등의 연구가 진행되고 있다. 이러한 촉매적 관점 및 전극 구조적 관점의 연구들은 연료전지의 성능

증가 및 백금족 촉매의 이용률 향상을 목표로 진행되고 있다.

본 연구에서는 원자적 수준 및 거시적 수준에서의 백금족 (백금, 팔라듐) 이원계 합금 촉매와 그 전극 시스템의 구조 개선 및 조성 변화에 따른 전기화학적 활성과 연료전지 성능에 관한 연구를 진행하였다. 첫 번째로, 원자적 수준 관점에서의 연구로, 백금 촉매의 활성을 높일 수 있는 가장 일반적인 방식인 백금 이원계 합금 촉매의 합성에 대한 연구를 소개하였다. 본 연구는 이전의 백금 이원계 합금 촉매의 합성 연구와 다르게 기존에 사용되던 금속수소화물 환원제 대신 알루미늄 금속 호일을 환원제로 이용하여 합성을 진행하였다. 환원제로 사용된 알루미늄 금속 호일은 고체상이기 때문에 저장 및 이동이 쉬우며 금속수소화물 환원제와는 다르게 공기 중에서 자유롭게 보관이 가능하다. 또한 이전의 백금 이원계 합금 촉매를 합성할 시 필요했던 고온 조건, 유독한 용매 및 안정제의 사용을 줄이면서 현저히 낮은 제조비용으로 더욱 쉽게 금속 합금 나노 입자의 합성을 진행할 수 있었다. 추가적으로, 산소 환원 반응 활성과 백금 이원계 합금 입자의 표면 구조와의 관계를 파악하기 위해 여러 가지 조건의 열처리를 진행하였다.

두 번째 원자적 수준에서의 연구로, 백금의 사용량 저감을 위한 고활성 팔라듐 이원계 합금 입자의 합성에 관련한 연구를 진행하였다. 팔라듐과 다른 전이금속 (철, 코발트, 니켈, 티타늄, 구리 등) 의 이원계 합금 촉매는 백금 촉매와 비교했을 때 더 낮은 가격 및 비교적

많은 매장량의 장점을 가지며, 비슷한 수준의 산소 환원 반응 활성을 보이는 것으로 알려져 있다. 본 연구에서는 팔라듐-철 이원계 합금 촉매를 폴리올 합성 방식과 소듐수소화물을 이용한 합성방식을 결합하여 합성하고, 고온의 열처리를 통해 구조 변화 및 성능 증대를 달성하였다. 이렇게 합성된 팔라듐-철 이원계 합금 촉매를 고온의 수소조건에서 열처리 한 후 여러 분석을 진행하였는데, 열처리 후 결과적으로 팔라듐 셀 - 정렬된 팔라듐-철 코어의 금속간 화합물 구조가 만들어졌음이 확인되었다. 이렇게 열처리로부터 얻어진 팔라듐-철 금속간 화합물 구조로 인해 팔라듐의 d-band center 위치가 기존보다 내려가게 되고, 결과적으로 상용 백금 촉매 대비 높은 산소환원반응 활성을 나타내었다.

세 번째로는, 거시적 수준에서의 연구로, 멀티스케일 접근법을 통한 단위 연료전지내의 촉매층의 구조를 변화시켜 촉매의 이용률 향상 및 단위전지 성능의 증가에 관한 연구를 진행하였다. 본 연구에서는 멀티플렉스 리소그래피 공정을 통해 제작된 멀티스케일 고분자 구조물을 나노 임프린트 리소그래피 공정을 통해 나피온 이온교환막에 계층구조물을 새긴 후, 이를 단위전지 구조에 적용하였다. 계층구조물을 가지는 나피온 이온교환막의 경우, 기존의 상용 나피온 211, 212 이온교환막과 비교하여 향상된 물리적 및 전기화학적 특성을 나타내었다. 특히 얇아진 두께로 인해 감소한 전기화학적 저항 값 및 이온교환막의 표면의 패턴 구조물로 인한 촉매층 구조변화에 따른



삼상계면 증가 등의 효과가 나타났으며, 이로 인해 단위전지 성능이 향상되는 결과가 얻어졌다. 또한 연료전지의 실제적인 적용을 위해, 전압순환법을 통한 가속 장기안정성 실험을 진행하였다. 가속 장기안정성 실험 후에도 계층 고분자 막을 포함하는 단위전지의 파손이나 단락 문제가 발견되지 않았으며, 기존 전지 대비 높은 성능을 유지하는 것으로 나타났다.

결론적으로, 원자적 수준 및 거시적 수준에서의 백금족 촉매(백금 이원계 합금 촉매, 팔라듐 이원계 합금 촉매)와 연료전지 전극 구조 개선 (멀티스케일 구조 적용한 촉매층 구조 개선) 및 조성 변화의 두 가지 접근법을 통해 고분자 전해질 촉매 및 시스템의 개선을 유도하여 촉매 활성 증대 및 전지 성능의 증가를 이루어내었다. 또한 이러한 연구결과를 토대로 향후 연료전지 촉매 및 전극구조의 설계뿐만 아니라 배터리나 태양전지 등 다른 전기화학적 에너지 변환 장치에 사용 가능한 새로운 재료 및 전지 구조의 제작에 활용 가능한 실험적 방법 및 이론을 확보할 수 있었다고 판단된다.

주요어: 고분자 전해질 연료전지, 산소 환원 반응, 백금족 이원계 합금 촉매, 백금 촉매층, 입자 결정 구조, 멀티스케일 구조.

학번: 2011-30274